Università Ca'Foscari Venezia

Centro Euro-Mediterraneo sui Cambiamenti Climatici

CORSO DI DOTTORATO DI RICERCA IN

SCIENZA E GESTIONE DEI CAMBIAMENTI CLIMATICI

Ciclo XXIX

Tesi di Ricerca

Defining the time and spatial scale of climate response to CO_2 changes

Settore scientifico disciplinare di afferenza: GEO/12

Coordinatore del Dottorato:

Prof. Carlo Barbante

Supervisore:

Dr. Antonio Navarra

Dottoranda:

Marianna Benassi

Matricola 956089

Defining the time and spatial scale of climate response to CO_2 changes

Marianna Benassi

in ricordo di Paolo Gentilini

Acknowledgements

Several people have been important in the realization of this thesis, and I should like, on this occasion, to thank them all.

First of all I wish to thank deeply my supervisor, Dr Antonio Navarra, for the time and the patience he has devoted to my work during these years. Without his foresight and his constant support many of the results I have achieved during my PhD would have not been possible. The researchers and the staff of CMCC have been there every day, ready to help. A special mention to Pier Giuseppe Fogli for the precious advices he gave to me, especially in the coding part of this work.

During the period I have spent at NCAR, I had the invaluable opportunity to work with Dr Joe Tribbia. Joe's teachings have deeply influenced my approach to science and to the study of climate, and his suggestions have been fundamental in my PhD experience.

I would like to acknowledge the staff of University of Venice for the helpful assistance, Prof Stefano Tinti and Prof Emanuele Di Lorenzo for reviewing this work and for their valuable comments and suggestions.

Thanks to my colleagues, María del Mar, Ali, Prakash, Daniele, Giovanni, Irene, Enea, Paola, and all the others with whom I have shared good moments and bad moments during the long days in the PhD student office.

Last, but obviously not least, a very heartfelt thanks to Simone. In these years his incessant support and his smile have given me the determination and the self-confidence essential to tackle every difficulty I have encountered and to accomplish all my goals.

Abstract

The goal of this research is to investigate the response of climate system to both temporal and spatial variations in the atmospheric carbon dioxide concentration.

In the first part, the climatic signal related to an impulsive CO_2 forcing has been detected and investigated, while in the second one the goal has been to study the effects on atmosphere variability of a spatially non-homogenous concentration of carbon dioxide. By forcing the system with a pulse of CO_2, the response function of the atmosphere has been detected with an Empirical Orthogonal Function (EOF) analysis. The robustness of these results has been tested and confirmed with a set of different experiments, which have also allowed to define the typical time scale involved in the fast response of the system to variations in the radiative CO_2 forcing.

Carbon dioxide is generally considered as a well-mixed greenhouse gas. However, as confirmed by satellite measurements, there is some spatial variability in the atmospheric CO_2 concentration. The effects on the state of the atmosphere of a stationary anomaly of CO_2 concentration over different regions have been studied with a set of experiments (ensemble approach), and a statistically significant signal has been detected. To have a more direct evaluation of the dynamical fingerprint in this stationary framework, the dynamical linear response due to the localized CO_2-related forcing has been studied. In order to obtain this linear response, the linearized version of the same dynamical core exploited in the full non linear simulations has been proposed. This new linear model represents the first attempt to to linearize the current version of the Eulerian Dynamical Core of CAM (Community Atmosphere Model), and it is a simple but powerful tool to study the response of the atmosphere to stationary perturbation. The linearized experiments have allowed to assess which forcing region, among the ones analyzed in this work, is particularly effective in terms of both amplitude and spatial extent of the response.

Table of Contents

List of Figures

Introduction

Climate dynamics and variability are driven and influenced by several factors. The system is intrinsically non linear, and at the same time it is forced by external factors, both natural (*e.g.* the solar cycle variation, or the volcainc activity) and human-induced (*e.g.* the emission of radiatevely active components in the atmosphere, or the land cover change). These components contribute in a complex way to the overall evolution of the climate system on a number of temporal and spatial scales, with both direct and feedback effects.

In the last decades, one may register an increasing interest in investigating the effects on climate of the *anthropogenic forcing*, both from a scientific point of view and for the related policy implications. This is the focus of the so-called *detection and attribution* problem: the aim is to recognise and separate the signals related to external forcings from the ones linked to the internal variability of the system. As described in Hegerl and Zwiers (2011), several authors have tried to assess the effects of the anthropogenic forcing by analysing directly the observations. These procedures generally require some *a priori* hypotheses on the characteristics of the processes involved in the response of the system to the forcing - hypotheses which in most cases may be restrictive and likely to lead to an incomplete interpretation of the obtained signal.

For this reason, also in this framework, General Circulation Models (GCMs) play a fundamental role. GCMs solve numerically, on a discrete spatial and temporal domain, the empirical and deterministic equations which describe the state and the evolution of the atmosphere, the ocean, and of all the other components which constitute the Earth System (*e.g.* the land surface, the sea and the land ice, and so on). Under the assumption that the models account for the right mechanisms at work, they may provide a realistic representation of the state and evolution of the climate system. By properly defining the boundary conditions constraining the evolution of the system, GCMs may supply forecast, predictions, and projections of climate in the future, over a wide range of time scales; moreover, they allow to reconstruct the climate in the past, as for example in paleoclimatology experiments. On the other hand, numerical models allow one to perform idealized experiments: by introducing controlled and simplifying hypotheses, it is possible to isolate and study single aspects of the system, which in principle may lead to a better

understanding of the complex processes and mechanisms observed in nature.

In this research we want to study the signature in the atmospheric state related to changes, in both time and space, of the carbon dioxide concentration. Our approach is different from the ones which usually can be found in the literature. Instead of making some *a priori* hypotheses on the shape of the signals linked to the external forcing, our goal is to arrive at defining in a direct way the fingerprint related to the CO_2 forcing. We will focus on both the time and spatial structure of the response.

In the first part, we will deal with the response of the atmosphere to a time pulse change in carbon dioxide concentration. As will be extensively discussed, if we formalize our problem as a dynamical system (*i.e.* the atmosphere) under the effects of an external forcing (*i.e.* the CO_2 concentration), the response to a time pulse defines the *response function* of the system. This response function is an efficient but fully consistent method to characterize the system: it represents the elementary response of that system to the considered forcing. For this reason, in our case, defining the response function will provide some insight on the features of the signal due to carbon dioxide. It is important to stress that the response function approach is usually defined in a linear framework. Given the intrinsic non linearity of the atmosphere, introducing some approximations will be necessary. In order to define the response function of the system, we will perform a set of numerical experiments accounting for a pulse of carbon dioxide concentration. From the outcomes of these simulations we will extrapolate a signal which will be interpreted as directly due to the applied forcing, and thus as the response function of the system. This part of the work is structured as follows: in Chapter One the response function formalism will be presented, together with an overview on how this approach has been previously exploited in climate change studies. The model, the experimental design, and the analytical tools used to define the response function of the system will be described in Chapter Two, and finally in Chapter Three the obtained results will be presented and discussed.

In the second part of this work, we will focus on the spatial response. In particular, we concentrate on the effects of a non-homogeneous and stationary anomaly in carbon dioxide concentration. Although CO_2 is generally considered a well-mixed greenhouse gas, it has been observed that its spatial distribution is far from being homogeneous, mainly because of the non uniform distribution at the surface of sources and sinks, and of the characteristics of the large scale circulation pattern. Even if the amplitude of these spatial anomalies is generally small, in most cases they are persistent in time. To assess the effects of a persistent anomaly of CO_2 on the atmosphere, a set of idealized numerical experiments have been performed: an anomalous and stationary distribution of carbon dioxide has been introduced over selected regions, and the steady state signal due to this forcing has been extracted. In order to further investigate the effects of a localized CO_2 anomaly, we have used a stationary linear model forced by this forcing. The linear response, even though it

gives just a partial picture in comparison to the full non-linear signal, allows a much more direct assessment of the response. For this reason several studies in the literature have attempted to examine the main features of the atmospheric circulation by focusing on the signals obtained in a linearized framework. A new linear model will be proposed, sharing the same numerical scheme of the original non-linear atmospheric model exploited in this research. Through this new tool it will be possible to derive the response of the system to a stationary forcing, and hence to further characterize the signature related to the presence of a persistent anomaly of carbon dioxide concentration.

This part is organized as follows: the non linear experiments accounting for the localized CO_2 anomalies and the obtained results will be discussed in Chapter Four. The new linear model will be presented in Chapter Five, while the results from the linearized experiments will be analysed in Chapter Six. Finally in the last chapter we will provide an overall summary of the results and some concluding remarks.

Chapter 1

Atmospheric Response Function to CO_2 variations

Changes in the atmospheric greenhouse gas content and the related effects on the atmospheric circulation and climate variability are a major concern for the climate change community, both from a scientific and a policy implication point of view. Carbon dioxide is generally considered to be the major contributor to long term climate change, due to its efficacy in acting on the radiative balance of the atmosphere, and its long residence time in the atmosphere.

By radiative balance we mean the equilibrium between the absorbed and the emitted energy through the atmosphere. Carbon dioxide absorbs the long-wave radiation emitted by the Earth's surface and re-emits it in the air column, trapping heat into the atmosphere. Schematically this is the natural mechanism which has allowed to keep the Earth's surface warmer than what it would have been without an atmosphere, and so made it hospitable for life as we know it. But this very same mechanism, when the greenhouse gas concentration in the atmosphere is altered, may produce a mean warming at the Earth surface, driving deep changes in climate dynamics and variability.

Since the seminal works by Manabe and Wetherald (1967, 1975), numerical models have become the preferred tool to study the effects of carbon dioxide on the atmosphere and on climate variability. General circulation models (GCMs) solve on a discrete spatial and temporal domain the equations describing the behaviour of the various components of the Earth system. In addition to forecasts and projections of the future climate, numerical models allow to perform idealized experiments, in which theoretical hypotheses may be tested to better understand the mechanisms behind the complex behaviour observed in nature.

To study the fingerprint of the CO_2 effects usually some realistic or idealized path of carbon dioxide concentration is assumed and hence introduced as boundary condition in a GCM simulation. In this framework we want to deal with this problem from a slightly

different point of view. The idea is to formalize the problem as a dynamical system (the atmosphere) under the action of an external forcing (the altered carbon dioxide concentration). In this way, if a single or a set of variables ($\mathcal{X}$) is chosen to represent the state of the atmosphere, at least to a first approximation it is possible to reduce the dynamics of the forced system to a simple linear relation:

$$\mathcal{L}_{\mathbf{x},t}\ (\mathcal{X}(\mathbf{x},t)) = f(t)$$

where $\mathcal{L}$ represent a generic linear operator, and $f(t)$ is the external forcing. Even if we do not know explicitly which is the shape of the linear operator $\mathcal{L}$, it is always possible to deduce the response to the forcing by defining the *response function* of the system. The response function is a compact formalism to describe the system, but in principle it fully characterizes the system dynamics. Of course, in nature the radiative forcing due to greenhouse gases interacts with the system also through feedbacks and non-linear effects which strongly complicate the detection of this signal. Nevertheless, the response function is an efficient and powerful tool, and it still includes some fundamental features of the atmosphere response to carbon dioxide forcing.

1.1 The Response Function approach

The atmosphere is intrinsically a strongly non-linear system. However, as for any other differentiable non linear system, the response to a small external forcing in a first order approximation may be considered linear. Relying on this assumption, our aim is to investigate the linear response of the atmosphere to the carbon dioxide-related radiative forcing.

Let us consider a dynamical system - in our case the atmosphere - undergoing the action of an external forcing. Under the "small perturbation" hypothesis, *i.e.* if the variations from the reference state due to the forcing are small in comparison with the basic state itself, the following equation is always valid:

$$x(t) = \int_0^t \mathcal{G}(t-t')f(t')d\,t' \tag{1.1}$$

Here $x(t)$ is a vector representing the state of the system, $f(t)$ is the forcing acting on it, and $\mathcal{G}(t)$ is the *Response Function*. In this brief overview the state of the system is represented in terms of global mean quantities, thus both $x(t)$ and $\mathcal{G}(t)$ are only dependent on time.

To better understand equation (1.1), consider the instance of a pulse forcing centered at some time t'. Analytically an impulse is represented by a Dirac δ function $\delta(t)$, so the pulse forcing may be written as:

$$f(t) = \delta(t-t')$$

Equation (1.1) becomes:

$$x(t) = \int_0^t \mathcal{G}(t - t')\delta(t - t')dt' \tag{1.2}$$

and hence, for the well-known properties of the Dirac δ function:

$$x(t) = \mathcal{G}(t) \tag{1.3}$$

The response function is the particular solution of the general forced problem in the case of an impulsive forcing. Thus, if the system undergoes the action of a generic time varying forcing, from equation (1.1), its response at a given time t can be interpreted as the sum of the responses to single pulses preceding t with a convenient delay. For this reason often the response function is called also *Impulsive Response Function* (IRF).

In a fully-linear framework the response function is nothing but the *Green's function* of the system. For the sake of simplicity here the two locutions will be used interchangeably, even if, to be rigorous, by "response function" one should mean the generalization of the Green's function concept for a system which is just approximately linear.

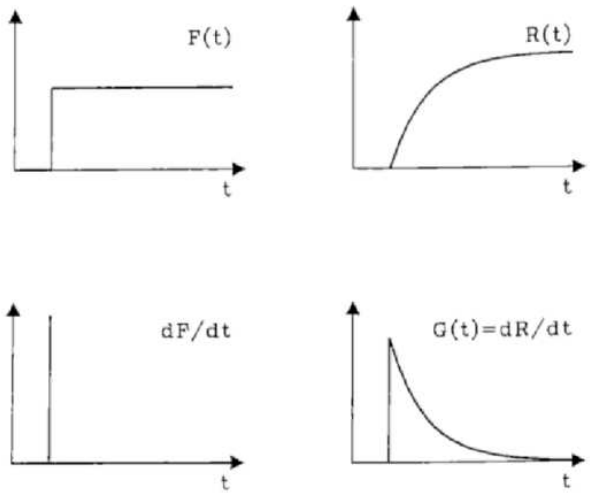

Figure 1.1: On top: *step function* (left) *and associated response function* (right). On bottom: *impulsive forcing* (left) *and Green's function* (right). (Source: Hasselmann et al., 1993)

The Green's function approach is widely used in several fields of physics, from quantum mechanics to signal processing. In climate change literature the impulsive IRF is introduced to approximate the results of a fully coupled atmosphere-ocean model in an highly efficient way from the computational point of view. For example, in Hasselmann and colleagues multidisciplinary discussion on optimal CO_2 emission path (Hasselmann et al., 1997), an IRF model has been used to define the climate module in the coupled climate-economic cost model they implemented. The idea is that the response function approach, differently from other kinds of approximation, does not implicate any *a priori* loss of information compared to the full non linear system. It represents a first-order reduction in the system response, that, under the small perturbation hypothesis, is always permissible: as long as the linear regime is guaranteed, the IRF and the full climate model from which the reduced one is defined, will be the exact substitute of one another.

Hooss et al. (2001) extended Hasselmann et al. (1997) IRF model, by including explicitly some major non-linear effects related to the carbon cycle (*i.e.* the effects of ocean and land uptake and the dependence of radiative forcing on carbon dioxide concentration). Moreover, instead of representing the climate state with a unique global mean variable, a set of two-dimensional fields is considered, by conveniently separating spatial and temporal variability. As in Hasselmann et al. (1997), also in this case the response function is defined following the same procedure proposed in Hasselmann et al. (1993). The response function may be written exploiting some analytical approximation, which is calibrated by fitting the results of some empirical experiments.

The analytical relation between the Dirac δ function and the Heaviside step function (see figure (1.1)) is implied in:

$$x(t) = \int_0^t F(t')\mathcal{G}(t-t')\,dt' = \int_0^t \frac{dF}{dt'}(t')\,R(t-t')\,dt' \tag{1.4}$$

Here, $R(t)$ is the linear response function to a step function forcing, and $\mathcal{G}(t) = \frac{dR}{dt}$ is the impulsive response function of the system. Moreover, under the linear assumption, it is always possible to represents $\mathcal{G}(t)$ and $R(t)$ as a superposition of individual modes:

$$\mathcal{G}(t) = \sum_j \alpha_j\, e^{-\mu_j t} = \sum_j \mathcal{G}_j(t) \tag{1.5}$$

$$R(t) = \sum_j \frac{\alpha_j}{\mu_j}(1 - e^{\mu_j t}) = \sum_j R_j(t) \tag{1.6}$$

To evaluate the shape of the Green function, a choice should be done on the empirical experiment on which the parameters of the mode decomposition (1.5)-(1.6) are calibrated. One option is to exploit the doubling step forcing experiment, which is an usual test performed to evaluate climate model performance. In this way the calibration is performed on the step response function, and then from $R(t)$ the shape of $\mathcal{G}(t)$ is deduced. Another possibility is to directly introduce the mode decomposition for $\mathcal{G}(t)$ (equation (1.5)) in equation (1.1), and to infer the decomposition parameters comparing the analytical function with the results from some transient CO_2 simulations. Hasselmann et al. (1993) have considered both options and have preferred the second one for their estimation of the cold start error. Analogously Hooss et al. (2001) have defined their IRF model calibrating it against a simulation with a prescribed ramping CO_2 concentration: from preindustrial value the concentration is increased exponentially up to the fourfold reference level and then kept constant.

The response function approach has been proposed also to define some metrics for the evaluation of climate change effects. The emission metrics are simple tools to quantify the impact of changes on climate due to the effects of different GHG species, and are widely used in multidisciplinary assessments. Once again, the idea is to represent with a simple

equation the dynamics of the complex climate system. The IRF is deduced from a full model integration and then the responses to different forcing are compared: by considering the ratio between the response due to a generic GHG species and the one due to carbon dioxide, an index which quantifies the "equivalent CO_2 response" can be defined.

Originally this approach was applied to define the relative radiative forcing due to a generic radiatevely-active gas emitted in the atmosphere, *i.e.* the so-called "Global Warming Potential" (*e.g.* Smith and Wigley, 2000a,b). Then the same concept was extended to surface temperature in order to deduce a metric valid to quantify the climate impact from emission: the "Global Temperature Change Potential" (Shine et al., 2005). Of course, the estimate of the response function is a focal point for the definition of these metrics. The analytical estimation of the response function strongly depends on the full model choice and experimental design exploited for fitting the parameters. This yields a huge spread in the evaluation of the IRF and thus in a non-univocal estimate of the metric values (Olivié and Peters, 2013).

The common theme of the studies cited above is to find a convenient strategy to reduce the dimensionality of the problem. In our case the focus is different. The response function represents the fundamental response of the system to a forcing: once we know it, at least in principle, we are able to estimate the response to whatever forcing. In Branstator's words (2014, p.8811), "*by learning about the response to short-lived pulses, one is learning about the building blocks that when combined give the response to any temporally varying source*". In this sense, being able to extrapolate the shape of the Green's function of the atmospheric system should allow us to gain some insight on the signature of the CO_2 effects on climate system. For this reason we have used a much more direct approach. Instead of applying some analytical approximation on a selected mean quantity (*e.g.* global mean surface temperature or sea level height), we exploit a simplified version of a global circulation model to study how the system responds to a pulse of CO_2 concentration. By conveniently analysing the output of a set of pulse experiments, a full mode of both spatial and temporal variability will be detected and recognised to include the pulse effect, and so defined as the response function of the system.

1.2 The time scale of the atmospheric response

Under the action of changes in the radiative forcing, the components of the Earth System react on a wide range of time scales. The atmosphere shows a fast adjustment, while the deep ocean, with its huge thermal inertia, exhibits a response time scale of several hundred of years or more.

Coupled atmosphere-ocean general circulation models offer a powerful tool to estimate the typical time scale involved, and in the literature several studies can be found discussing

this topic (*e.g.* Manabe et al., 1991; Stouffer and Manabe, 1999; Stouffer, 2004). A widely used approach is to impose some transient forcing to the system and to study how the whole interacting Earth system, or just some components of it, reacts. The issue in this case becomes the computational cost: the more complete the representation of the Earth system and the longer the time scale examined, the more demanding the simulations become.

However, a number of simplified approaches can also be found in this framework. For instance, Held et al. (2010) idealize the separation between the fast and the slow climate response with a simple two-box-model and then test their hypothesis by forcing a GCM with an abrupt change from present day to pre-industrial CO_2 value: a fast component (with an e-folding time of about 5 years) turns out to be the dominant component, whereas a much slower "recalcitrant" component emerges far beyond the stabilization of the forcing.

The representation of the response function as a superposition of individual modes (as in equation (1.5)-(1.6)) implicitly carries an estimate of the different time scale involved. Indeed, if just the first two terms in the time series in equation (1.5) are retained:

$$\mathcal{G}(t) = \alpha_1 \, e^{-\mu_1 \, t} + \alpha_2 \, e^{-\mu_2 \, t}$$

the constants μ_1^{-1} and μ_2^{-1} may be interpreted as the typical time scale involved in the response to the radiative forcing.

In the previously mentioned study by Hasselmann et al. (1993), the authors identify two different sets of values for μ_1^{-1} and μ_2^{-1} depending on the kind of experiment performed to estimate the response function. The typical time scale for the fast response ranges between 1.2 years and 2.86 years, while the slow mode shows an estimated e-folding time scale between the 23.5 and the 41.7 years. In the same way, also Hooss et al. (2001) suggest an estimate for the mean surface temperature response characterized by a fast time scale of 12 years and a slow one of 400 years. Voss and Mikolajewicz (2001) on top of their analysis on long term effects of CO_2 increase on a coupled simulation output, estimated the fast adjustment time constant varying between 13 and 20 years, and the long one between 660 years and 990 years, depending on the amplitude of the carbon dioxide forcing.

These examples show that the estimate of these parameters is highly uncertain, as extensively analysed by Olivié et al. (2012). Even if the distinction in fast and slow mode is a prominent feature of all the coupled general circulation model they have examined, the mode characteristics are not univocally identified. The spread in the values of the parameters defining the two modes reflects the differences in the general circulation model formulation and experimental design. For instance, in the just cited work by Voss and Mikolajewicz (2001) the only difference between the two experiments is the shape of the CO_2 path: in one case the maximum CO_2 concentration value is twice the reference value, while in other case it is four times as high.

The byproduct of the analysis performed in this work is to propose our estimate for

the typical time scale involved in the climate response to CO_2 forcing, and in particular, given the adopted experimental setup, the focus will be on the fast atmospheric-driven component.

Chapter 2

Model and Experimental Setup

The numerical experiments in this research have been performed with the Community Earth System Model (CESM). The CESM is the fully coupled Earth System Model developed at the National Center for Atmospheric Research (NCAR) (Hurrell et al., 2013). It consists of different model components, each of them representing the various components of the real Earth System: together with atmosphere, ocean, land, and sea ice, also biogeochemical fluxes, land ice and a "high-top" atmosphere can be accounted for in a fully coupled Earth System experiment.

Each model approximates the phenomena observed in nature by solving the equations which analytically represent those phenomena. Depending on the nature of the considered phenomenon, either a purely deterministic or empirical equation is integrated. Each model component is then coupled to the other in order to represent the actual exchange and conservation of mass and energy, which characterize the real Earth System dynamics.

Given the focus of this study, a simplified version of the CESM has been used here. Instead of a fully coupled atmosphere-ocean model, the active atmosphere component is coupled with a one layer ocean, together with a fully active sea-ice component, while the land surface model is necessary to account for the energy fluxes at the surface. The slab ocean configuration has been demonstrated to lead to a good agreement in equilibrium climate sensitivity study in respect to a full climate model (Danabasoglu and Gent, 2009), with the advantage of being much less computationally demanding.

An overview of the model will be presented in the following sections of this chapter, together with the details of the experimental setup exploited in this research framework, and a short review on the statistical technique adopted in the analysis of the data.

2.1 Model overview

As already said, the slab ocean configuration is made up of a fully active atmosphere, land and sea ice model coupled with a simplified ocean model.

The atmosphere component of the CESM is the Community Atmosphere Model (CAM). In this case CAM version 4 has been used (Neale et al., 2010). As usually true for all the numerical model of the atmosphere, CAM is made up of two main building blocks: the *dynamical core* and the *physical parametrization suite*. While the first one solves numerically the equations representing the fluid motion and thermodynamics on a discrete horizontal and vertical domain, the second one represents sub-grid processes and other processes not explicitly included in the dynamical core, by introducing some convenient parametrization. Processes like radiative transfer, boundary layer turbulences, convection and cloud physics are typically treated in the physical parametrization suite, while the motion of the air mass under the adiabatic and frictionless hypothesis together with the passive tracer transport are solved by the dynamical core.

Different choices can be done regarding the prognostic variables which represent the state of the fluid, and hence the equations for the fluid motion to be solved, the algorithms used to integrate those equations, and the spatial and temporal discretization. This choice defines which dynamical core is implemented in the model. CAM4 can be configured to use a finite-volume, a finite-element or a spectral transform (Eulerian or Semi-Lagrangian) dynamical core. The choice between these options should be done considering a number of aspects, (*e.g.* computational demand, need in resolution, *etc.*), however there is no consensus in the scientific community on a single approach being superior for all, or even a single, application.

In CAM4 the dynamical core and the physical parametrization suite are totally independent and their coupling strongly depends on the chosen dynamical core. Following Williamson (2002), if we consider a prognostic variable ψ (*e.g.* the temperature or the horizontal velocity component), the evolution in time of that variable can be written as:

$$\frac{\partial \psi}{\partial t} = D(\,\psi\,) \,+\, P(\,\psi\,) \tag{2.1}$$

where D and P respectively represent the dynamic component and the parametrization one. The two "engines" can be coupled following two different approaches: the *process-split* and the *time-split*. In the first case, both the parametrization suite and the dynamical core make their computation on the values of the prognostic variables at the previous time step $(n-1)$, while in the second one the computation is performed sequentially, using the one the output by the other component. The process-split approach can be summarized as:

$$\psi^{n+1} = \psi^{n-1} + 2\Delta\, tD(\psi^n, \psi^{n-1}) + 2\Delta\, tP(\psi^n, \psi^{n-1}) \tag{2.2}$$

Actually both D and P also depend on ψ^{n+1}, so equation (2.2) results in a complicated implicit equation. In practice, the computations from the physical parametrization suite are performed first, giving an "effective" forcing which enters in the dynamical core.

On the other hand, the time-split approach can be summarized as:

$$\psi^* = \psi^{n-1} + 2\Delta\, t\, D(\psi^*,\, \psi^n,\, \psi^{n-1}) \tag{2.3}$$

$$\psi^{n+1} = \psi^* + 2\Delta\, t\, P(\psi^{n+1}, \psi^n, \psi^*) \tag{2.4}$$

With an operator notation, the two approaches can be respectively written as:

$$\text{process-split} \qquad \psi^{n+1} = D\left[\psi^{n-1},\, \frac{P(\psi^{n-1}) - \psi^{n-1}}{2\Delta\, t}\right] \tag{2.5}$$

$$\text{time-split} \qquad \psi^{n+1} = P\left[D(\psi^{n-1}, 0)\right] \tag{2.6}$$

The parametrization suite in turn is made up of several sub-components:

$$P = [M,\, R,\, S,\, T]$$

each of them representing different processes: M parametrizes moist processes (*e.g.* convection and condensation), R accounts for cloud and radiation parametrizations, S computes the surface fluxes which acts as boundary conditions for the turbulent mixing component T. While the coupling between the dynamical core and the parametrization suite can be either time split or process split based, each sub-components of the parametrization suite is in any case coupled with the other through time splitting. Thus, again exploiting Williamson's notation, by explicitly considering each component entering in CAM computation, equations (2.5) - (2.6) become:

$$\text{process-split} \qquad \psi^{n+1} = D\left[\psi^{n-1},\, \frac{T(S(R(M(\psi^{n-1})))) - \psi^{n-1}}{2\Delta\, t}\right] \tag{2.7}$$

$$\text{time-split} \qquad \psi^{n+1} = T\left(S\left(R\left(M\left(D\left(\psi^{n-1}, 0\right)\right)\right)\right)\right) \tag{2.8}$$

The choice of the dynamics-physics kind of coupling strongly depends on the chosen dynamical core: in general a process-split approach is used for spectral transform dynamical cores, while the time-split one is preferred for the finite volume one.

In the slab ocean configuration, the ocean is represented as a layer of motionless water (*i.e.* the mixed layer), with fixed temperature, salinity, and depth. The main process represented is the heat exchange with the other components of the system: especially atmosphere and sea ice. No currents, advection and diffusion processes, and deep ocean dynamics are considered. The computational cost of the simulations results strongly reduced, giving anyway a realistic boundary condition for the atmosphere, especially when sensitivity-like experiments are performed.

The slab ocean model (SOM) solves the heat balance relation:

$$\rho_0\, c_p\, h\, \frac{\partial T}{\partial t} = F_{net} + Q_{flx} \tag{2.9}$$

where h and T are respectively the mixed layer depth and temperature, F_{net} is the net surface heat flux, and Q_{flx} is the heat transport convergence, *i.e.* the flux of heat across

the local volume of the simplified ocean. As described in Bitz et al. (2012), unlike the past SOM formulation, in this version of the model the variables describing the one-layer ocean are climatological monthly mean from a fully coupled simulation rather than data from observational dataset. This choice allows to avoid inconsistencies between the observed mixed layer state and the simulated model climate.

The sea ice component of the CESM is CICE - Community Ice CodE (Hunke and Lipscom, 2010). Several aspects of the sea ice evolution are accounted for: the dynamics (*i.e.* the motion of the sea ice due to the balance between the forces acting on it, both internal and external), the thermodynamics (*i.e.* the sea ice growth/melting rates and the vertical temperature profile), the transport, and the thickness distribution. All these aspects have an important impacts in terms of climate change and variability, acting on key processes as the surface albedo effect or the freshwater exchange with the ocean. Exploiting a fully active sea ice component also in a simplified slab ocean framework has become necessary once a simulated mixed layer state has been introduced, in order to have a full numerical consistency.

A fully active land model is necessary to provide the correct surface fluxes for the atmosphere. CLM, the Community Land Model, is the land component of the CESM (Oleson et al., 2010). The land surface actively interacts with the other components of the Earth System in terms of energy and water exchange and biogeochemical cycles on a number of temporal and spatial scale. In order to investigate all these aspects an heavy parametrization is introduced to represent the different land surface elements interacting with the system (*e.g.* kind of surface, kind of soil, kind of vegetation and so on) and their properties. Finally, all these components interact through cpl7, the CESM coupled/driver (Craig et al., 2011). The coupler allows the exchange of data between the components and to deal with all the related numerical issues: regridding/interpolation of the fields, flux computation, coupling frequencies, temporal sequencing and so on.

2.2 Experimental setup

2.2.1 CAM Eulerian Dynamical Core and Model Resolution

In this research, we have exploited the Eulerian spectral transform (EUL) dynamical core of CAM4. The current version of the EUL dynamical core implements a finite difference numerical scheme for vertical and time differentiation, and a *spectral transform method* for horizontal differentiation. The model integrates the primitive equations to derive the value of the prognostic variables (*i.e.* vorticity, divergence, temperature, and logarithm of the surface pressure) together with three diagnostic equations for geopotential height, vertical pressure velocity (ω), and vertical velocity for advection ($\dot{\eta}\frac{\partial \eta}{\partial p}$).

The temporal differentiation scheme is a semi-implicit leapfrog. The primitive equation are linearized against an isothermal and isobaric reference state: the linear terms are then treated implicitly by averaging in time between the next and the previous time step, while the non-linear terms are differentiated using a centered difference scheme.

In the vertical dimension CAM4 implements the hybrid coordinate system (Simmons and Strüfing, 1983): the vertical levels are terrain-following near the surface and become pure pressure at a certain point up to the top of the air column. The vertical coordinates are defined implicitly as those levels η_k which pressure $p(\eta_k)$ at each time step is equal to:

$$p(\eta_k) = p_0\, A_k + p_s\, B_k \qquad\qquad k = 1, 2, \ldots, n_{lev} \tag{2.10}$$

where p_0 is a pressure reference value, p_s is the actual surface pressure at each time step, while A_k and B_k are a set of fixed parameters modulating the shift from the terrain-following regime to the pure pressure one. The central finite difference scheme applied in the vertical is defined so that the global integrals of total energy and mass are conserved. For the details see Williamson and Olson (1994), and Boville and Bretherton (2003).

In general the input/output process of the model is performed on a grid-point domain (longitude and latitude): the physical parametrizations - which in the process-split framework are computed first at each time step - and the dynamical non-linear terms are indeed computed on the longitude-latitude domain, but the horizontal differentiation and the linear terms are computed on the spectral domain. At each level and for each time step t, the prognostic variables and the non-linear product terms in the primitive equations are written as a truncated series of spherical harmonic functions, and, by exploiting the algebraic properties of the harmonic functions, the horizontal derivatives are computed. At this point the values of the prognostic variable spectral coefficients at time $t + \Delta t$ are known, and transformed back to the grid-point domain (figure (2.1)). For a generic time dependent variable ψ the decomposition in spherical harmonic functions may be written as:

$$\psi(\lambda, \phi;\, t) = \sum_{m=-M}^{+M} \sum_{n=|m|}^{\mathcal{N}(m)} \psi_n^m(t) P_n^m(\sin\phi) e^{i\, m\, \lambda} \tag{2.11}$$

In equation (2.11), λ and ϕ are respectively longitude and latitude, the quantities ψ_n^m are the time-dependent spectral coefficients, P_n^m is the associated Legendre polynomial, m represents the number of waves in the east-west Fourier decomposition, while n is the meridional index. In general, the higher the order of the truncation in (2.11), the smaller the scale captured by the approximated field will be. Different choices on the truncation strategy may be made, the most common being the triangular and the rhomboidal ones:

$$\begin{aligned} &\mathcal{N}(m) = M && \text{Triangular Truncation} \\ &\mathcal{N}(m) = M + |m| && \text{Rhomboidal Truncation} \end{aligned}$$

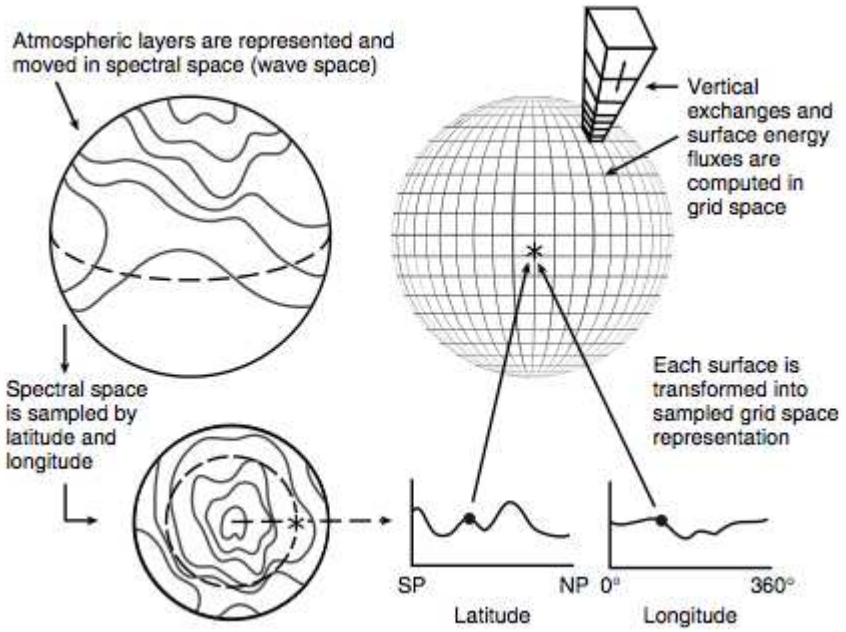

Figure 2.1: *Schematic of the spectral transform technique: computation on the horizontal are performed in the spectral domain, while in the vertical a finite difference scheme is applied.* (Source: Edwards, 2011)

In the first case each wave is solved with the same resolution (*i.e.* for each zonal number m the same number of spectral coefficients are retained), while in the second one shorter waves are less resolved than longer ones, (*i.e.* the higher m, the less spectral coefficients are considered). Generally the notation R or T, followed by the chosen value of M, is used to distinguish across the two approaches. Consistently, to a given spectral resolution corresponds a bi-dimensional *Gaussian grid*: the discretization in the zonal direction is defined through the Fourier transform, while the estimation of the spectral coefficient ψ_n^m through Gaussian quadrature implicitly determines the discrete latitudes ϕ_k. This brief summary on the spectral transform approach is intended to provide a general insight on the model used in this research, a detailed description of the numerical techniques and of the related theory can be found on several publications, for example Machenhauer (1979) and Washington and Parkinson (2005).

In this study a T31 grid is used. This represents a common choice in low resolution studies and it corresponds to 96×48 grid points in the longitude-latitude domain (approximately a resolution of 3.75°). In the vertical, the standard CAM4 discretization is adopted, with 26 hybrid levels which nominally covers up to $\sim$ 3 hPa. The pure pressure region starts at about 100 hPa, while the terrain-following component becomes stronger going down to the last level, for which $p(\eta_k)$ depends just on the actual surface pressure p_s.

CLM shares the same horizontal resolution of the atmospheric component, while the slab ocean and the sea ice model run on a 3 degrees Greenland pole grid, which is the

natural choice to match the global grid from the T31 truncation.

2.2.2 Initialization and Forcing

Before performing the actual experiment, it is necessary to define correctly the initial conditions. The choice of the initial conditions is a crucial aspect in the experimental design. If the state of the system on which the numerical integration is performed is not at the equilibrium with the world described by the model, numerical instabilities and non-physical signal may arise in the simulation. The common practice in climate studies is to perform a *spinup* of the model. Starting from scratch initial conditions, the model is run without imposing any forcing, until the simulated state is consistent with the model physics and climate. For some insights on the general philosophy about the spinup technique see Simmonds (1985).

For our focus the reference state of the system is given by the present day conditions (*i.e.* nominally the 2000 condition). To perform the spinup, starting from a standard 2000 state, the model is run with the boundary conditions kept constant. In this way the model will recursively simulate the 2000 condition, relaxing towards its own climate and reaching a numerically stable "2000-state".

Generally, the more complex the system represented by the model, the longer the spinup period will be. An uncoupled atmospheric model arrives at the equilibrium after few days, for a fully coupled atmosphere-ocean model hundreds of years are needed to reach the numerical stability. In the slab ocean framework, we have chosen a 30 year spinup. Figure (2.2) shows the evolution of the surface temperature in the spinup period (blue line) together with the radiation flux at the top of the model (red line). The radiation balance at the top of model (*i.e.* at the top of the atmosphere - TOA) is a typical metrics used to check the model spinup: if there is no imbalance in the energy flux, it means that all the sources and sinks of energy due to numerical processes have been dissipated and the system has reached a consistent equilibrium. The first five years are characterized by a transient warming, and consistently by a decrease of the TOA radiation balance, until a plateaux is reached. The state of the system after more than two decades of plateaux, *i.e.* for January of the model year 2030, has been selected as the initial condition for the experiment.

The aim of the experiments is to detect the response function of climate system in terms of response to an impulsive forcing. To approximate a pulse of carbon dioxide concentration, we have decided to introduce in the system a Gaussian-shaped peak of CO_2. Thus, the analytical equation for the impulse is simply given by:

$$C(t) = \mathcal{C} \exp\left[-\frac{(t - t_0)^2}{2\,\Delta t}\right] \tag{2.12}$$

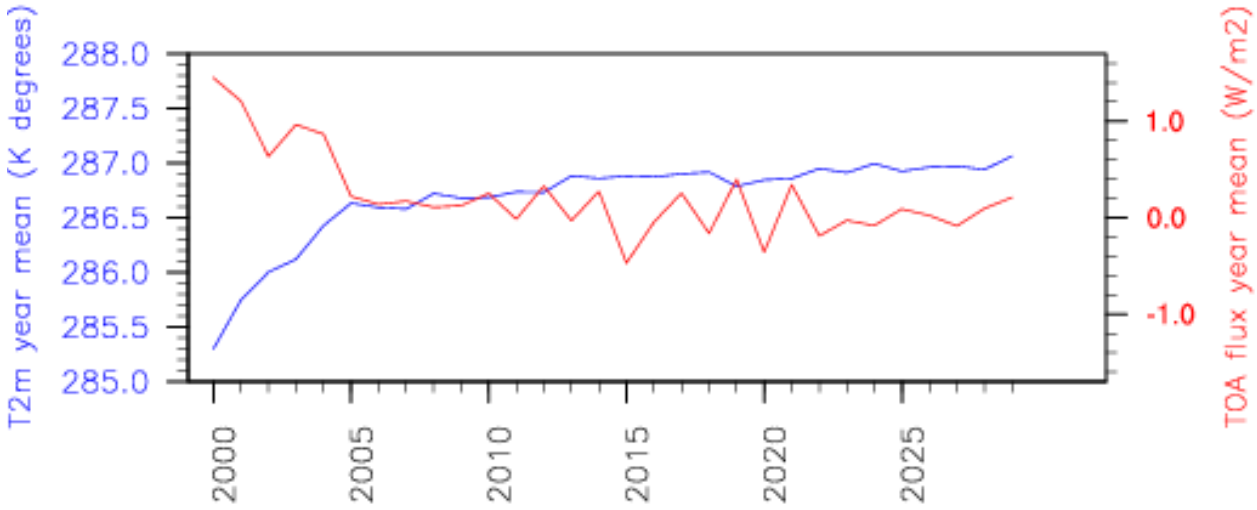

Figure 2.2: Blue line: *Yearly average global mean near surface* (2 m) *temperature* (K) *in the spinup period.* Red line: *Yearly average global mean energy flux* ($\mathrm{W\,m^{-2}}$) *at the top of the atmosphere in the spinup period. After the transient period the system reaches the equilibrium.*

where $\mathcal{C}$ defines the amplitude of the pulse, t_0 is the time at which the peak will be maximum, and Δt is the width in time of the peak. The choice of the Gaussian bell parameters is a critical issue. The width Δt should be small enough in comparison with the whole duration of the simulation for the function in equation (2.12) to be a good approximation of a δ-function. For this reason we have fixed Δt to be one year, as against a total duration of the simulation of 41 years (from model year 2030 to model year 2070). At the same time the amplitude $\mathcal{C}$ should be large enough to have a significant increase of the forcing in a short time, but it should be consistent with the linearity constraint. As noticed by Hasselmann et al. (1997) a doubling in CO_2 concentration corresponds to an increase in the radiative forcing of about $4\,\mathrm{Wm^{-2}}$, which is a little more than 1% of incoming solar radiation ($\sim 340\,\mathrm{Wm^{-2}}$). For this reason the linear approximation turns out to be adequate for our purposes. Starting from a reference present day value of 369 ppm, the value of maximum CO_2 has been fixed to 738 ppm. As usual, together with the forced experiment, a companion-one, with all the boundary condition kept constant, is considered. This control experiment is necessary to provide a benchmark against with the forced simulations can be compared.

To summarize the structure of the experiment, after a 30 year spinup, from the stable model conditions for the present day climate, we have branched off a control experiment - which represents a recursive 2000 condition -, and a forced one where all the boundary conditions are kept constant except the CO_2 concentration, which follows the forced path described above. To be able to assess the robustness of the analysis we are going to perform,

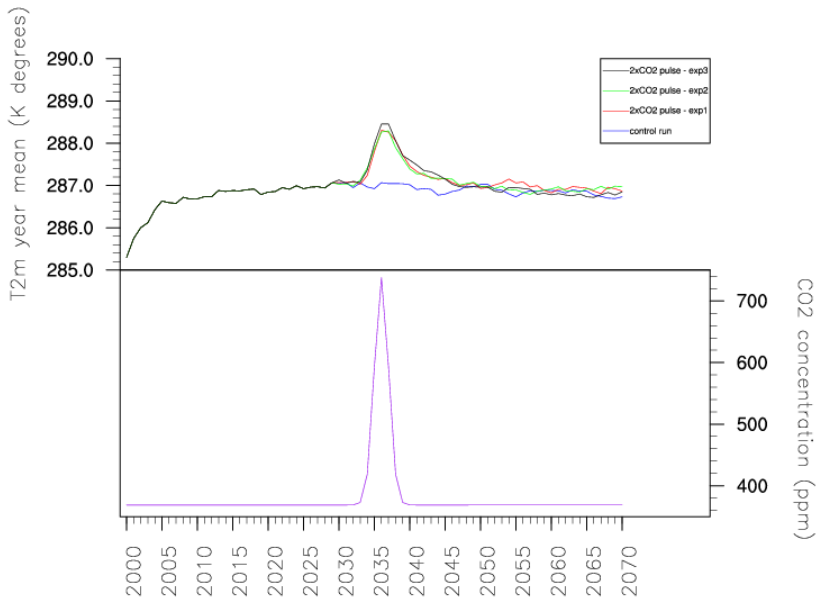

Figure 2.3: On top: *Yearly average global mean near surface* (2 m) *temperature* (K) *for the control experiment and the three forced ones after the first 30 years of model spinup.* On bottom: *Path of carbon dioxide concentration forcing* (ppm).

a set of three different initial conditions from the spinup are considered to initialize the forced experiment. The three initial conditions are three possible realization of the 2000 condition from the control experiment, thus they can be considered totally equivalent from both a physical and a statistical point of view. In figure (2.3) the composit of the global mean 2m temperature for the set of forced simulations and for the control one is shown. The model is sensitive to the applied forcing and the differences between the three forced simulations may be interpreted as due to the internal variability of the system.

2.3 The Empirical Orthogonal Function

The Empirical Orthogonal Function (EOF) analysis is a powerful statistical method widely used in atmospheric and climate science. In other fields this technique is often known as Principal Component Analysis (PCA). The basic idea is to split a space and time dependent data field in a set of independent spatial patterns together with a set of uncorrelated time series. In this work this technique will be used to analyse the output from the pulse experiments described in section (2.2), for this reason it is useful to give some insight on it before discussing the actual results we have obtained.

Suppose to have a set of data in the discrete time and spatial domain, as for instance the output of a numerical simulation. If the spatial domain is made up of m grid points, we can define a set of n *synoptic* vectors x_j, each of them representing the state of the

atmosphere at each *j-th* time step.

$$\mathbf{x}_j = \begin{bmatrix} x_1(t_j) \\ x_2(t_j) \\ \vdots \\ x_m(t_j) \end{bmatrix}, \qquad j = 1, 2, \ldots, n$$

The synoptic vectors can be organized in a $m \times n$ data matrix $\mathbf{X}$, whose rows will be the time series at each grid point and whose columns will be the spatial map at each time step. The choice between $\mathbf{X}$ and $\mathbf{X}^T$ is arbitrary, given that the notation is kept constant throughout. In this description we will follow the convention and the approach proposed by Navarra and Simoncini (2010).

From linear algebra we know that the rank of $\mathbf{X}$ indicates the number of columns which are linearly independent. Using k to denote the rank, if there are some recurrent patterns in the data, there will be $k < n$ columns linearly independent, the remaining ones being a combination of some fundamental modes. The aim of EOF analysis is to represent the whole set of data in terms of the fundamental modes, defining at the same time how these modes evolve in time.

The rank of a generic $m \times n$ matrix may be computed through the *singular value decomposition* (SVD):

$$\mathbf{X} = \mathbf{U}\mathbf{\Sigma}\mathbf{V}^T \tag{2.13}$$

where U and V, respectively of dimension $m \times m$ and $n \times n$, have for columns the left and right singular vectors, while Σ is a diagonal $m \times n$ matrix, defining the singular values. The number of non-zero singular values is the rank of $\mathbf{X}$.

Let define the anomaly data matrix $\tilde{\mathbf{X}}$ as:

$$\tilde{\mathbf{X}} = \mathbf{X} - \overline{X}$$

where $\overline{X}$ is a vector whose components are the time mean of the original data at each grid point. The *covariance matrix* for the data in $\mathbf{X}$ is:

$$\mathbf{S} = \frac{1}{n-1}\tilde{\mathbf{X}}\tilde{\mathbf{X}^T} \tag{2.14}$$

The components of $\mathbf{S}$ are the covariances s_{ij} between the time series of the field at any pair of space point (i, j). By definition the covariance matrix is symmetric:

$$s_{ij} = s_{ji}$$

and the diagonal elements s_{ii} represent the variance of the series at the *i-th* grid-point. The trace of the covariance matrix, *i.e.* the sum of the elements on the diagonal, gives the

variance of the total field. If we write the SVD for $\tilde{\mathbf{X}}$ and substitute it into equation (2.14) we end up with:

$$\mathbf{S} = \frac{1}{n-1}\mathbf{U}\mathbf{\Sigma}\mathbf{V}^T\mathbf{V}\mathbf{\Sigma}\mathbf{U}^T \tag{2.15}$$

that, for the orthogonality of $\mathbf{V}$, can be reduced to:

$$\mathbf{S} = \frac{1}{n-1}\mathbf{U}\mathbf{\Sigma}^2\mathbf{U}^T \tag{2.16}$$

If we omit the simple multiplicative factor $\frac{1}{n-1}$, equation (2.16) becomes a similarity relation for $\mathbf{S}$:

$$\mathbf{S} = \mathbf{U}\mathbf{\Sigma}^2\mathbf{U}^T \tag{2.17}$$

This last relation shades some light on the reason why the SVD is interesting for our focus. The left singular vectors can be interpreted as a set of orthogonal eigenvectors for the covariance matrix, while the squared singular values, up to a factor $\frac{1}{n-1}$, are the related eigenvalues. Recalling that the trace of a matrix is similarity-invariant - so the trace of Σ^2 is the same of the one of $\mathbf{S}$ -, we have obtained a set of orthogonal eigenvectors for the covariance matrix each of them explaining an amount of variance:

$$\lambda_i = \frac{\sigma_i^2}{\mathrm{Tr}\,(\mathbf{\Sigma^2})}$$

If, as usually is the case, the singular values are arranged in decreasing magnitude, the first column of $\mathbf{U}$ will explain the highest amount of variance, followed by the second one and so on. The number of non zero singular values will be equal to the number of significant orthogonal vectors. The columns of $\mathbf{U}$ are the *Empirical Orthogonal Functions* (EOFs) and can be computed indifferently from the eigenanalysis of the covariance matrix or from the singular value decomposition of the anomaly data matrix: usually this latter option is chosen, being much faster from a computational point of view, especially when a large data space is considered.

Now let us consider $\mathbf{V}$, the $n \times n$ matrix which contains the right singular vectors. For the orthogonality of $\mathbf{U}$, we can write:

$$\mathbf{U}^T\tilde{\mathbf{X}} = \mathbf{U}^T\mathbf{U}\mathbf{\Sigma}\mathbf{V} = \mathbf{\Sigma}\mathbf{V} \tag{2.18}$$

The projection of the anomaly data matrix on the k^{th} EOF is given by the k^{th} column of $\mathbf{V}$, conveniently weighted by σ_k, basically by the variance explained by the k^{th} mode. Each vector of $\mathbf{V}$ represents the *Principal Component* for the related EOF mode.

Symbolically the EOF analysis may be explained in the following terms:

$$\mathbf{X} = \sum_j \mathrm{EOF}_j(x, y, z) \cdot \mathrm{PC}_j(t)$$

The entire data set may be written as a series of spatial patterns mutually orthogonal. A set of coefficients, mutually uncorrelated, describes how the amplitude of each of these

patterns is modulated in time. Each component of the *k-th* column of $\mathbf{V}$ is a coefficient which describes how the *k-th* EOF is modulated time step by time step.

The interpretation of the EOF modes from a physical point of view is not straightforward. It should be always kept in mind that the partition in modes is performed on a statistical basis, so a single phenomenon may contribute to different modes or, *viceversa*, different physical modes may be taken into account in a single statistical pattern. For this reason, the interpretation of the link between the actual physical mechanisms in action and the EOF statistical representation may be simplified by the knowledge of the temporal variability of the real phenomenon. Moreover by definition the EOF modes are orthogonal in space and uncorrelated in time: even if the first one can be directly related to some physical pattern, the subsequent ones will be deformed by the orthogonality constraint. In other words, the EOF analysis correctly reveals on different modes physical phenomena which in nature are uncorrelated in time and space.

Despite these caveats, the EOF analysis represents a widely used method to interpret observed data or simulation output in atmospheric sciences. It allows to treat also large dataset, reducing the dimensionality of the problem to some significant modes. Several applications and generalizations of the EOF analysis may be found in the literature, which partly have been introduced in order to override the restrictions described above. In this study these generalizations will not be used, however for further details on the EOF analysis and its application see Navarra and Simoncini (2010), Hannachi et al. (2007) and references therein.

Chapter 3

Definition of the Atmosphere Response Function

The aim of this experiment is to define the response function of the atmosphere to variations in the CO_2 changes by directly introducing in the system a pulse of carbon dioxide. As already explained, for the experiments to be meaningful we need a pulse of CO_2 which amplitude is small enough to guarantee, at least to a first approximation, the linearity of the response. For this reason doubling in the CO_2 concentration, compared to the reference present day value, has been chosen. Moreover, to have a good representation of an analytical impulse - *i.e.* a Dirac δ function - the pulse has been approximated with a Gaussian function, whose duration in time is much shorter then the duration of the whole simulation. We have performed a set of three different pulse experiments with different, but statistically and physically equivalent initial conditions, together with a control experiment where the boundary conditions are kept constant throughout all the duration of the simulation.

Consistently with several other studies which use the surface temperature as a proxy for the atmosphere response when treating climate sensitivity or climate response to radiative forcing, here we will concentrate on the 2 meter temperature output from our numerical experiments. To detect the response function, we need to separate the forced signal from the internal variability of the system. We have decided to perform an EOF analysis on the results of our simulations, in order to extrapolate one or more modes of variability which can be directly associated with the pulse forcing. The EOF analysis has been performed on both the forced experiments and the control one. The discussion of these results will be presented in the following sections.

3.1 Pulse experiments: EOF analysis

As discussed in section (2.3), the EOF analysis allows to completely describe a time series of data as a set of orthogonal spatial patterns, which appears in the actual realization of the field, conveniently modulated in amplitude. The set of coefficients which amplify or damp the EOF patterns in time are the principal components. It is important to stress that both EOFs and PCs are needed to correctly identify and interpret the results of an EOF analysis, which otherwise can lead to misleading interpretations. As already noticed, we recall here that the EOF modes do not represent physical modes of variability, and to study modes which may have some real physical meaning, the first few ones are usually retained. In our analysis we will consider the first three EOFs for both the forced and the control experiments.

In figure (3.1a)-(3.1c) the first three EOF modes for the control simulation are represented. The first mode explains 15 % of the total variance and in it we can recognize some canonical patterns. For example, we may find a pronounced warm signal over the Equatorial Pacific, together with a wavy pattern over North America and the North Atlantic region. Given that in the control experiment there are no forcings which vary in time, the presence of these signals tells us that these modes are inherent to the internal variability of the climate simulated by the model. Consistently with this interpretation, if we look at the first PC (black line in figure (3.3a)) we notice no definite trend but a clear oscillation around the zero, telling us that the pattern seen in the first mode appears changing sign and amplitude during all the simulations. The second and the third EOF modes explain a similar amount of variance - 7% and 6% respectively. This fact together with the similar shape of the pattern, especially over North America, may suggest that we are looking at two phases of the same oscillatory phenomenon. If that is the case the the related PCs should oscillate in quadrature one in respect with the other, *i.e.* with a shift in phase of 90°. As can be seen in figure (3.3a), the shift between the two time series (*i.e.* respectively the blue and the red lines) is not so evident. This is a further demonstration that the constraint implicit in the EOF analysis may deform the shape of the modes, making the interpretation not straightforward.

Now let consider the results from the forced experiment. The first three EOF modes are shown in figure (3.2a)-(3.2c). The first EOF presents a totally different pattern from the ones seen before. First of all it accounts for a much larger amount of variance: 42%. A definite positive signal is presented anywhere and especially concentrated in the tropical region. The higher order EOFs represent 8% and 7% of the total variance. In the second mode the main features related to the signal of the unforced model climate variability can be found, *e.g.* the dipole signal over North America and North Atlantic, or the elongated structure over the Eurasian continent. In the third mode, the pattern shows a dipole

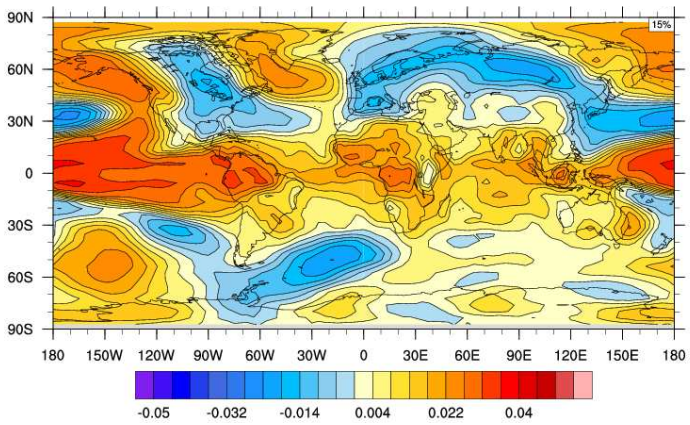

(a) *First EOF mode - control simulation:* 15% *explained variance*

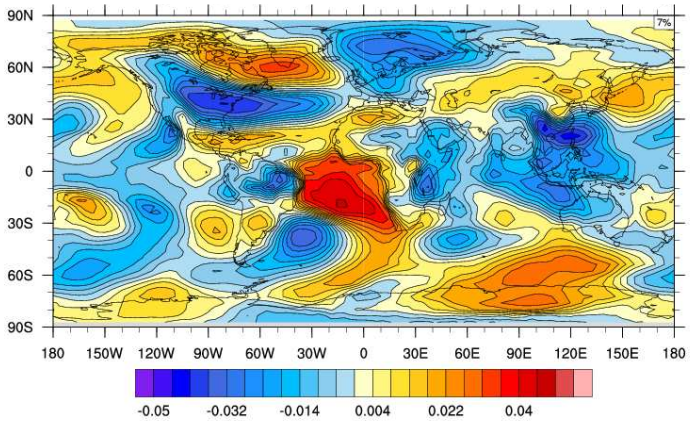

(b) *Second EOF mode - control simulation:* 7% *explained variance*

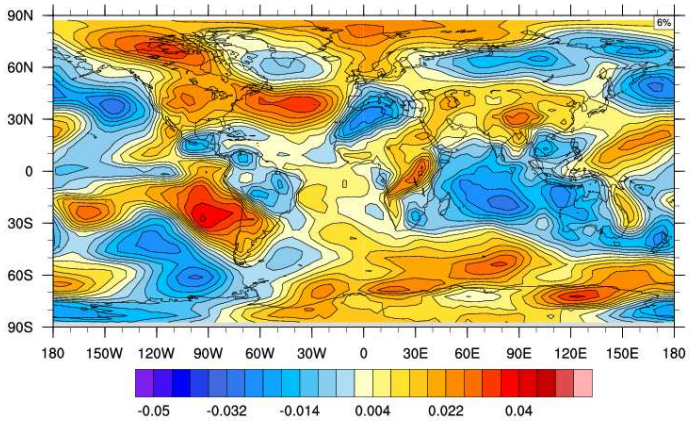

(c) *Third EOF mode - control simulation:* 6% *explained variance*

Figure 3.1: *Near surface* (2 m) *temperature for the control experiment: first three EOF modes.*

structure, with different signs between continental areas at low to mid-latitudes and oceans over high latitudes. It is worth recalling that the sign of the EOF is somehow arbitrary, the total sign of the mode is given by the product of the EOF pattern with the PC time series. To have a more complete picture of the situation, let us analyse the shape of the related PCs (figure (3.3b)).

The first aspect which stands out is that the amplitude of the first PC is much larger than the one of the higher order PCs. The first PC shows a distinct path in time, totally in phase with the forcing. The second PC oscillates around the zero line, while a more interesting signal is the one in the third PC. Indeed the red line in figure (3.3b) seems to behave as the derivative of the black one - the first PC: it is positive while the first PC is increasing and turns to negative while the first PC is decreasing.

To test the robustness of this result, the same EOF analysis has been performed also for the other two equivalent experiments, yielding consistent results both in the spatial and in the temporal modes. The first EOF in all the experiments (figures (3.4a)-(3.5a)) shows a similar pattern, positive in all the domain with some local minima at the high latitudes (*e.g.* over Antarctic peninsula and over North Atlantic). The higher order EOFs explain always a comparable amount of variance (between 6% and 5%). The related spatial patterns show the typical wave signal of the internal variability together with the dipole structure already noted before, even if the separation between these modes is less pronounced than before. The PCs show some familiar features: the first mode is characterized by the same clear distinct peak seen before, while the higher order modes generally oscillate with a much smaller amplitude, with the derivative-like signal being less evident.

The modes described with the EOF analysis often suffer from a geometrical deformation, due to the orthogonality constraint. For this reason it cannot be expected to have exactly the same sharp separation between the modes of two analogous experiments, even if, from a physical point of view, the two set of data describe the same phenomenon. The fact that the first EOF mode in all the performed experiment shows exactly the same features both in time and space, makes us confident to identify in this mode the effective signature of the pulse of CO_2.

But, as already discussed, the response to an impulsive forcing represents the response function of the system to that forcing. Without making any assumption on the shape of the response function, we have deduced it directly from the data, identifying it with the first EOF mode of an impulsive experiment.

3.2 Time scale of the atmospheric response

By looking at the first principal component for the three forced experiments, we may notice that there is a common feature characterizing the response of the system to the

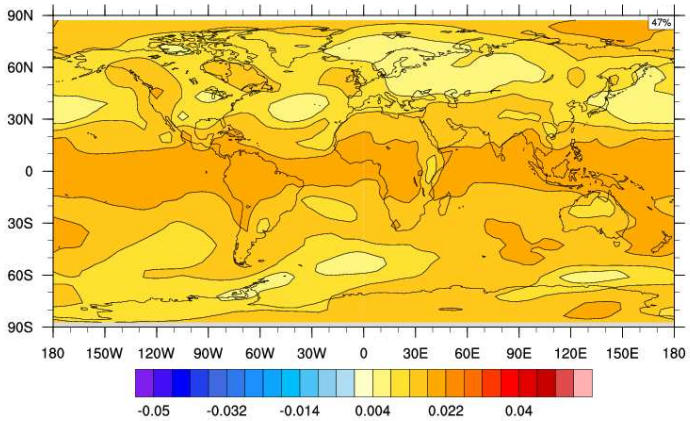

(a) *First EOF mode - forced experiment (test 1):* 47% *explained variance*

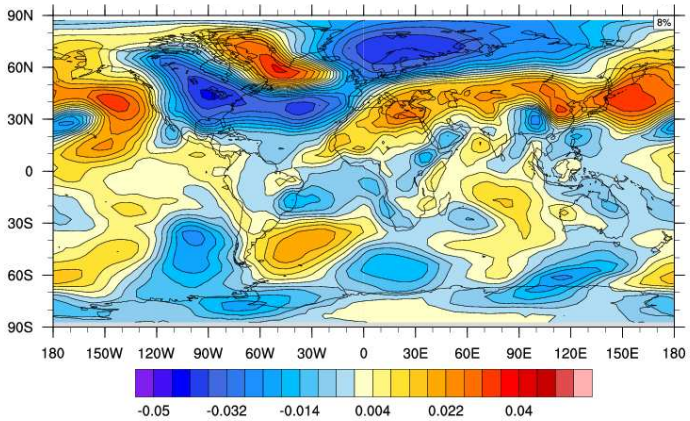

(b) *Second EOF mode - forced experiment (test 1):* 7% *explained variance*

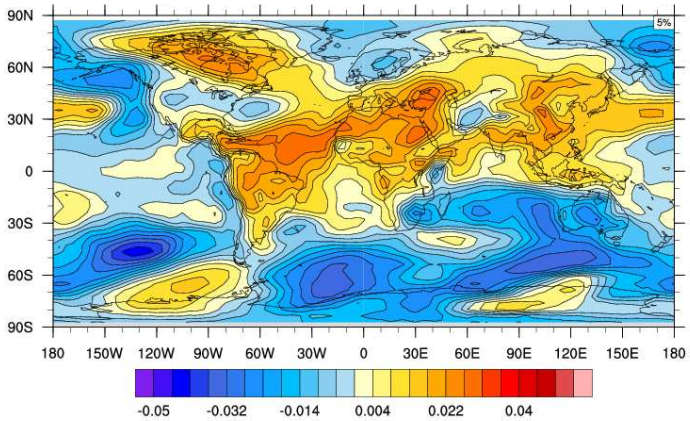

(c) *Third EOF mode - forced experiment (test 1):* 6% *explained variance*

Figure 3.2: *Near surface* (2 m) *temperature for the forced experiment (test 1): first three EOF modes. In the first EOF a positive signal spread in all the domain may be found, while the higher order EOFs show a more complex pattern.*

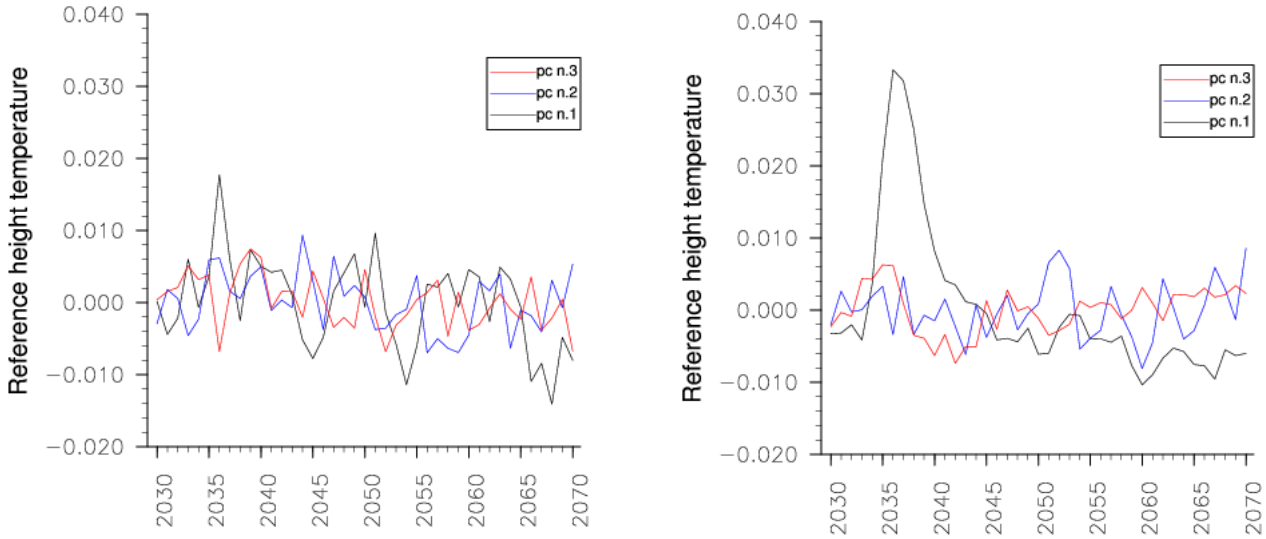

(a) *PC coefficients - control experiment*

(b) *PC coefficients - forced experiment (test 1)*

Figure 3.3: Left: *First three PC coefficients for the control experiment.* Right: *First three PC coefficients for the forced experiment (test 1). In black the first mode PC, in blue the second mode PC, in red the third mode PC. In the left panel no definite trend may be noticed. In the right panel, the first PC mode shows a clear forced signal, while the higher order PCs oscillate around the zero line.*

applied pulse: the time the system needs to recover from the pulse effect. Indeed if we look at the path described by the black line in figures (3.3b)-(3.4d)-(3.5d), the trend due to the forcing seems to become steady after about 15 years.

To test if really after 15 years the effect of the pulse is over, a sanity check can be performed by directly compute an EOF analysis on the same data from the forced experiment, by simply discarding the first 15 years. Here for the sake of simplicity just the results from the first forced experiment are shown. From both the EOF patterns and the PC coefficients (figure (3.6)), neither clear spatial signature nor temporal trend can be found recalling the applied forcing. However, before putting forward any hypothesis, we need to test whether and how this feature is related with the choice we have done to define the shape of the pulse.

In order to do so we have performed a further experiment: instead of a continuous Gaussian, a discrete pulse in carbon dioxide concentration has been considered. From the constant reference value (369 ppm), at the model year 2031 the CO_2 concentration is instantaneously doubled to 738 ppm, and then returned to 369 ppm the following year. Once again to detect the effects of the forcing we compute and EOF analysis. Even if the signal is much more noisy than the one due to the continuous bell pulse, both the spatial patterns (figure (3.8a)-(3.8c)) and the principal component time series (figure (3.7)) share

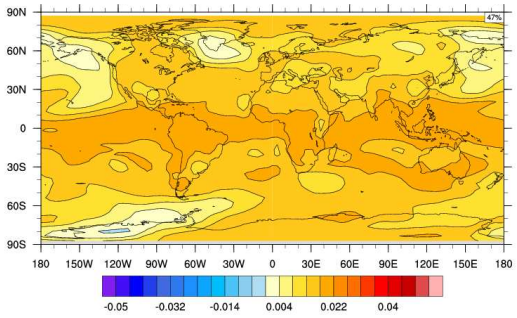

(a) *First EOF mode - forced experiment (test 2): 47% explained variance*

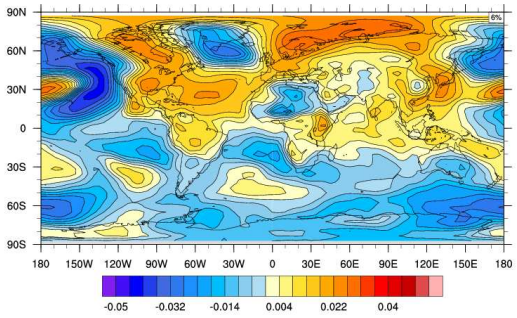

(b) *Second EOF mode - forced experiment (test 2): 6% explained variance*

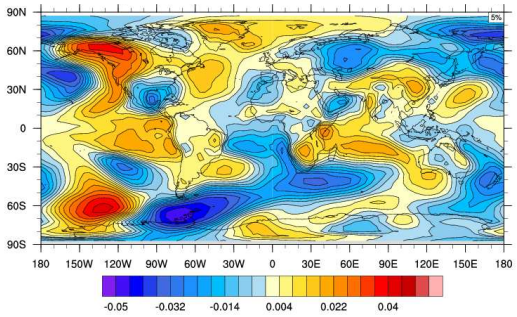

(c) *Third EOF mode - forced experiment (test 2): 5% explained variance*

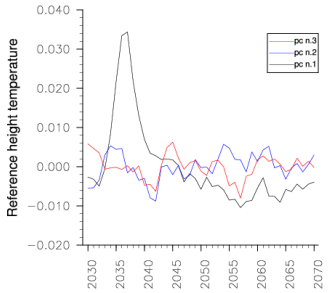

(d) *PC coefficients - forced experiment (test 2): same color convention as in figure (3.3a)-(3.3b)*

Figure 3.4: *EOFs and PCs for the near surface* (2 m) *temperature field of the forced experiment (test 2). These results are consistent with the ones in figures (3.2)-(3.3b)*

the same main features seen in the continuous case. The first EOF mode is characterized by the well-known positive pattern mainly concentrated in the tropical region, while the higher order EOFs show the typical fingerprint of the internal variability. But more surprisingly, also the PCs follow the same path seen in the previous cases: the first PC has a peak which is totally relaxed by the model year 2045, while the higher order PCs oscillate around the zero line with a much smaller amplitude.

The combination of these results show a clear and consistent picture. The effects due the the pulse of carbon dioxide concentration are all concentrated in the first EOF mode. We know that the response of the system to an impulsive forcing is the *Green's function* or, to be more accurate, the *response function*. So it is tempting to identify the first EOF mode of an impulsive experiment as the response function of the system. The interesting aspect here is that these results are independent of the choice of the approximation of the analytical impulse: both with a continuous bell and with the discrete doubling of carbon

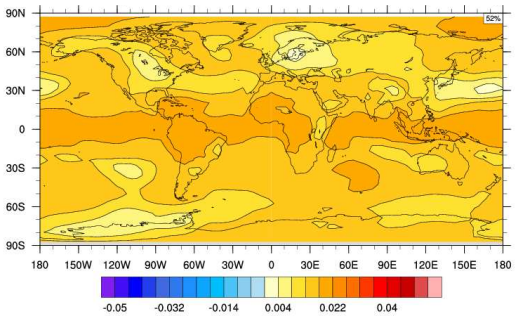

(a) *First EOF mode - forced experiment (test 3):* 52% *explained variance*

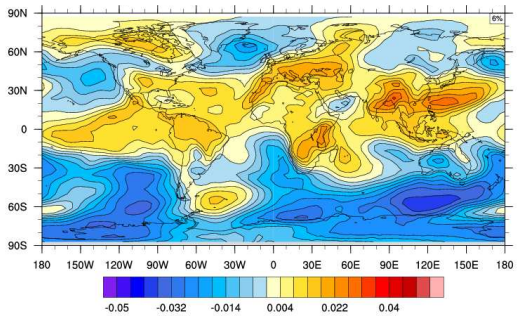

(b) *Second EOF mode - forced experiment (test 3):* 6% *explained variance*

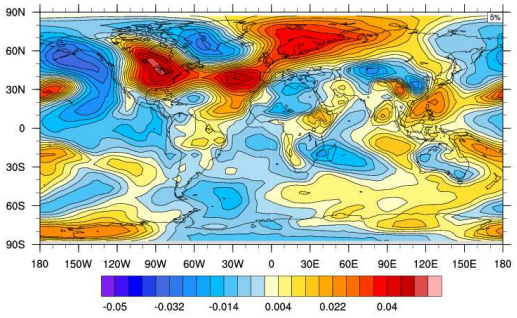

(c) *Third EOF mode - forced experiment (test 3):* 5% *explained variance*

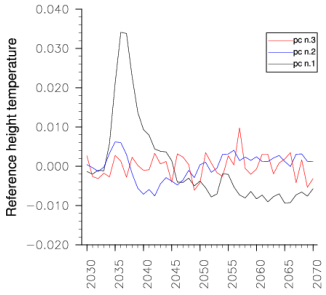

(d) *PC coefficients - forced experiment (test 3): same color convention as in figure (3.3a)-(3.3b)*

Figure 3.5: *EOFs and PCs for the near surface* (2 m) *temperature field of the forced experiment (test 3). Also in this case, the results are consistent with the ones in figures (3.2)-(3.3b)*

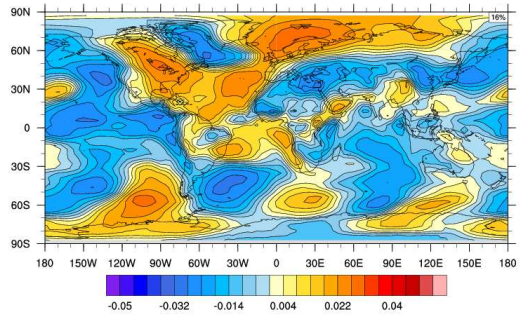

(a) *First EOF - forced experiment (test 1) from model year 2045:* 16% *explained variance*

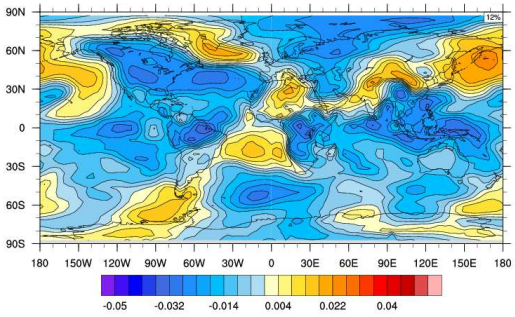

(b) *Second EOF - forced experiment (test 1) from model year 2045:* 12% *explained variance*

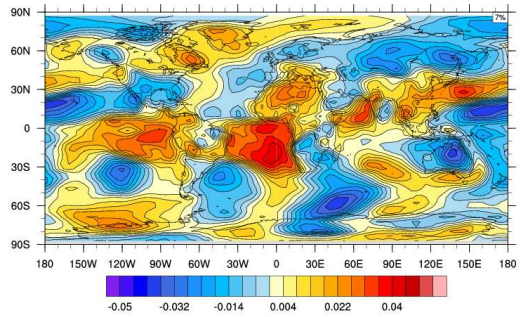

(c) *Third EOF - forced experiment (test 1) from model year 2045:* 7% *explained variance*

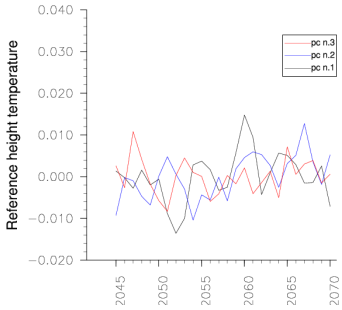

(d) *PC coefficients - forced experiment (test 1) from model year 2045*

Figure 3.6: *EOFs and PCs for the near surface* (2 m) *temperature field of the forced experiment (test 1) after discarding the first 15 years of simulation. Neither spatial nor temporal signature of the forcing may be found.*

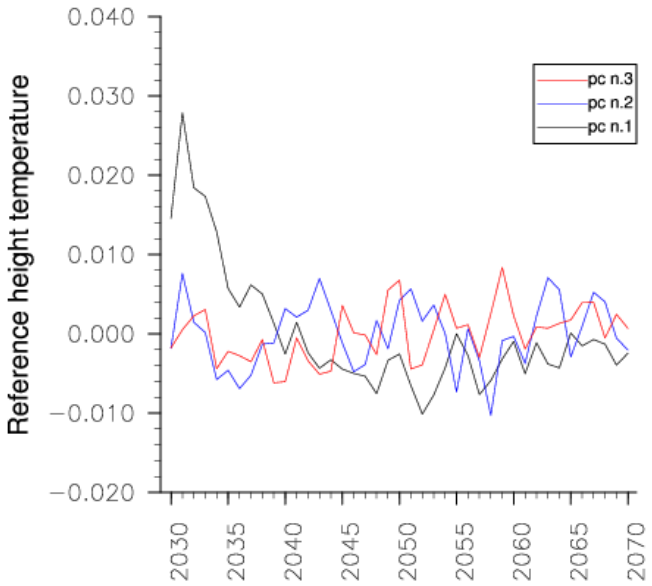

Figure 3.7: *PC coefficients - discrete impulse experiment: same color convention as in figure (3.3a)-(3.3b). The results show the same temporal trend discussed for the experiments accounting for the continuous forcing.*

dioxide concentration the same features have been found. Using a full numerical model, we have been able to define the spatial pattern related to the response function, which gives us an hint on the fundamental response of the atmosphere to the CO_2-related forcing. It is important to stress here that, given the simplified numerical system used for these experiments, only the atmosphere response can be detected. In a slab ocean framework, all the contributions due to the ocean dynamics cannot be accounted for. For this reason, we can interpret the relaxation time we have deduced from the impulsive mode detection as the fast time scale already discussed in section (1.2). This estimate seems consistent with the results which can be found in the literature, and most of all, it is a robust feature of our experiments.

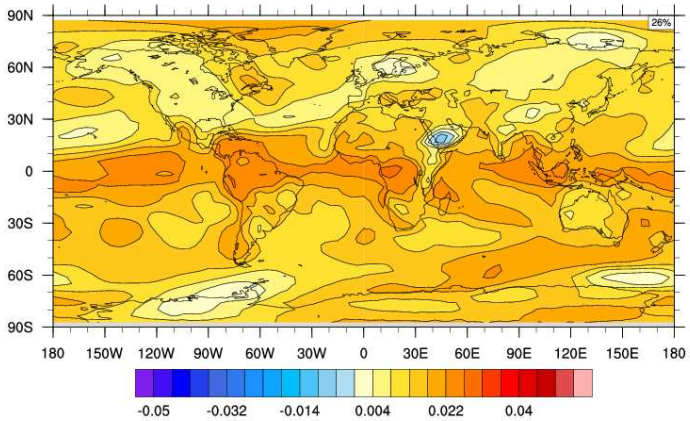

(a) *First EOF mode - discrete impulse experiment:* 26% *explained variance*

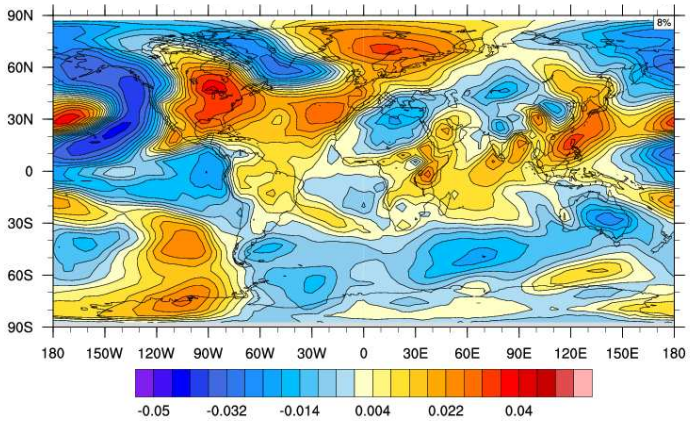

(b) *Second EOF mode - discrete impulse experiment:* 8% *explained variance*

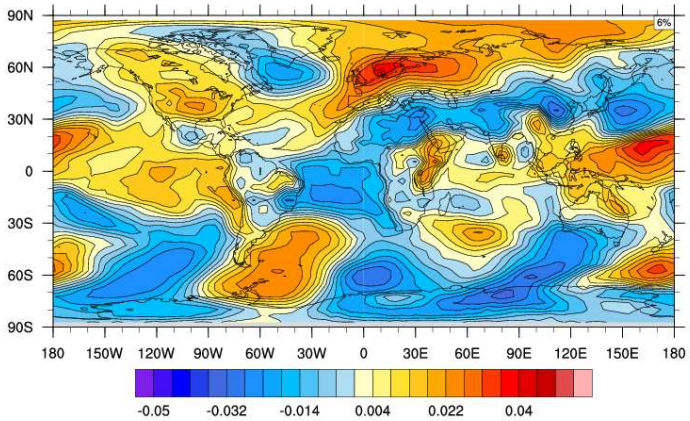

(c) *Third EOF mode - discrete impulse experiment:* 6% *explained variance*

Figure 3.8: *First three EOF modes for the near surface* (2 m) *temperature field of the discrete impulse experiment. These patterns show the same features discussed for the experiments accounting for the continuous approximation of the impulsive forcing.*

Chapter 4

Effects of a Localized CO_2 Forcing

Carbon dioxide is generally considered a well-mixed greenhouse gas: a gas whose typical lifetime is long enough to be homogeneously distributed in the troposphere. For this reason, when the focus is on the atmospheric response to the human-induced radiative forcing, model studies usually consider greenhouse gas concentration as a boundary condition in the simulations. In these cases, a unique homogeneous value which typically varies on a yearly basis, enters in the model representation through the numerical scheme accounting for the radiative properties of the atmosphere.

However, the actual CO_2 distribution shows some spatial inhomogeneity. For example, in figure (4.1) the spatial distribution from satellite data of the mean carbon dioxide concentration for the year 2011 is reported. Even if the differences are small in terms of absolute values - *i.e.* in the order of ~ 5 ppm -, some prominent features can easily be noticed: there is a clear inter-hemispheric gradient increasing from the Southern to the Northern Hemisphere, with some distinct maxima over North America and South East Asia. This feature has been widely discussed in the literature (*e.g.* Denning et al., 1995; Ruzmaikin et al., 2012), and it is mainly related to the location of sources and sinks, both natural and human-induced, and to the main transport pathway due to the general atmospheric circulation. As observed by Chahine et al. (2008), in the Northern Hemisphere the tropospheric jet stream plays a fundamental role in shaping the CO_2 concentration pattern at the mid-latitudes. Even if with smaller amplitude a similar feature may be found also in the Southern Hemisphere: the characteristics of the average austral atmospheric circulation leads to a mid-latitude concentration belt much more zonally uniform than the North Hemisphere case. Moreover, the role of the carbon dioxide emissions due to anthropogenic activities in enhancing the observed inter-hemispheric gradient, especially on the annual to interannual time scale, has been tested and confirmed by modeling studies (*e.g.* Pearman et al., 1983).

CO_2 atmospheric concentration exhibits both spatial and temporal variability on a number of scale. This variability is driven by both natural and human-induced forcing

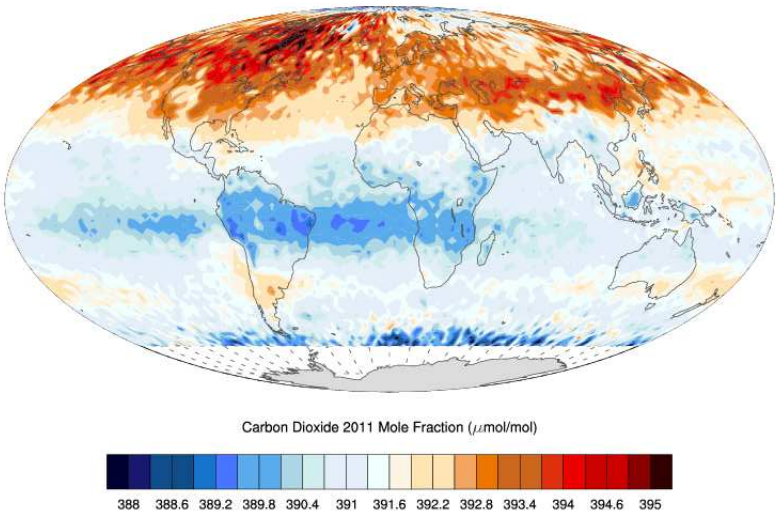

Figure 4.1: *Mean concentration of carbon dioxide for the year 2011 from satellite measurements.* (data from: `http://mirador.gsfc.nasa.gov/`)

and it has been widely observed from *in situ* (*e.g.* Linter, 2002) and satellite data (*e.g.* Jiang et al., 2010) and analysed in a model framework (*e.g.* Tans et al., 1990; Gurney et al., 2002). The seasonal signal is mainly related to the biosphere activity (*i.e.* carbon uptake through photosynthesis, and carbon release through autotrophic and heterotrophic respiration), which shapes the CO_2 spatial distribution on both the global and regional scale (Fung et al., 1983). On the other hand, on the interannual time scale different factors contribute in a complex way to define the actual distribution and growth rate of atmospheric carbon dioxide. Indeed, the relative importance of the variability in the natural and anthropogenic land surface sources and sinks, in the ocean-driven fluxes, and in the atmospheric circulation is a widely discussed topic in the literature (*e.g.* Nevison et al., 2008). Studying the mechanisms which regulate the spatial variability in atmospheric carbon dioxide concentration is beyond the goal of this work and here will not be considered.

In this framework, we change the point of view: the starting point is the observation that some carbon sources - as the ones due to human activities - are generally localised in space and do not show a strong temporal variability, leading to some stationarity also in the spatial distribution of the atmospheric content of CO_2. Our aim is to assess if it is possible to identify an atmospheric signal related to a stationary and localized carbon dioxide forcing. In other words, the questions we want to address are: is the *persistence* of an anomalous *localised* CO_2 concentration in the atmosphere effective on atmospheric variability? And in this case, what is the related signature? In order to investigate this issue, we have performed a set of experiments where a *stationary* and spatially *localised* pulse of carbon dioxide concentration is introduced in the system. Considering three different forcing regions has allowed us to test the sensitivity of the atmosphere to the location of the anomalous carbon dioxide distribution. Moreover, it is important to stress that these

experiments have been performed in a totally idealized framework, which has helped us to excite and identify a pattern which we have interpreted as related with a localized and stationary CO_2 forcing. In the next section the experimental design is presented, while in sections (4.2) and (4.3) the results from the three experiments will be analysed and discussed.

4.1 Rational of the experiment and experimental design

In our attempt to detect the atmospheric signature due to a localized CO_2 forcing, a set of idealized experiments have been performed. We have used the same numerical tool exploited in the first part of this work. In Chapter Two a more detailed description of the numerical model can be found, thus in this section we will just recall the main features of the model structure and will define the new experimental design exploited in this framework.

The main focus is the response of the atmosphere, therefore the CESM has been set in a slab ocean configuration. A fully active atmosphere, together with a full sea ice and land surface components are coupled to a simplified one-layer ocean. This model setup guarantees realistic energy fluxes between the atmosphere and the other model components, with a much less expensive computational demand.

To study the effects of a localized carbon dioxide perturbation we introduce a stationary anomalous "spot" of CO_2 over different regions, while all the other forcings are kept constant. The anomalous forcing is switched on and then kept constant for ten years of simulation. Three different experiments have been performed, with the anomalous CO_2 perturbation concentrated over different regions. To test the sensitivity of the system to the location of the forcing the regions which have been selected are the Equatorial Pacific, the South East Asia, and the North America continent. For the sake of simplicity, the three experiments will be identified respectively as the "Pacific", "Far East Asia", and "North America" experiment.

The anomalous CO_2 perturbation has been analytically defined as a 2-D Gaussian function:

$$C(x,\, y) = \mathcal{C}_{2000} \exp\left[-\frac{(x - x_0)}{2\,\Delta x^2}\right] \exp\left[-\frac{(y - y_0)}{2\,\Delta y^2}\right] \tag{4.1}$$

where x_0 and y_0 are respectively the longitude and latitude value which identify the center of the carbon dioxide spot, while $\Delta\, x$ and $\Delta\, y$ define the typical zonal and meridional dimension of this spot, *i.e.* 20 degrees in longitude, and 8 degrees in latitude. $\mathcal{C}_{2000}$ represents the reference value ($\sim$ 369 ppm) from which the CO_2 concentration smoothly increase. Just to clarify which the structure of the forcing, in figure (4.2a)-(4.2c) the

anomalous CO_2 spot for the three cases is shown.

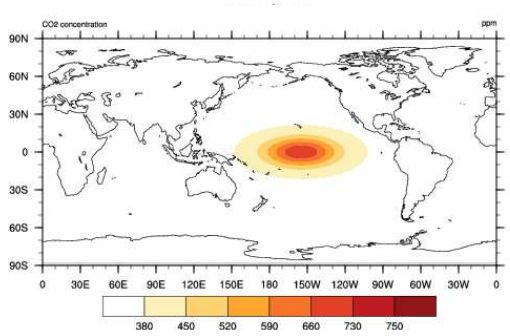

(a) CO_2 *forcing over Equatorial Pacific (latitude of maximum forcing:* 0N*)*

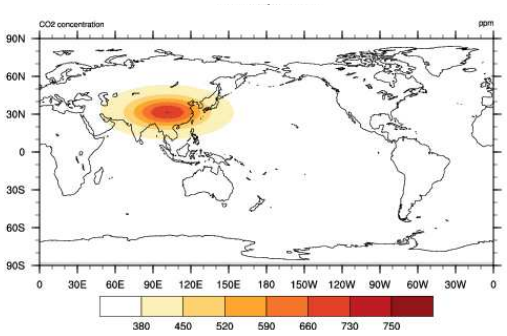

(b) CO_2 *forcing over South-East Asia (latitude of maximum forcing:* 31N*)*

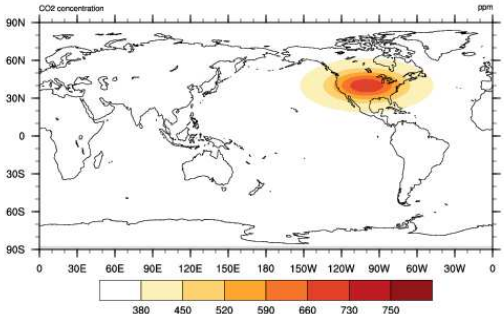

(c) CO_2 *forcing over North America (latitude of maximum forcing:* 40N*)*

Figure 4.2: *Stationary and localized* CO_2 *forcing for the three experiments. Values ranging from* 360 *to* 750 ppm.

The anomaly is elongated in the zonal direction and the maximum value, at the center of the spot, is twice as large as the reference one. No vertical structure has been defined, so the same anomalous concentration of CO_2 has been imposed at each discrete vertical level of the air column.

To detect the signature in the atmospheric fields due to the localised forcing, an *ensemble* approach has been exploited: for each experiment six different simulations, lasting ten year each, have been performed. The only difference between the six members of the ensemble is the initial condition: starting from the control experiment described in section (2.2.2), six different, but statistically and physically equivalent, realizations of the reference state of the system have been selected, and from each of them a ten-year forced simulation has been carried on. As shown in the next section, given that the focus is the stationary response of the atmosphere and that no temporal variability is accounted for in the applied forcing, we have adopted a very simple but straightforward metrics to identify the response of the system: the ten-year ensemble mean difference between the forced and the control simulations. The rational underlying this choice is the assumption that the output of a

model experiment consists of the superposition of the signal due to the applied boundary conditions (*e.g.* the present day uniform greenhouse gas concentration for the unforced simulation, and the localized doubling pulse of CO_2 for the forced experiment) and the noise due to the internal variability of the system. With the ensemble mean the internal variability noise is reduced, and hence the difference between the forced and the unforced averages allows us to extrapolate a signal which can be interpreted as the signature related to the considered forcing.

To recap the structure of the experiment, from the control simulation described in section (2.2.2) - which simulates recursively the present day condition -, six different initial conditions have been chosen, and from them, both a forced and an unforced simulations have been branched off. Each numerical exercise lasts ten years, for a total of 60 years of forced and control simulations. With this setup three different experiments have been carried on, with the anomalous concentration of CO_2 switched on over different regions. As discussed in the next section, the model turns out to be sensitive to the applied forcing, and a statistically significant pattern will be detected in all the three cases.

4.2 Atmospheric response to a localized forcing

Before analysing the atmospheric signature due to the applied forcing, we have performed a sanity check on our model design. We have tested the sensitivity of the model to the applied forcing, by looking at the radiative heating response locally in the forced region. We know that an increase in carbon dioxide concentration should warm the troposphere, due to the re-emission of longwave radiation from the Earth's surface, and cool the stratosphere, given that the increase emissivity of the upper layer of the atmosphere enhances the emitted radiation in the outer space.

As stressed in the previous section, the response due to the forcing in this stationary framework has been defined always in terms of ten-year ensemble mean difference between the forced and the control experiment. In figure (4.3) the heating rate signal due to the longwave component of the radiation for the Pacific experiment is reported. The longitude-height section is plotted at the latitude for which the forcing is maximum, in this case at the Equator. We find exactly the behaviour we expect: on the top layer of the model there is a clear cooling (left panel), while in the mid troposphere (right panel) a positive signal, typical of an enhanced warming can be found. If we look at the temperature profile at the same latitude (figure (4.4)), we find a consistent anomaly. A similar pattern may be found also for the Far East Asia and for the North America experiments (not shown).

Once we have checked that the local effect of the carbon dioxide anomaly is consistent with what we expect, we may look at the global signature of the applied forcing. For every field analysed a *t-test* has been performed, in order to check for the statistical significance

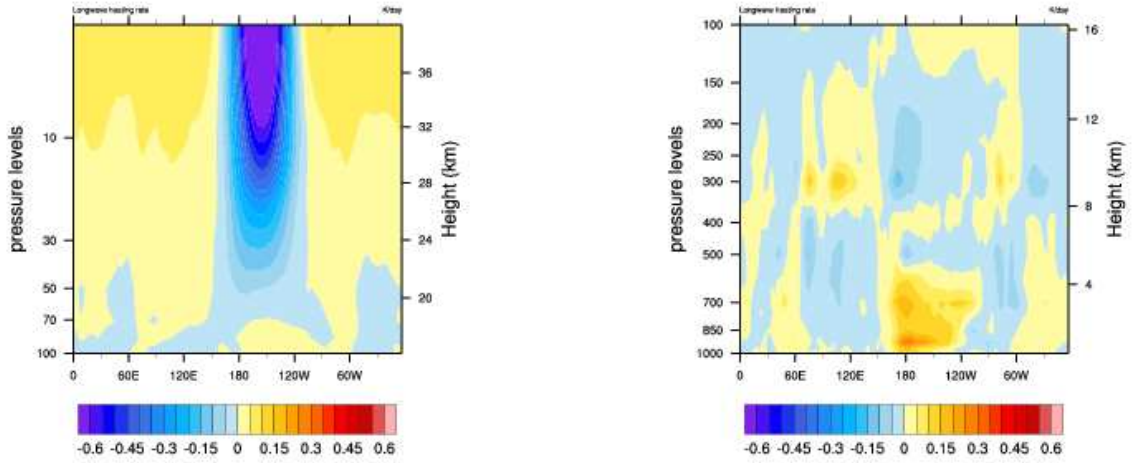

Figure 4.3: *Longwave heating rate profile* (Pacific Case)*: forced minus control experiment - 10-year ensemble mean. Longitude-vertical section at the latitude* (0N) *of maximum* CO_2 *anomaly.*
Left panel: *Stratospheric signal.* Right panel: *Tropospheric signal.*
Values ranging from $-0.6\,\mathrm{Kday}^{-1}$ *to* $0.6\,\mathrm{Kday}^{-1}$

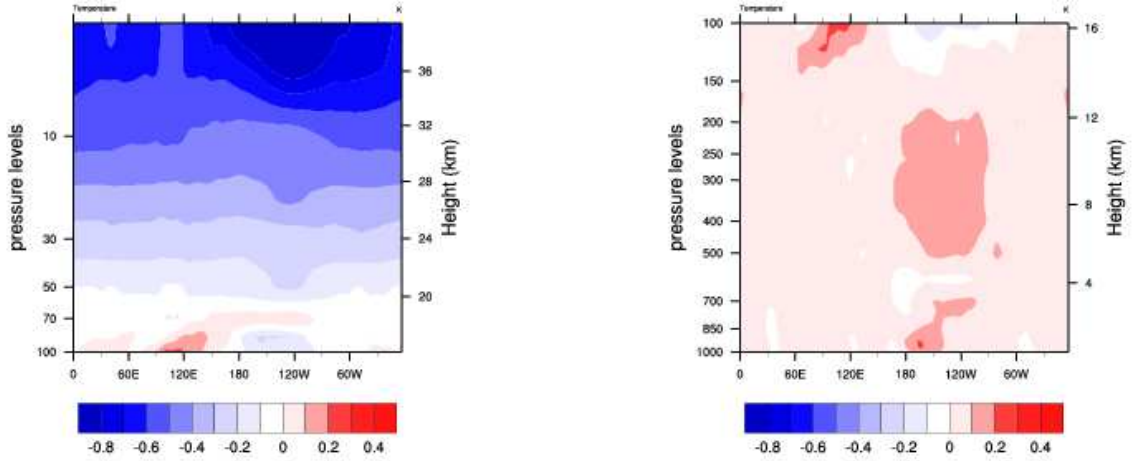

Figure 4.4: *Temperature profile* (Pacific Case)*: forced minus control experiment - 10-year ensemble mean. Longitude-vertical section at the latitude* (0N) *of maximum* CO_2 *anomaly.*
Left panel: *Stratospheric signal.* Right panel: *Tropospheric signal.*
Values ranging from $-0.4\,\mathrm{K}$ *to* $0.4\,\mathrm{K}$

of the results. The confidence level has been set at 95 %.

4.2.1 Pacific Experiment

In figure (4.5a) the 300 hPa geopotential height signal for the Pacific experiment is shown. The prominent response at the large scale is a wave-like pattern which is mainly concentrated over the North-East Pacific, the North America continent and the North Atlantic region. The regions where the signal is stronger are statistically significant, making us confident that this pattern is actually related to the forcing.

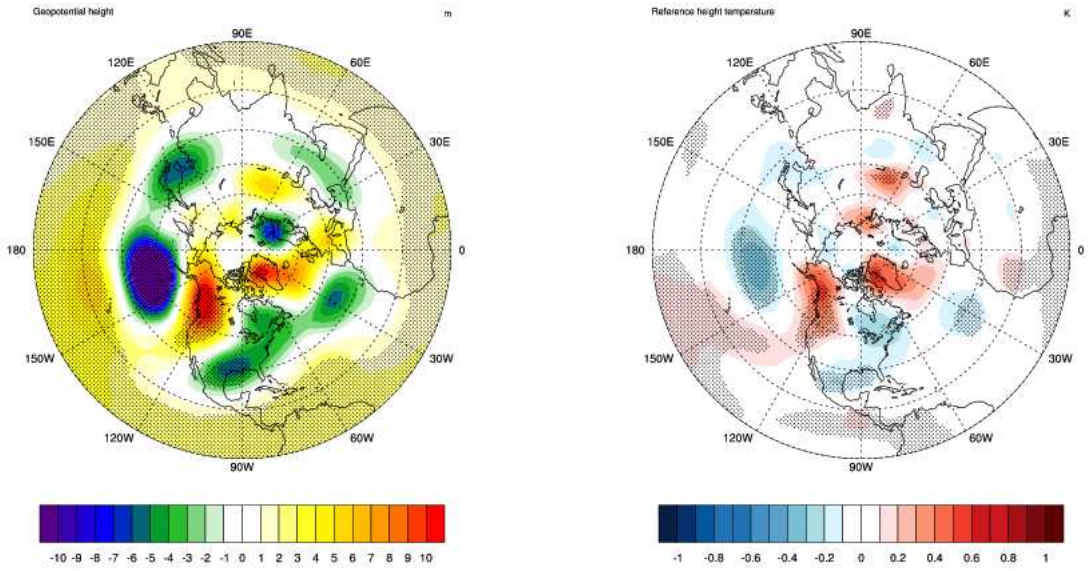

(a) 300 hPa *Geopotential Height* (Pacific Case)

(b) *Near Surface* (2m) *Temperature* (Pacific Case)

Figure 4.5: *Forced minus control experiment - 10-year ensemble mean fields for the Pacific case. The shaded area represents the region in which the results are statistically significant at* 95% *of confidence level. In panel* (a) *the values range from* −10 m *to* 10 m. *In panel* (b) *the values range from* −1 K *to* 1 K.

This signal resembles the PNA - *Pacific North America Pattern* (Wallace and Gutzler, 1981). The PNA is a prominent feature of the atmospheric variability over the Northern Hemisphere extratropical region, in particular during the winter season. It is characterized by a positive phase, with high pressure anomaly over the western North American continent and a low pressure anomaly over the North-East Pacific, roughly over the Aleutian Islands, and over the South-East North America continent, while during the negative phase this pattern is reversed. The positive phase of the PNA has been seen to correlate with the positive ENSO phase (*e.g.* Trenberth et al., 1998): the ENSO-related warm sea surface temperature and the enhanced precipitation over the central Equatorial Pacific induce an anomalous tropospheric heating, which, as may be explained through a basic linear theory

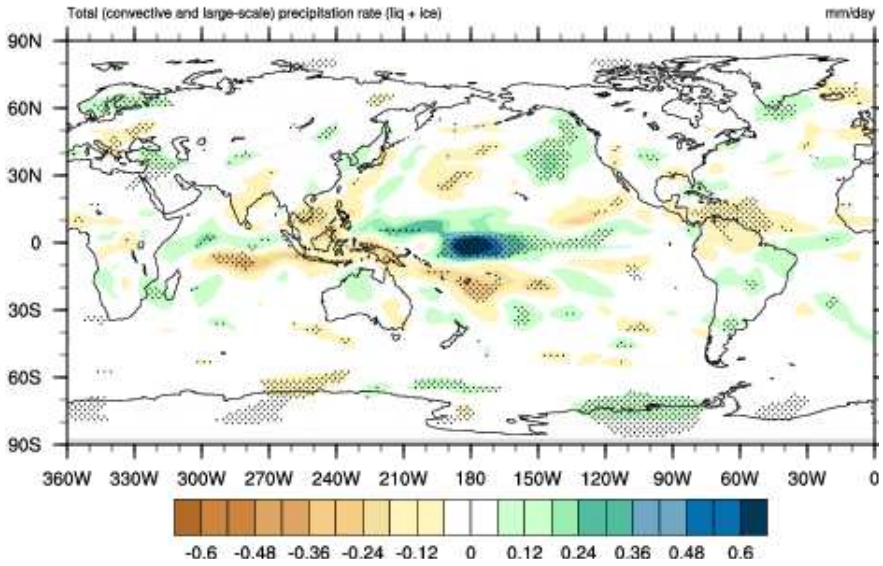

Figure 4.6: *Total precipitation* (Pacific Case)*: forced minus control experiment - 10-year ensemble mean. The shaded area represents the region in which the results are statistically significant at* 95% *of confidence level. Values ranging from* $-0.6\,\mathrm{mmday}^{-1}$ *to* $0.6\,\mathrm{mmday}^{-1}$.

(*e.g.* Hoskins and Karoly, 1981), can behave as a source for a stationary Rossby wave train propagating eastward and poleward. The validity of this simple linear framework has been widely discussed in the literature, and a overall appraisal can be found in the review by Liu (2007).

The local effect of the anomalous carbon dioxide spot in terms of mid troposphere heating forcing (figure (4.4)) may lead us to interpret this geopotential height signal as due to the dynamical response of the system to a localised tropical heating: a stationary Rossby wave train forced in the tropical region which propagates following, to a first approximation, a great circle route.

The response in terms of surface temperature (figure (4.5b)) is consistent with the geopotential height pattern: the region with a high pressure anomaly are warmer at the surface, and *viceversa* in correspondence with the low pressure areas, there is a negative temperature anomaly. Moreover, the warm signal across the equator between 180E and 150E may be considered as the local effect of the anomalous CO_2 concentration.

To complete our analysis, let us look at the precipitation anomaly (figure (4.6)). The main feature which can be noticed is a clear positive signal over the central-western tropical Pacific, and a negative anomaly in the Indian Ocean, to the west of the Indonesian archipelago. This signal may suggest an anomalous zonal circulation in the equatorial region, which indeed can be found by looking at the upper and lower level zonal velocity signal (figure (4.7a)-(4.7b)). The anomaly in the tropical western Pacific up to the Australian region changes sign - from positive to negative - with height. The picture is consistent with the vertical motion pattern: if we look at the longitude-vertical section of

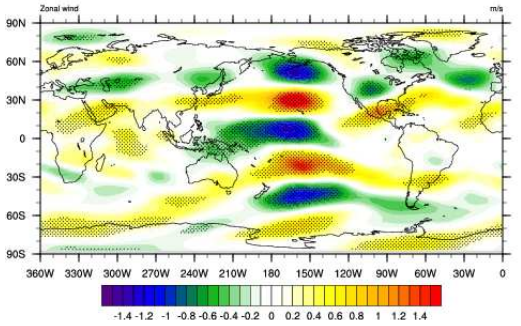

(a) 200 hPa *Zonal Wind*
(Pacific Case)

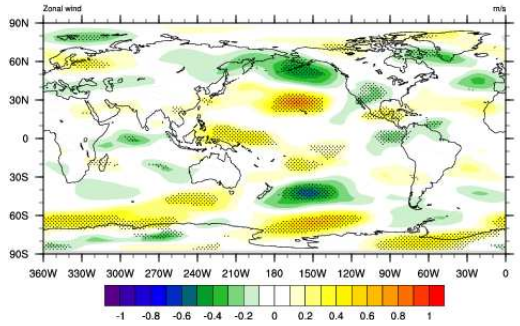

(b) 700 hPa *Zonal Wind*
(Pacific Case)

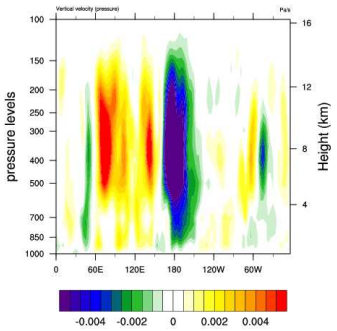

(c) *Vertical Pressure Velocity: longitude - vertical section at* 5S
(Pacific Case)

Figure 4.7: *Forced minus control experiment - 10-year ensemble mean fields for the Pacific case. The shaded area represents the region in which the results are statistically significant at* 95% *of confidence level (for the vertical section no shaded area has been plotted). In panel* (a) *the values range from* $-1.5\,\mathrm{ms}^{-1}$ *to* $1.5\,\mathrm{ms}^{-1}$*, in panel* (b) *the values range from* $-1\,\mathrm{ms}^{-1}$ *to* $1\,\mathrm{ms}^{-1}$*, and in panel* (c) *the values range from* $-5\times10^{-3}\,\mathrm{Pas}^{-1}$ *to* $5\times10^{-3}\,\mathrm{Pas}^{-1}$.

the vertical pressure velocity (figure (4.7c)) we notice a negative anomaly (*i.e.* ascending motion) at 180E, in correspondence to the positive precipitation spot, and a positive signal (*i.e.* descending motion) between 60E and 90E, where there is the negative anomaly in the precipitation.

4.2.2 Far East Asia Experiment

Following the same philosophy of the previous case, let us start from the 300 hPa geopotential height signal (figure (4.8a)). Also in this case we find a statistically significant pattern, whose shape is somehow unexpected. Even if the amplitude and the exact position of the maxima and minima are different from the ones seen in the previous case, a similar wave-like pattern, mainly concentrated over the North America region, can be found. In particular, also in this case, we can find distinct maxima over the North-West North

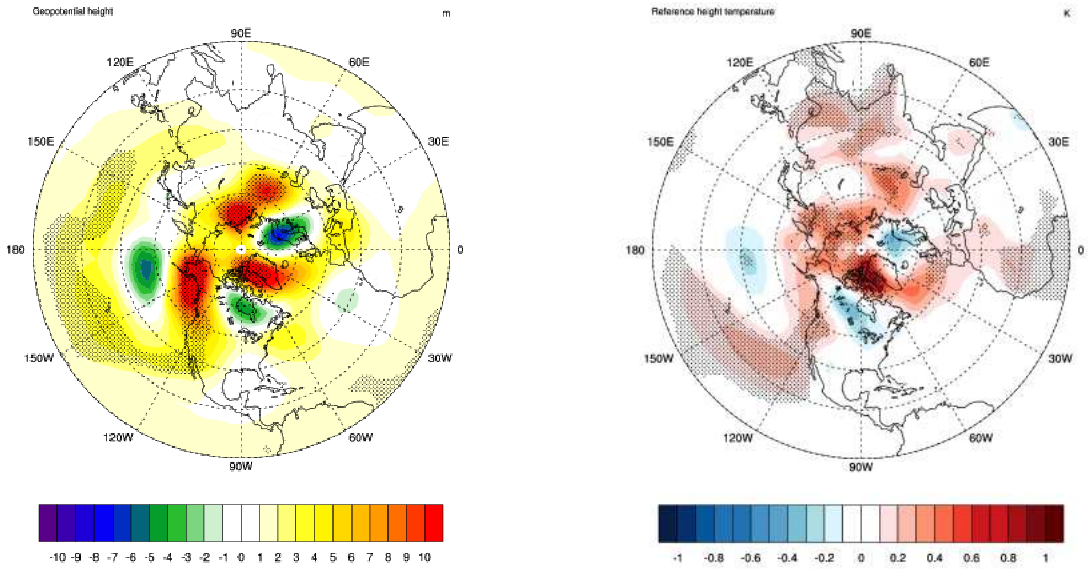

(a) 300 hPa *Geopotential Height* (Far East Asia Case)

(b) *Near Surface* (2m) *Temperature* (Far East Asia Case)

Figure 4.8: *Forced minus control experiment - 10-year ensemble mean fields for the Far East Asia case. The shaded area represents the region in which the results are statistically significant at* 95% *of confidence level. In panel* (a) *the values range from* $-10\,\mathrm{m}$ *to* $10\,\mathrm{m}$. *In panel* (b) *the values range from* $-1\,\mathrm{K}$ *to* $1\,\mathrm{K}$.

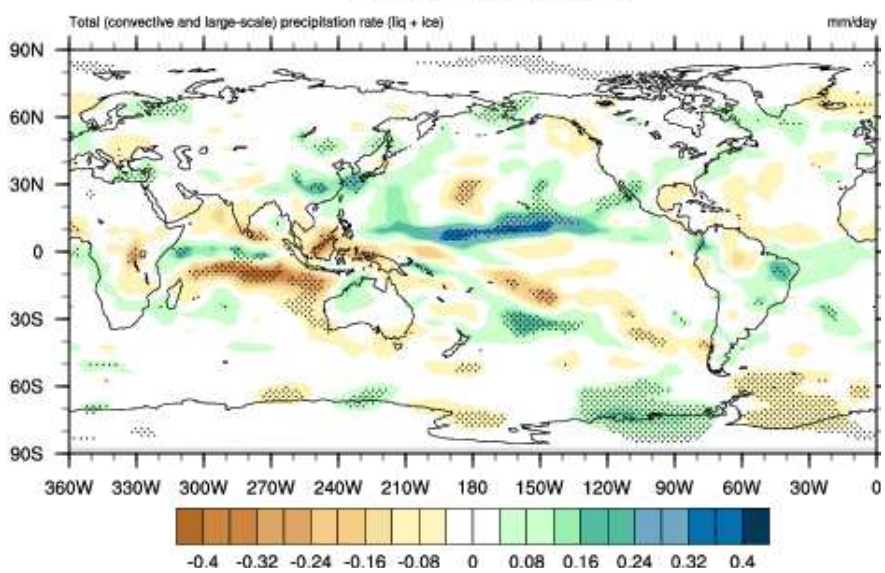

Figure 4.9: *Total precipitation* (Far East Asia Case)*: forced minus control experiment - 10-year ensemble mean. The shaded area represents the region in which the results are statistically significant at* 95% *of confidence level. Values ranging from* $-0.4\,\mathrm{mmday}^{-1}$ *to* $0.4\,\mathrm{mmday}^{-1}$.

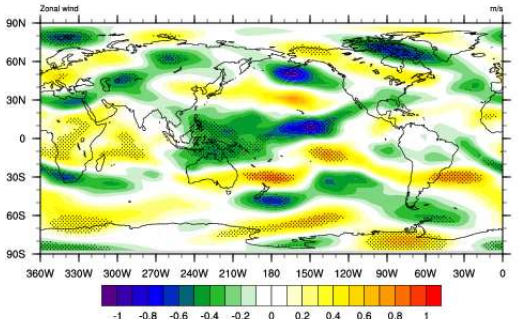

(a) 200 hPa *Zonal Wind*
(Far East Asia Case)

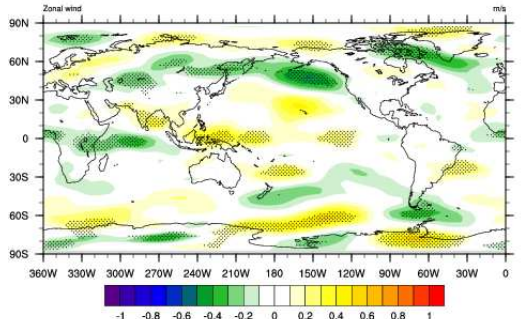

(b) 700 hPa *Zonal Wind*
(Far East Asia Case)

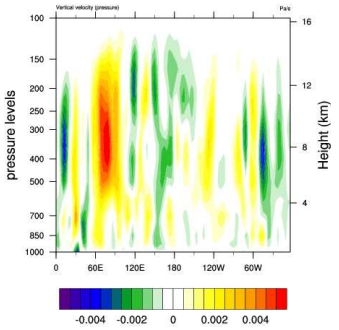

(c) *Vertical Pressure Velocity: longitude - vertical section at* 5S
(Far East Asia Case)

Figure 4.10: *Forced minus control experiment - 10-year ensemble mean fields for the Far East Asia case. The shaded area represents the region in which the results are statistically significant at 95 % of confidence level (for the vertical section no shaded area has been plotted). In panel* (a) *and in panel* (b) *the values range from* $-1\,\mathrm{ms}^{-1}$ *to* $1\,\mathrm{ms}^{-1}$. *In panel* (c) *the values range from* $-5 \times 10^{-3}\,\mathrm{Pas}^{-1}$ *to* $5 \times 10^{-3}\,\mathrm{Pas}^{-1}$.

America continent and over Greenland, while the minimum over the North-East Pacific is reduced in amplitude and appears not to be as significant, from a statistical point of view, as in the previous case. With an analogous amplitude the wave structure is extended across the mid-to-high latitude sector over Eurasia. The surface temperature (figure (4.8b)), shows a pattern consistent with the geopotential fingerprint, together with a warming signal over South East Asia, which we interpret as due to the local effect of the CO_2 forcing.

If we look at the precipitation anomalies (figure (4.9)), also in this case the positive/negative dipole across the Indonesian archipelago can be found, even if with a lower amplitude, especially in the Pacific area, and more elongated in the zonal direction. Even if also in this case the anomaly is less intense than in the Pacific experiment, the eastward anomalous low level zonal wind in the western Pacific (figure (4.10b)) turns to a westward anomaly going in the upper troposphere (figure (4.10a)). As shown in figure (4.10c), the vertical velocity signal is totally consistent.

4.2.3 North America Experiment

Also in this case, the 300 hPa geopotential height shows a statistically significant wave-like pattern. As can be seen in figure (4.11a), this signal strongly recalls the one described for the Far East Asia experiment, with a stronger maximum over the western North America continent, and a less pronounced expansion of the signal eastward. The minima are located over the same area described in the previous case, but their amplitude is generally smaller.

Consistently, the shape of the surface temperature (figure (4.11b)) exhibits a more intense warming over west to central North America, which presumably is due to the combination of the local effect due to the forcing, and to the enhanced large scale signal. A strong positive signal can be found also over Greenland.

If finally we analyse the precipitation pattern (figure (4.12)), we notice that the dipole westward to the dateline appears reversed and shifted northward in comparison with the previous cases: there is an anomalous precipitation over Southern India, and a negative anomaly over the Philippines.

Even though, generally speaking, the signal is more concentrated at the mid-latitudes, nevertheless a negative low level zonal velocity anomaly can be found across Indonesia and the Thailand Peninsula, which changes sign with height. Both the low and the upper level anomaly are less elongated zonally than the previous case, and consistently the distance between descending and the ascending region is reduced (figure(4.13)).

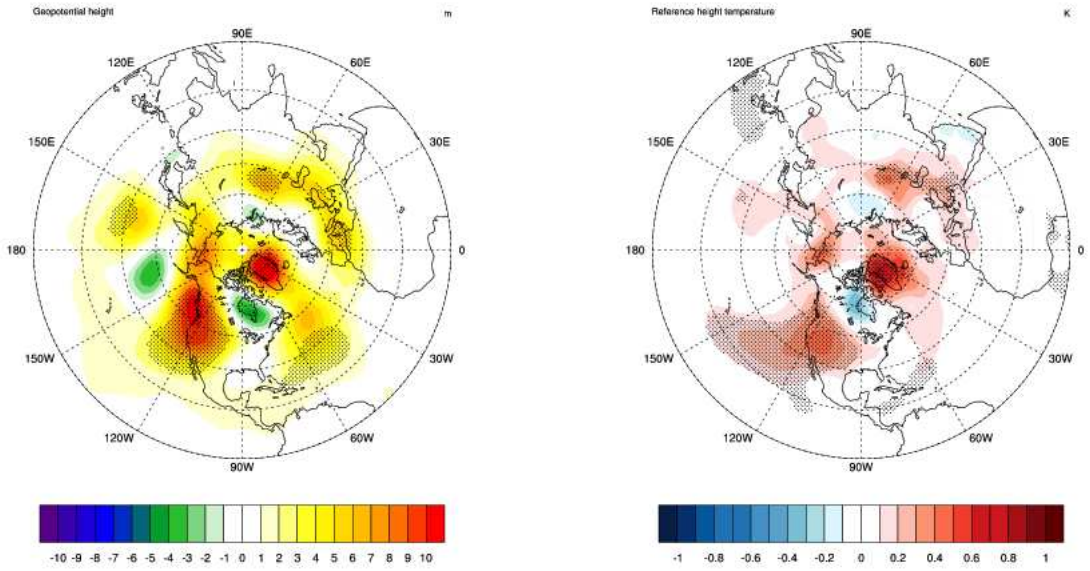

(a) 300 hPa*Geopotential Height* (North America Case)

(b) *Near Surface (2m) Temperature* (North America Case)

Figure 4.11: *Forced minus control experiment - 10-year ensemble mean fields for the North America case. The shaded area represents the region in which the results are statistically significant at* 95% *of confidence level. In panel* (a) *the values range from* $-10\,\mathrm{m}$ *to* $10\,\mathrm{m}$. *In panel* (b) *the values range from* $-1\,\mathrm{K}$ *to* $1\,\mathrm{K}$.

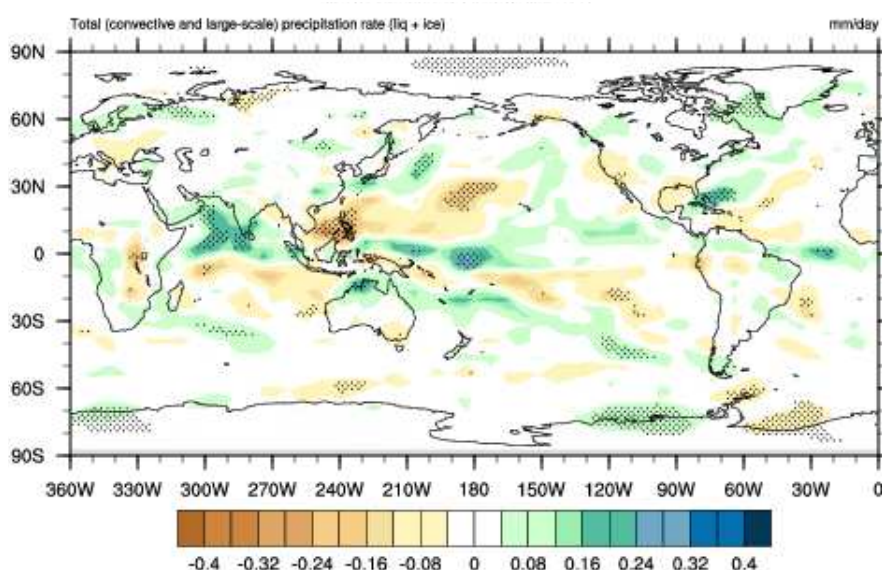

Figure 4.12: *Total precipitation* (North America Case)*: forced minus control experiment - 10-year ensemble mean. The shaded area represents the region in which the results are statistically significant at* 95% *of confidence level. Values ranging from* $-0.4\,\mathrm{mmday}^{-1}$ *to* $0.4\,\mathrm{mmday}^{-1}$

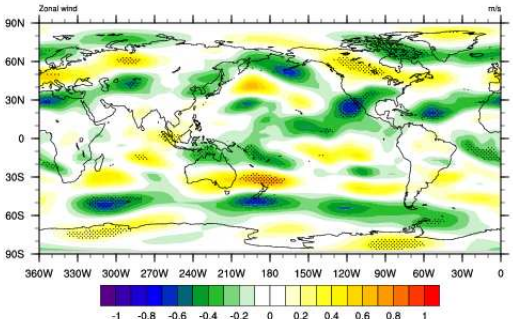

(a) 200 hPa *Zonal Wind*
(North America Case)

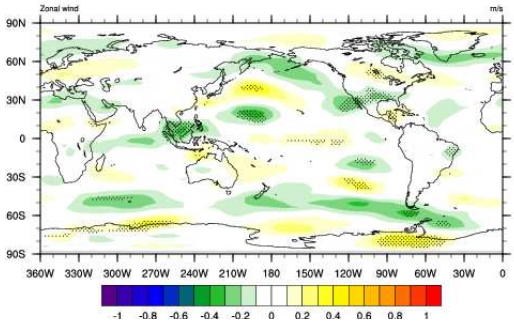

(b) 700 hPa *Zonal Wind*
(North America Case)

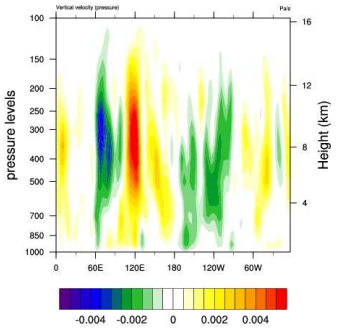

(c) *Vertical Pressure Velocity: longitude - vertical section at* 10N
(North America Case)

Figure 4.13: *Forced minus control experiment - 10-year ensemble mean fields for the North America case. The shaded area represents the region in which the results are statistically significant at* 95% *of confidence level (for the vertical section no shaded area has been plotted). In panel* (a) *and in panel* (b) *the values range from* $-1\,\mathrm{ms}^{-1}$ *to* $1\,\mathrm{ms}^{-1}$. *In panel* (c) *the values range from* $-5 \times 10^{-3}\,\mathrm{Pas}^{-1}$ *to* $5 \times 10^{-3}\,\mathrm{Pas}^{-1}$.

4.3 Summary and discussion of the experimental results

To study the possible effects on the atmospheric large scale variability due to a persistent and localised CO_2 concentration anomaly, we have performed a set of idealized experiments. We have placed the forcing over different regions, in order to test the sensitivity of the model to the position of the forcing. South East Asia and North America are indeed areas characterized by a remarkable CO_2 emission levels, while the Pacific experiment may be thought of as a "benchmark" experiment: the interaction between low latitude sea surface temperature anomaly (and the related warming in the troposphere), and mid-latitude circulation and the related mechanisms, has been for a long time discussed in the literature, and still is.

The first notable result is that the model is indeed sensitive to the applied forcing. The response pattern is statistically significant for all the experiments we have performed, and in all the different fields we have looked at. In terms of large scale circulation, regardless of the location of the forcing, we have excited a signal which strongly resembles the Pacific North America pattern. In the literature different mechanisms have been referred to in order to interpret the occurrence of the PNA in the observed natural low frequency variability of the atmosphere. Simmons and colleagues (Simmons et al., 1983), in their model experiments, consider the effects of a set of localized forcings over different regions of the global domain. Independently of the position of the forcing, the atmospheric response is characterized by a recurrent PNA-like pattern, which they interpret as the consequence of a dynamical instability process internal to the atmosphere. In their analysis, even if the PNA response was obtained for both tropical and mid-latitude sources, they find some preferred forcing regions which may trigger the instability mode over the North Pacific area: the South East Asia and the North West tropical Pacific.

The fact that we have obtained similar patterns for all the three experiments, may suggest that we are indeed looking at an internal mode of variability of the atmosphere, excited by the CO_2-induced localized heating. The different amplitude and the different locations of the maxima and minima may be explained in terms of "efficiency" of the forcing position in exciting the internal mode.

Another interesting feature is the signal we have obtained in terms of tropical convection. A dipole structure similar to the one described above, has been studied in the literature (*e.g.* Franzke et al., 2011), and has been linked to the evolution of the observed PNA life cycle over different time scales (*e.g.* Johnson and Feldstein, 2010). In our case it is important to stress that we are looking at stationary patterns, so by definition the time causality relation cannot be detected. An attempt to interpret the change in sign in the dipole convective pattern noted in the North America experiment, may be made by

looking at the shift of the high pressure center over the western North America continent towards the Aleutian Islands, and the enhanced high pressure along the North American Eastern coast. These changes, with respect to a fully established positive-like PNA pattern (as the one obtained for the Pacific Experiment), may be suggestive of the inception of a negative PNA phase, related tropical convective pattern of which is similar to the one in figure (4.12).

Chapter 5

A Linear Model

In Chapter Four the atmospheric response due to a localized CO_2 forcing has been investigated, and a statistically significant signal has been detected. We want to go a step further, and give a direct assessment on the dynamical fingerprint related to the forcing we have applied. For this reason we have decided to study the dynamical linear response of the system to the global heating distribution associated with the anomalous carbon dioxide distributions discussed in the previous chapter. Coherently with the analysis performed before, we have focused on the stationary linear response.

A linear models is a powerful tool to understand the basic mechanisms ruling the large scale dynamics of the atmosphere. Although the atmosphere is characterized by a strong non-linear behaviour, the linear response to a given forcing represents the fundamental dynamical response of the system. For example, the stationary wave propagation due to an asymmetric forcing has been widely investigated in a linear framework. The underlying idea is that preferred locations of diabatic heating sources in the troposphere and the orographic features at the surface may shape the long term mean state of the atmospheric flow, and thus partially explain the low frequency climatological signal. In the literature linear model of increasing complexity have been adopted. Two-dimensional barotropic models solve the vorticity equation, including the forcing in terms of an anomalous divergence term, and considering some analytical or climatological basic state (*e.g.* Branstator, 1985; Hoskins and Ambrizzi, 1993). The choice of the level at which such a formalization may be representative of the features of the real atmosphere has been discussed from both a theoretical (Held et al., 1985) and a numerical (Ting, 1996) point of view. On the other hand, multi-level baroclinic models solve the full set of linearized primitive equations: the numerical complexity of the problem increases considerably, especially when a zonally asymmetric basic state is considered, but at the same time a much deeper analysis of the linear signal is allowed. Together with the analysis of the effects of a three-dimensional localized forcing (*e.g.* Hoskins and Karoly, 1981; Navarra, 1990; Ting and Sardeshmukh, 1993; Ting and Yu, 1998), the possibility to match the numerical structure of a full general

circulation model with a much simpler numerical tool, as the linear model, enhances the investigation of the stationary long term climatology and low frequency variability of the simulated atmosphere (*e.g.* Nigam et al., 1986; Branstator, 1990).

In our framework, in order to have a significant analysis, we need a linear model which shares the same numerical scheme and resolution of the full version of CAM exploited in the original simulations. Starting from the full non-linear version of the actual Eulerian Dynamical Core implemented in CAM, a new linearization has been proposed: the dynamical equations in the hybrid vertical coordinate system have been analytically linearized, and to solve numerically the steady state problem the strategy proposed by Hoskins and Karoly (1981) has been adopted. In the literature, a previous linearized version of CAM may be found (Branstator, 1990), however in that case the reference non-linear model was the CCM0B model (Williamson, 1983), which was formulated in terms of σ vertical coordinates. Hence, even if the general philosophy followed for the linearization procedure is the same, the analytical and numerical outcome strongly depends on the choice of the vertical coordinates, making our linear model totally independent of the previous formulation.

In section (5.1)-(5.2), the analytical and numerical approaches exploited in this work are described, while some preliminary tests on the model are presented in section (5.3).

5.1 Linearization of CAM Eulerian Dynamical Core

The equations describing the motion of a layer of finite thickness of fluid on a sphere are by definition non-linear. As already discussed in section (2.1), several equivalent choices may be done regarding the variables, and consequently the equations, which describe the system state and evolution. In this case our benchmark is the set of equations solved in the Eulerian Dynamical Core of CAM: the prognostic variables are vorticity (ζ), divergence (D), temperature (T), and logarithm of the surface pressure (q). Together with these, also the equations for the diagnostic variables (the geopotential Φ, the pressure vertical velocity ω, and the vertical velocity for advection $\dot{\eta}\frac{\partial p}{\partial \eta}$) are needed. As reported in Neale et al. (2010), the equations solved by the model are:

$$\frac{\partial \zeta}{\partial t} = \hat{k} \cdot \nabla \times \left(\frac{\hat{n}}{\cos\phi} \right) \tag{5.1a}$$

$$\frac{\partial D}{\partial t} = \nabla \cdot \left(\frac{\hat{n}}{\cos\phi} \right) - \nabla^2 \left(E + \Phi \right) \tag{5.1b}$$

$$\frac{\partial T}{\partial t} = -\frac{1}{a \cos^2\phi} \left[\frac{\partial \left(UT \right)}{\partial \lambda} + \cos\phi \frac{\partial \left(VT \right)}{\partial \phi} \right] + TD - \dot{\eta} \frac{\partial p}{\partial \eta} \frac{\partial T}{\partial p} + \frac{R}{c_p} T \frac{\omega}{p} + Q \tag{5.1c}$$

$$\frac{\partial q}{\partial t} = -\int_{(\eta_t)}^{(1)} \mathbf{V} \cdot \nabla q \, d\Big(\frac{\partial p}{\partial \pi} \Big) - \frac{1}{\pi} \int_{p(\eta_t)}^{p(\eta_1)} D \, dp \tag{5.1d}$$

where Q is the applied heating, R is the gas constant, c_p is the specific heat capacity at constant pressure, and π is the surface pressure. Moreover, the following relations hold:

$$\begin{aligned}
\hat{n} &= (n_U,\, n_V) \\
n_U &= (\zeta + f)V - \dot{\eta}\frac{\partial p}{\partial \eta}\frac{\partial U}{\partial p} - \frac{RT}{a}\frac{\pi}{p}\frac{\partial p}{\partial \pi}\frac{\partial q}{\partial \lambda} + F_u \\
n_V &= -(\zeta + f)U - \dot{\eta}\frac{\partial p}{\partial \eta}\frac{\partial V}{\partial p} - \frac{RT\cos\phi}{a}\frac{\pi}{p}\frac{\partial p}{\partial \pi}\frac{\partial q}{\partial \phi} + F_v \\
\mathbf{V} &= (U, V) = (u, v)\cos\phi \\
E &= \frac{U^2 + V^2}{2\cos^2\phi}
\end{aligned}$$

where F_u and F_v are the forcing terms in the momentum equations.

To close the system three diagnostic equations are needed:

$$\Phi = \Phi_s + R\int_{p(\eta)}^{p(1)} T\, d\ln\, p \tag{5.2a}$$

$$\begin{aligned}
\dot{\eta}\frac{\partial p}{\partial \eta} = \frac{\partial p}{\partial \pi}\left[\int_{(\eta_t)}^{(1)} \mathbf{V}\cdot\nabla\pi d\left(\frac{\partial p}{\partial \pi}\right) + \int_{p(\eta_t)}^{p(1)} D\, dp\right] - \\
- \int_{(\eta_t)}^{(\eta)} \mathbf{V}\cdot\nabla\pi d\left(\frac{\partial p}{\partial \pi}\right) - \int_{p(\eta_t)}^{p(\eta)} D\, dp
\end{aligned} \tag{5.2b}$$

$$\omega = \frac{\partial p}{\partial \pi}\mathbf{V}\cdot\nabla\pi - \int_{(\eta_t)}^{(\eta)} \mathbf{V}\nabla\pi d\left(\frac{\partial p}{\partial \pi}\right) - \int_{p(\eta_t)}^{p(\eta)} D\, dp \tag{5.2c}$$

The boundary conditions applied at the top and at the bottom of the domain are given by:

$$\dot{\eta}\frac{\partial p}{\partial \eta}\Big|_{\text{top}} = \dot{\eta}\frac{\partial p}{\partial \eta}\Big|_{\text{bottom}} = 0$$

As described in section (2.2), the variables are discretized on the vertical dimension following a hybrid coordinate system: the terrain-following layers relax toward flat pure pressure levels going to the top of the air column. Each level η_k is implicitly defined as that level the pressure of which $p(\eta_k)$ at each time step is equal to:

$$p(\eta_k) = A_k p_0 + B_k \pi \qquad k = 1, 2, \ldots, n_{lev} \tag{5.3}$$

where p_0 is a fixed reference pressure value, π is the actual surface pressure, A_k and B_k are a set of constants which, once the number of level is defined, regulate the transition between the pure pressure and the terrain-following regime. As discussed in Neale et al. (2010), this choice of the vertical coordinates system yields primitive equations of the form (5.1)-(5.2), and should be kept in mind to determine the terms involving p and $\frac{\partial p}{\partial \pi}$.

Given these preliminary considerations, let us describe the linearization strategy which has been adopted. The basic idea is to represent the state of the system as the sum of

a steady state basic state and a time-varying anomaly. If with ψ we denote a generic prognostic or diagnostic variable, this decomposition may be written as:

$$\psi(\lambda,\, \theta,\, \eta;\, t) = \overline{\psi}(\lambda,\, \theta,\, \eta) + \psi'(\lambda,\, \theta,\, \eta;\, t) \tag{5.4}$$

By introducing this decomposition, the equations for the basic state and for the anomaly can be defined, and, with appropriate assumptions, it will be immediate to obtain the linearized system.

Before going on with the explicit computation, let us put forward some observations about the treatment of the terms involving surface pressure π. When applying the linearization strategy the aim is to find equations which are linear, in the anomalies, with respect to the basic state. For our problem, the prognostic variable is not directly the surface pressure π, but q:

$$q = \ln(\pi)$$

If we apply (5.4) to q, we obtain:

$$\overline{q} + q' = \ln(\pi) \tag{5.5}$$

and hence:

$$\pi = \exp(\overline{q} + q') \tag{5.6}$$

If we want to write π as a linear function of the perturbation in the prognostic variable, we may consider the decomposition of the exponential function in terms of the harmonic series. By keeping only the first order term, we obtain:

$$\pi = \exp(\overline{q}) \exp(q') = \exp(\overline{q})(1 + q') \tag{5.7}$$

and thus we can denote:

$$\begin{aligned} \overline{\pi} &= \exp(\overline{q}) \\ \pi' &= q' \exp \overline{q} \end{aligned} \tag{5.8}$$

If we introduce the definition (5.7) for π into equation (5.3), which defines the pressure along the air column, by skipping the discrete indices and writing it in a continuous fashion we obtain:

$$p = Ap_0 + B\pi = Ap_0 + B \exp(\overline{q}) + Bq' \exp(\overline{q}) \tag{5.9}$$

In many cases we have terms which depend on $\frac{\partial p}{\partial \pi}$. By applying the chain rule we have:

$$\frac{\partial p}{\partial \pi(\overline{q},\, q')} = \frac{\partial p}{\partial \overline{q}} \frac{\partial \overline{q}}{\partial \pi} + \frac{\partial p}{\partial\, q'} \frac{\partial\, q'}{\partial \pi} \tag{5.10}$$

By re-writing equation (5.5) as:

$$q' = \ln(\pi) - \overline{q} \tag{5.11}$$

and given that:

$$\frac{\partial \overline{q}}{\partial \pi} = 0$$

equation (5.10) becomes:

$$\frac{\partial p}{\partial \pi} = \frac{\partial p}{\partial q'}\frac{\partial q'}{\partial \pi} = B\exp\left(\overline{q}\right)\left(\frac{1}{\exp(\overline{q})(1+q')}\right)$$

and therefore:

$$\frac{\partial p}{\partial \pi} = \left(\frac{B}{1+q'}\right) \tag{5.12}$$

Finally, under the reasonable assumption of small perturbation, we can exploit the approximation:

$$\frac{1}{1+q'} \sim 1 - q'$$

which yields:

$$\frac{\partial p}{\partial \pi} = B(1-q') \tag{5.13}$$

As before for π, also in this case we may denote:

$$\begin{aligned} \overline{\left(\frac{\partial p}{\partial \pi}\right)} &= B \\ \left(\frac{\partial p}{\partial \pi}\right)' &= -q'B \end{aligned} \tag{5.14}$$

We have now all the elements to perform the linearization. The complete derivation will be described for the case of the thermodynamic equation. For the other equations the procedure is completely analogous and just the final result will be reported.

The full non linear thermodynamic equation is:

$$\frac{\partial T}{\partial t} = -\frac{1}{a\cos^2\phi}\left[\frac{\partial\left(UT\right)}{\partial\lambda} + \cos\phi\frac{\partial\left(VT\right)}{\partial\phi}\right] + TD - \dot{\eta}\frac{\partial p}{\partial\eta}\frac{\partial T}{\partial p} + \frac{R}{c_p}T\frac{\omega}{p} + Q \tag{5.15}$$

By introducing the decomposition (5.4) into equation (5.15), we obtain:

$$\begin{aligned} \frac{\partial\left(\overline{T}+T'\right)}{\partial t} = -\frac{1}{a\cos^2\phi}\Bigg[&\frac{\partial}{\partial\lambda}\left(\left(\overline{T}+T'\right)\left(\overline{u}+u'\right)\cos\phi\right) \\ &+ \cos\phi\frac{\partial}{\partial\phi}\left(\left(\overline{T}+T'\right)\left(\overline{v}+v'\right)\cos\phi\right)\Bigg] + \\ &+ \left(\overline{T}+T'\right)\left(\overline{D}+D'\right) - \left(\overline{\dot{\eta}\frac{\partial p}{\partial\eta}} + \dot{\eta}\frac{\partial p'}{\partial\eta}\right)\frac{\partial}{\partial\overline{p}}\left(\overline{T}+T'\right) \\ &+ \frac{R}{c_p}\left(\overline{T}+T'\right)\left(\overline{\left(\frac{\omega}{p}\right)} + \left(\frac{\omega}{p}\right)'\right) \end{aligned} \tag{5.16}$$

Let us notice that, when there is a pressure-related term at the denominator (as for instance in the derivative $\frac{\partial}{\partial\left(\overline{p}+p'\right)}$), we can make the following approximation:

$$\frac{1}{\left(\overline{p}+p'\right)} = \frac{1}{\overline{p}\left(1+\frac{p'}{\overline{p}}\right)} \sim \frac{1}{\overline{p}}\left(1-\frac{p'}{\overline{p}}\right)$$

and given that $p' \ll \overline{p}$, we are justified in retaining just the basic state term:

$$\frac{1}{(\overline{p}+p')} \sim \frac{1}{\overline{p}}$$

If we compute the time average of equation (5.16), we will obtain the equation for the basic state. By definition the basic state is stationary, so we may write:

$$\begin{aligned} 0 = &- \frac{1}{a\cos^2\phi}\left[\frac{\partial}{\partial\lambda}\left(\overline{T}\,\overline{u}\cos\phi + \overline{T'u'\cos\phi}\right) + \cos\phi\frac{\partial}{\partial\phi}\left(\overline{T}\,\overline{v}\cos\phi + \overline{T'v'\cos\phi}\right)\right] + \\ &+ \overline{T}\,\overline{D} + \overline{T'D'} - \overline{\dot{\eta}\frac{\partial p}{\partial\eta}\frac{\partial T}{\partial\overline{p}}} - \overline{\dot{\eta}\frac{\partial p'}{\partial\eta}\frac{\partial T'}{\partial\overline{p}}} + \frac{R}{c_p}\overline{T}\overline{\left(\frac{\omega}{p}\right)} + \frac{R}{c_p}\overline{T'\left(\frac{\omega}{p}\right)'} \end{aligned} \tag{5.17}$$

If we subtract from the full state equation (5.16) the mean state one (5.17), we obtain an equation for the anomalous field, which can be considered linear if the differences between the product of perturbations and the time-mean product of perturbations (*i.e.* all the non-linear terms as $T'u' - \overline{T'u'}$) are replaced by a linear damping and a diffusion term. Physically speaking we are dissipating the non-linear eddies through a linear operator. Thus, for the thermodynamic equation we obtain:

$$\begin{aligned} \frac{\partial T'}{\partial t} = &-\frac{1}{a\cos\phi}\left[\frac{\partial}{\partial\lambda}\left(\overline{T}u' + T'\overline{u}\right) - \frac{\partial}{\partial\phi}\left(\cos\phi\left(\overline{T}v' + T'\overline{v}\right)\right)\right] + \\ &+ \overline{T}D' + T'\overline{D} - \overline{\dot{\eta}\frac{\partial p}{\partial\eta}\frac{\partial T'}{\partial\overline{p}}} - \dot{\eta}\frac{\partial p'}{\partial\eta}\frac{\partial\overline{T}}{\partial\overline{p}} - \\ &- \frac{R}{c_p}\overline{T}\left(\frac{\omega}{p}\right)' - \frac{R}{c_p}T'\overline{\left(\frac{\omega}{p}\right)} - \gamma(\eta)T' + k_H\nabla^4 T' \end{aligned} \tag{5.18}$$

By applying the same procedure in the equations for the other prognostic and diagnostic variables, we obtain the full set of relations which will be solved by the new numerical linear model. The complete set of equations solved by the model is reported below (equations (5.19)-(5.20)).

$$\frac{\partial\zeta'}{\partial t} = \frac{1}{a\cos^2\phi}\frac{\partial M_v}{\partial\lambda} - \frac{1}{a\cos\phi}\frac{\partial M_u}{\partial\phi} - \epsilon(\eta)\zeta' + k_H\nabla^4\zeta' \tag{5.19a}$$

$$\frac{\partial D'}{\partial t} = \frac{1}{a\cos^2\phi}\frac{\partial M_u}{\partial\lambda} + \frac{1}{a\cos\phi}\frac{\partial M_v}{\partial\phi} - \nabla^2(E' + \Phi') - \epsilon(\eta)D' + k_H\nabla^4 D' \tag{5.19b}$$

$$\begin{aligned} \frac{\partial T'}{\partial t} = &-\frac{1}{a\cos\phi}\left[\frac{\partial}{\partial\lambda}\left(\overline{T}u' + T'\overline{u}\right) - \frac{\partial}{\partial\phi}\left(\cos\phi\left(\overline{T}v' + T'\overline{v}\right)\right)\right] + \\ &+ \overline{T}D' + T'\overline{D} - \overline{\dot{\eta}\frac{\partial p}{\partial\eta}\frac{\partial T'}{\partial p}} - \dot{\eta}\frac{\partial p'}{\partial\eta}\frac{\partial\overline{T}}{\partial p} - \\ &- \frac{R}{c_p}\overline{T}\left(\frac{\omega}{p}\right)' - \frac{R}{c_p}T'\overline{\left(\frac{\omega}{p}\right)} - \gamma(\eta)T' + k_H\nabla^4 T' \end{aligned} \tag{5.19c}$$

$$\begin{aligned} \frac{\partial q'}{\partial t} = &-\left(\int_{(\eta_t)}^{(1)}\overline{\mathbf{V}}\nabla q' d\left(\overline{\frac{\partial p}{\partial\pi}}\right) + \int_{(\eta_t)}^{(1)}\mathbf{V}'\nabla\overline{q} d\left(\overline{\frac{\partial p}{\partial\pi}}\right) + \int_{(\eta_t)}^{(1)}\overline{\mathbf{V}}\nabla\overline{q} d\left(\frac{\partial p}{\partial\pi}\right)'\right) - \\ &- \frac{1}{\overline{\pi}}\left(\int_{p(\eta_t)}^{p(1)}\overline{D}dp' + \int_{p(\eta_t)}^{p(1)}D'd\overline{p}\right) \end{aligned} \tag{5.19d}$$

with:

$$
\begin{aligned}
E' =& u'\overline{u} + v'\overline{v} \\
M_v =& -\zeta'\overline{u} - (\overline{\zeta} + f)u' - \overline{\left(\dot{\eta}\frac{\partial p}{\partial \eta}\right)}\frac{\partial v'}{\partial \overline{p}} - \left(\dot{\eta}\frac{\partial p}{\partial \eta}\right)'\frac{\partial \overline{v}}{\partial \overline{p}} - \\
& - \frac{R}{a}\left(\overline{\frac{\partial p}{\partial \pi}}\right)\left[\frac{\overline{T}}{\overline{p}}\pi'\frac{\partial \overline{q}}{\partial \phi} + \frac{T'}{\overline{p}}\overline{\pi}\frac{\partial \overline{q}}{\partial \phi} + \frac{\overline{T}}{\overline{p}}\overline{\pi}\frac{\partial q'}{\partial \phi}\right] - \frac{R}{a}\left(\frac{\partial p}{\partial \pi}\right)'\frac{\overline{T}}{\overline{p}}\overline{\pi}\frac{\partial \overline{q}}{\partial \phi} \\
M_u =& \zeta'\overline{v} + (\overline{z} + f)v' - \overline{\left(\dot{\eta}\frac{\partial p}{\partial \eta}\right)}\frac{\partial u'}{\partial \overline{p}} - \left(\dot{\eta}\frac{\partial p}{\partial \eta}\right)'\frac{\partial \overline{u}}{\partial \overline{p}} - \\
& - \frac{R}{a\cos\phi}\left(\overline{\frac{\partial p}{\partial \pi}}\right)\left[\frac{\overline{T}}{\overline{p}}\pi'\frac{\partial \overline{q}}{\partial \lambda} + \frac{T'}{\overline{p}}\overline{\pi}\frac{\partial \overline{q}}{\partial \lambda} + \frac{\overline{T}}{\overline{p}}\overline{\pi}\frac{\partial q'}{\partial \lambda}\right] - \frac{R}{a\cos\phi}\left(\frac{\partial p}{\partial \pi}\right)'\frac{\overline{T}}{\overline{p}}\overline{\pi}\frac{\partial \overline{q}}{\partial \lambda}
\end{aligned}
$$

$$
\Phi' = R\left(\int_{p(\eta)}^{p(1)} \overline{T}\frac{dp'}{\overline{p}} + \int_{p(\eta)}^{p(1)} T'\frac{d\overline{p}}{\overline{p}}\right) \tag{5.20a}
$$

$$
\begin{aligned}
\omega' =& \left(\overline{\frac{\partial p}{\partial \pi}}\right)\left(\pi'\overline{\mathbf{V}}\nabla\overline{q} + \overline{\pi}\mathbf{V}'\nabla\overline{q} + \overline{\pi}\overline{\mathbf{V}}\nabla q'\right) + \left(\frac{\partial p}{\partial \pi}\right)'\left(\overline{\pi}\overline{\mathbf{V}}\nabla\overline{q}\right) - \\
& - \left[\int_{(\eta_t)}^{(\eta)} \pi'\overline{\mathbf{V}}\nabla\overline{q}d\left(\overline{\frac{\partial p}{\partial \pi}}\right) + \int_{(\eta_t)}^{(\eta)} \overline{\pi}\mathbf{V}'\nabla\overline{q}d\left(\overline{\frac{\partial p}{\partial \pi}}\right) + \right. \\
& \left. + \int_{(\eta_t)}^{(\eta)} \overline{\pi}\overline{\mathbf{V}}\nabla q'd\left(\overline{\frac{\partial p}{\partial \pi}}\right) + \int_{(\eta_t)}^{(\eta)} \overline{\pi}\overline{\mathbf{V}}\nabla\overline{q}d\left(\frac{\partial p}{\partial \pi}\right)'\right] - \\
& - \int_{p(\eta_t)}^{p(\eta)} \overline{D}dp' - \int_{p(\eta_t)}^{p(\eta)} D'd\overline{p}
\end{aligned} \tag{5.20b}
$$

$$
\begin{aligned}
\left(\dot{\eta}\frac{\partial p}{\partial \eta}\right)' =& \left(\overline{\frac{\partial p}{\partial \pi}}\right)\left[\int_{(\eta_t)}^{(1)} \pi'\overline{\mathbf{V}}\nabla\overline{q}d\left(\overline{\frac{\partial p}{\partial \pi}}\right) + \right. \\
& + \int_{(\eta_t)}^{(1)} \overline{\pi}\mathbf{V}'\nabla\overline{q}d\left(\overline{\frac{\partial p}{\partial \pi}}\right) + \int_{(\eta_t)}^{(1)} \overline{\pi}\overline{\mathbf{V}}\nabla q'd\left(\overline{\frac{\partial p}{\partial \pi}}\right) + \\
& \left. + \int_{(\eta_t)}^{(1)} \overline{\pi}\overline{\mathbf{V}}\nabla\overline{q}d\left(\frac{\partial p}{\partial \pi}\right)' + \int_{p(\eta_t)}^{p(1)} \overline{D}dp' + \int_{p(\eta_t)}^{p(1)} D'd\overline{p}\right] + \\
& + \left(\frac{\partial p}{\partial \pi}\right)'\left[\int_{(\eta_t)}^{(1)} \overline{\pi}\overline{\mathbf{V}}\nabla\overline{q}d\left(\overline{\frac{\partial p}{\partial \pi}}\right) + \int_{p(\eta_t)}^{p(1)} \overline{D}d\overline{p}\right] - \\
& - \left[\int_{(\eta_t)}^{(\eta)} \pi'\overline{\mathbf{V}}\nabla\overline{q}d\left(\overline{\frac{\partial p}{\partial \pi}}\right) + \int_{(\eta_t)}^{(\eta)} \overline{\pi}\mathbf{V}'\nabla\overline{q}d\left(\overline{\frac{\partial p}{\partial \pi}}\right) + \right. \\
& \left. + \int_{(\eta_t)}^{(\eta)} \overline{\pi}\overline{\mathbf{V}}\nabla q'd\left(\overline{\frac{\partial p}{\partial \pi}}\right) + \int_{(\eta_t)}^{(\eta)} \overline{\pi}\overline{\mathbf{V}}\nabla\overline{q}d\left(\frac{\partial p}{\partial \pi}\right)'\right] - \\
& - \left[\int_{p(\eta_t)}^{p(\eta)} \overline{D}dp' + \int_{p(\eta_t)}^{p(\eta)} D'd\overline{p}\right]
\end{aligned} \tag{5.20c}
$$

In the momentum and in the thermodynamic equations the Rayleigh friction:

$$
-\epsilon(\eta)\zeta', \qquad -\epsilon(\eta)D'
$$

and the Newtonian cooling:

$$-\gamma(\eta)T'$$

are included to take into account the ground dissipation and the radiation cooling. Moreover, the bi-harmonic diffusion for vorticity, divergence, and temperature accounts for the small scale dissipation.

5.2 The numerical linear model

To have a linear model consistent with the full non-linear version of CAM, we have to apply the same numerical scheme to solve equations (5.19)-(5.20). For this reason, recalling the main features of the numerical strategy adopted in the Eulerian Dynamical Core of CAM may be useful. In the full version of CAM the terms which are differentiated in the zonal and in the meridional directions, together with the residuals "undifferentiated" ones, are grouped separately and previously computed on a grid point domain. This grid point domain is defined to be consistent with the chosen spectral resolution. These terms are then transformed in the spectral space, where the horizontal differentiation, together with the forecast in time, is performed and all the terms are summed together to give the updated prognostic variable in the spectral space. Finally, the updated prognostic variables are transformed back onto the physical domain.

In our case, the new linearized terms, analytically described in the previous section, are introduced in the grid point computations, and then the same transform routines of the original CAM are exploited. As in the full version of CAM, the vertical differentiation is performed through a finite difference scheme. Given that our focus is the stationary linear response of the system, the time differentiation scheme has not been applied, and a further simplification has been introduced by applying the method described by Hoskins and Karoly in the already mentioned seminal work of 1981.

To solve the linear system, we just need to compute the linearized tendencies in the spectral domain:

$$(\frac{\partial \zeta^m_{n,k}}{\partial t}, \frac{\partial D^m_{n,k}}{\partial t}, \frac{\partial T^m_{n,k}}{\partial t}, \frac{\partial q^m_n}{\partial t})$$

Indeed, if we assume to write the linear system for the prognostic variables in a matrix fashion, the unforced problem becomes:

$$\dot{\mathbf{X}} = \mathbb{A}\mathbf{X} \tag{5.21}$$

where $\mathbf{X}$ is a vector including the spectral coefficients of the prognostic variables at each level

$$\mathbf{X} = \left[\zeta^m_{n,1}, \dots \zeta^m_{n,n_{lev}}, D^m_{n,1}, \dots, T^m_{n,1}, \dots q^m_n, \dots\right]^T$$

Once the representative matrix $\mathbb{A}$ is known, the linear system is fully determined: all the information described by the linear equations (5.19) are included in the matrix $\mathbb{A}$. Starting from the linearized tendencies $\dot{\mathbf{X}}$, we may notice that, if we consider an initial condition with:

$$X_k = \delta_{kl}$$

$\mathbb{A}$ may be derived one column at the time:

$$\dot{\mathbf{X}}_j = \mathbb{A}_{jk}\delta_{kl} = \mathbb{A}_{jl} \tag{5.22}$$

In other words, the l-*th* column of $\mathbb{A}$ is the vector with the linearized spectral coefficient tendencies for a numerical experiment with an initial condition equivalent to a spectral vector $\mathbf{X}$ with zero component everywhere, but 1 in the l-*th* position. Thus, for a forced steady state problem we can write:

$$0 = \mathbb{A}\mathbf{X} + \mathbf{F} \tag{5.23}$$

where $\mathbf{F}$ is a vector including the spectral coefficients of the stationary forcing. The response of the system to the applied forcing may be derived by solving the matrix problem:

$$\mathbb{A}\mathbf{X} = -\mathbf{F} \tag{5.24}$$

Give the resolution we have adopted (T31 with 26 vertical levels), by considering the total number of non-zero spectral coefficients, the square system dimension is 80817×80817. For this reason, it has been necessary to treat the system (5.24) adopting the parallelized linear algebra routines included in the ScaLAPACK library (Blackford et al., 1997). With this procedure, we have obtained a solution for the linear system always in terms of spectral coefficients. To have the prognostic fields on the grid point domain, the same transform routines exploited in the model have been applied.

As discussed in the previous section, a linear damping and a horizontal diffusion terms have been inserted, in order to take into account the dissipation of the small scale eddies, and the boundary effects. The horizontal diffusion is included through a bi-harmonic operator in the momentum and in the thermodynamic equations:

$$k_H \nabla^4 \zeta, \quad k_H \nabla^4 D, \quad k_H \nabla^4 T$$

In the spectral framework, the computation of the laplacian operator (and of the higher order analogous operators) is highly simplified by the eigenvector/eigenvalue relation:

$$\nabla^2 P_n^m(\mu) e^{im\lambda} = -\frac{n(n+1)}{a^2} P_n^m(\mu) e^{im\lambda}$$

For this reason the horizontal diffusion terms have been added in the spectral domain computation. By contrast, the Rayleigh friction and the Newtonian cooling terms, accounting for the dissipation at the boundaries, have been applied in the grid point domain before the computation of the Fourier and Legendre transforms.

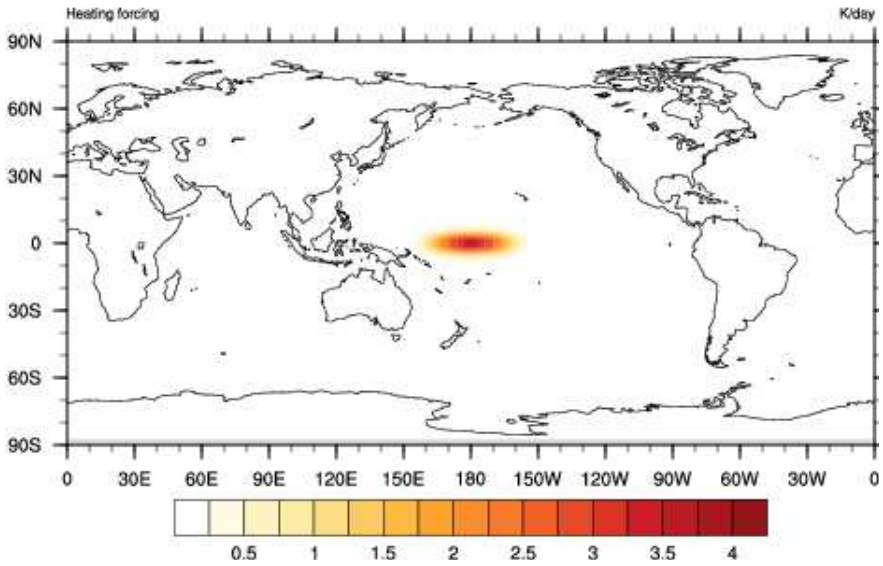

Figure 5.1: *Horizontal distribution of the idealized heating used in the test experiments. Values ranging from* 0 *to* 3.9 Kday^{-1}.

To summarize what we have seen so far, starting from the numerical scheme of the full non-linear Eulerian Dynamical Core of CAM, a new linearized version has been coded. The linearized terms are transformed in the spectral space, and from the set of linearized spectral tendencies the representative matrix of the linear system has been obtained, following the Hoskins and Karoly procedure. Once the matrix has been defined, through convenient inversion routines, it has been possible to solve the stationary forced linear problem. To check the consistency of the new model some preliminary tests have been performed. The main results are reported in the next section.

5.3 Preliminary tests

Before applying the new model for our final aims, some checks on it have been performed. To have some benchmark against which comparing the results from the new model, the idea has been to replicate some well-known experiments. In the details, we have tested the model with three basic state of increasing complexity: an analytical one, a zonal one, and a full asymmetric one. In all these cases, we have applied an idealized thermal forcing (figure (5.1)), the shape of which is given by:

$$Q(\lambda, \theta, \eta(p)) = Q_0 \sin\left(\pi\left(\frac{p}{p_0}\right)\right)\left[\sin\left(\pi\frac{(\lambda-\lambda_1)}{(\lambda_2-\lambda_1)}\right)\sin\left(\pi\frac{(\theta-\theta_1)}{(\theta_2-\theta_1)}\right)\right]^2 \tag{5.25}$$

and λ_1, λ_2, θ_1, and θ_2 define the position of the anomalous heating. In the vertical dimension, this function has a sinusoidal shape with its maximum in the mid of the troposphere, while tends to zero at the top and at the bottom of the air column. In the literature this is a typical choice used to approximate the anomalous heating due to deep convection. The

maximum amplitude Q_0 is reached in the mid of the troposphere, at about 500 hPa, and is equivalent to $3.9\,\mathrm{Kday}^{-1}$. However it should be noticed that in a linear framework the amplitude does not affect the structure of the response since it is always possible to rescale it. We recall here that in all the experiments we have performed, we have adopted the same horizontal (T31) and vertical (26 hybrid levels) resolution. The parameters of the model (linear damping and diffusivity) have been tuned depending on the complexity of the experiment, and, for this reason, we will specify them every time. It is important to stress that in particular the shape of the diffusion term may strongly influence the overall characteristics of the obtained response. On account of this, it is important to have consistency in the values of this coefficient when comparing results from different experiments.

5.3.1 Analytical basic state

In the first test we have considered an analytical basic state representing a solid body rotation, *i.e.* a state characterized by a constant vorticity. This means that just the zonal wind component is non-zero, while the temperature and the surface pressure have been fixed constant in every point of the domain.

$$\begin{aligned} \overline{u} &= u_0 \cos(\theta) \qquad & u_0 &= 15\,\mathrm{ms}^{-1} \\ \overline{v} &= 0 \\ \overline{T} &= 300\,\mathrm{K} \\ \overline{q} &= \ln(\overline{\pi}) & \overline{\pi} &= 10^5\,\mathrm{Pa} \end{aligned} \tag{5.26}$$

The horizontal diffusivity coefficient has been fixed to $2.338 \times 10^{16}\,\mathrm{m}^4\mathrm{s}^{-1}$, the Newtonian cooling coefficient has been held constant at all the vertical levels and equal to $\gamma^{-1} =$ 20.0day, while the Rayleigh damping is constant in the top 20 levels and is smoothly increasing over the last six:

$$\begin{array}{llll} \epsilon^{-1}(\eta_k) = 20.0\mathrm{day} & k = 1, \ldots, 20 & \epsilon^{-1}(\eta_k) = 16.0\mathrm{day} & k = 21 \\ \epsilon^{-1}(\eta_k) = 12.0\mathrm{day} & k = 22 & \epsilon^{-1}(\eta_k) = 6.0\mathrm{day} & k = 23 \\ \epsilon^{-1}(\eta_k) = 3.0\mathrm{day} & k = 24 & \epsilon^{-1}(\eta_k) = 2.0\mathrm{day} & k = 25, 26 \end{array}$$

The forcing (5.25) is located symmetrically across the Equator, with λ_1 =150E, λ_2 =210E, θ_1 =8S, θ_2 =8N. Given the symmetry in the basic state, at each latitude the zonal average has been subtracted from the imposed heating field Q, resulting in a forcing with a zero zonal mean everywhere.

In figures (5.2) the main results of this experiment are shown. The symmetry both in the forcing and in the basic state makes the structure of the response totally analogous in the two hemispheres. The upper and the low level wind pattern (figure (5.2a)-(5.2b)) show us the well-known Gill pattern (Gill, 1980): an easterly anomaly to the east of the forcing

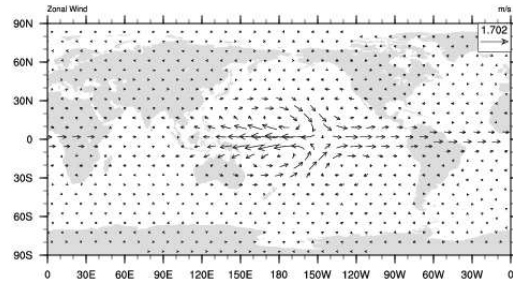

(a) 300 hPa *Zonal Wind*
(Solid Body Rotation)

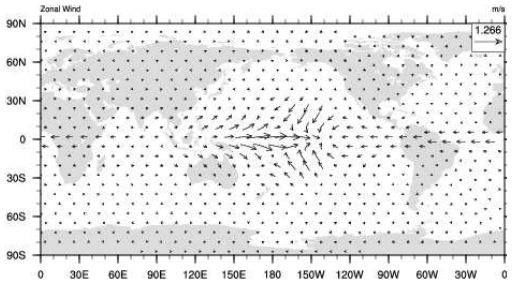

(b) 850 hPa *Zonal Wind*
(Solid Body Rotation)

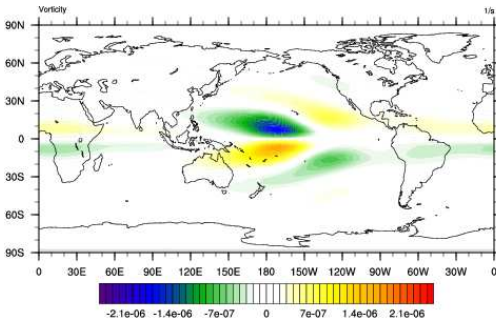

(c) 300 hPa *Vorticity*
(Solid Body Rotation)

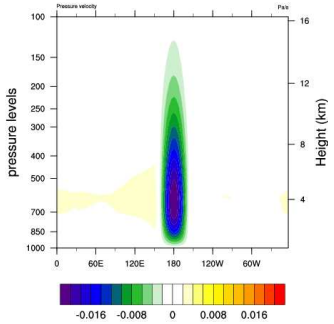

(d) *Vertical Pressure Velocity: longitude - vertical section at* 0N
(Solid Body Rotation)

Figure 5.2: *Solid Body Rotation Basic State: main results. In panel* (a) *and in panel* (b) *the magnitude of the vectors (expressed in* $\mathrm{m\,s^{-1}}$*) is reported in the legend. In panel* (c) *the values range from* $-2.4 \times 10^{-6}\,\mathrm{s^{-1}}$ *to* $2.4 \times 10^{-6}\,\mathrm{s^{-1}}$*, and in panel* (d) *the values range from* $-0.02\,\mathrm{Pas^{-1}}$ *to* $0.02\,\mathrm{Pas^{-1}}$.

region, and a westerly anomaly to the west of the forcing region at the lower levels, and a reversed pattern at the upper level. As in Gill analytical results, the anomalous easterlies are much more extended than the anomalous westerlies. In correspondence to the heating we can find a clear upward signal (figure (5.2d)), consistent with the convergence we see at the bottom, and the divergence we see at the top. Through the vorticity signal at 300 hPa (figure (5.2c)) we may see two symmetric trains of Rossby waves propagating northward/southward in the two hemisphere, and the signature of the Kelvin waves around the Equator. These results show an excellent agreement with the analytical theory. However it should be mentioned that, with such an idealized basic state, several terms in equations (5.19)-(5.20) disappear, so this experiment should not be considered as a definite test for our linear model. For this reason, in the next experiments a more complex reference state will be introduced.

5.3.2 Zonal basic state

Instead of the analytical solid body rotation, the basic state for this numerical exercise is the zonal average of a reference mean boreal winter condition (*i.e.* the mean winter state from the present day control simulation used in the experiments described in Chapter Four). Although it is a simplified symmetric reference state, differently from the previous experiment this basic state includes a meridionally varying three-dimensional field for the wind components and the temperature field. The planetary waves are strongly affected by the mean flow of the atmosphere, and, for this reason, their propagation is fostered by the natural enhancement of the subtropical jets during the winter season. The experimental setup is the same described above, with the forcing over the same equatorial region. The main results are reported in figure (5.3). A clear wave train propagating northward and eastward has been generated from the forcing region. If we look at the vorticity response at 300 hPa (figure (5.3a)) we may also see some evidence of the same split discussed by Hoskins and Karoly (1981), with a wave train proceeding over the north pole towards the opposite side of the hemisphere, and a wave train turning equatorward at about 45N. Also the geopotential height signal (figure (5.3b)) and the vertical structure (figure (5.3c)) are consistent with the known results.

5.3.3 Full asymmetric basic state

The last check we have performed is to test how the model reacts with a fully asymmetric basic state. We have decided to introduce the asymmetric basic state which will be used in the following part of this work: the same present day mean state used as a reference in the full non-linear exercises described in Chapter Four. We have applied the same forcing (5.25) over different regions, in our case centered at 180E and at 90E. Following Navarra (1990), who performs an analogous experiment, the horizontal diffusivity has been increased to $2.338 \times 10^{17}\,\mathrm{m^4 s^{-1}}$, while both the Rayleigh friction and the Newtonian cooling have been modified, adding some damping in the momentum also at the top of the model, and defining a vertical structure to the thermal damping coefficient γ. With these modifications, the shape of the damping coefficient becomes:

$$\epsilon^{-1}(\eta_k) = 20.0 \text{ day} \quad k = 7, \ldots, 20$$

$$\begin{array}{llll} \epsilon^{-1}(\eta_k) = 16.0 \text{ day} & k = 6, k = 21 & \epsilon^{-1}(\eta_k) = 12.0 \text{ day} & k = 5, k = 22 \\ \epsilon^{-1}(\eta_k) = 6.0 \text{ day} & k = 4, k = 23 & \epsilon^{-1}(\eta_k) = 3.0 \text{ day} & k = 3, k = 24 \\ \epsilon^{-1}(\eta_k) = 2.0 \text{ day} & k = 1, 2, k = 25 & \epsilon^{-1}(\eta_k) = 1.0 \text{ day} & k = 26 \end{array}$$

and

$$\gamma^{-1}(\eta_k) = 10.0 \text{ day} \quad k = 1, \ldots, 22$$

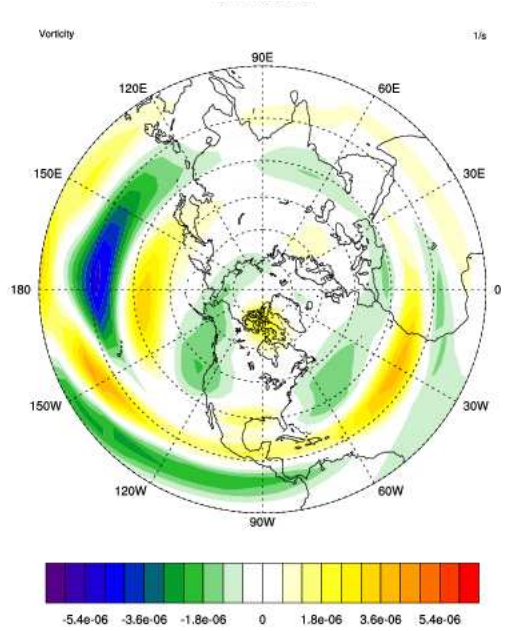

(a) 300 hPa *Vorticity*
(Zonal Mean Boreal Winter)

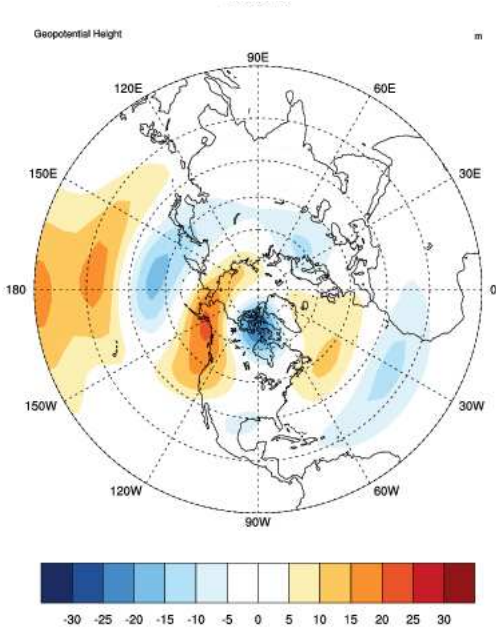

(b) 300 hPa *Geopotential Height*
(Zonal Mean Boreal Winter)

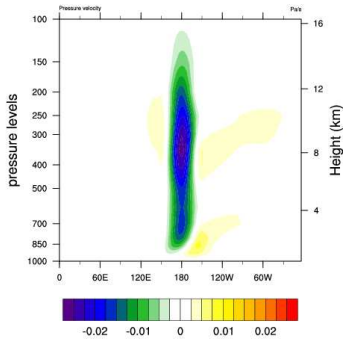

(c) *Vertical Pressure Velocity: longitude - vertical section at* 0N
(Zonal Mean Boreal Winter)

Figure 5.3: *Zonal Basic State: main results. In panel* (a) *the values range from* $-6 \times 10^{-6}\,\mathrm{s}^{-1}$ *to* $6 \times 10^{-6}\,\mathrm{s}^{-1}$*, in panel* (b) *the values range from* $-30\,\mathrm{m}$ *to* $30\,\mathrm{m}$*, and in panel* (c) *the values range from* $-0.025\,\mathrm{Pas}^{-1}$ *to* $0.025\,\mathrm{Pas}^{-1}$*.*

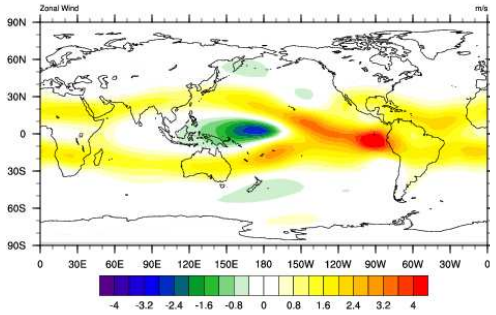

(a) 200 hPa *Zonal Wind*
(Asymmetric Basic State - Forcing at 180E)

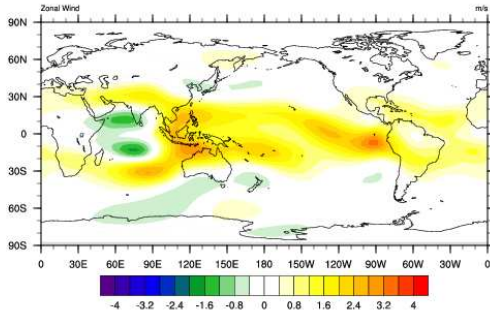

(b) 200 hPa *Zonal Wind*
(Asymmetric Basic State - Forcing at 90E)

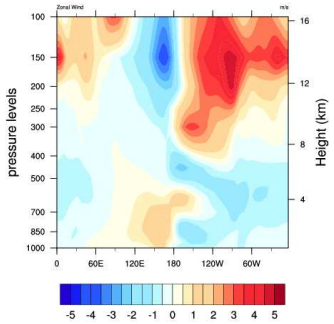

(c) *Zonal Wind: longitude - vertical section at* 0N
(Asymmetric Basic State - Forcing at 180E)

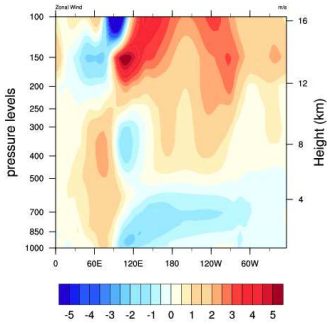

(d) *Zonal Wind: longitude - vertical section at* 0N
(Asymmetric Basic State - Forcing at 90E)

Figure 5.4: *Asymmetric Basic State: main results. In panel* (a) *and in panel* (b) *the values range from* $-4\,\mathrm{ms}^{-1}$ *to* $4\,\mathrm{ms}^{-1}$. *In panel* (c) *and in panel* (d) *the value range from* $-5\,\mathrm{ms}^{-1}$ *to* $5\,\mathrm{ms}^{-1}$.

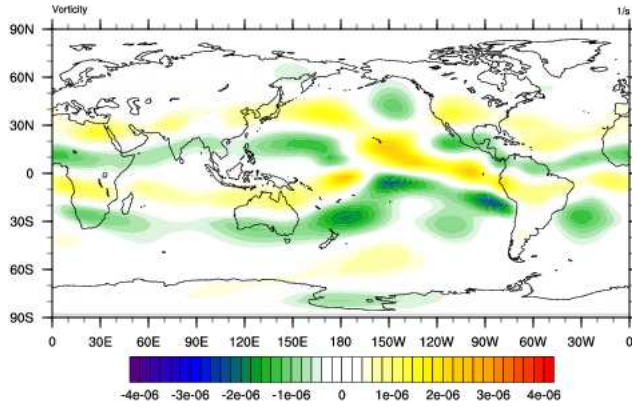

Figure 5.5: 300 hPa *Vorticity*
(Asymmetric Basic State - Forcing at 180E)
Values ranging from $-4 \times 10^{-6}\,\mathrm{s}^{-1}$ *to* $4 \times 10^{-6}\,\mathrm{s}^{-1}$.

$$\gamma^{-1}(\eta_k) = 8.0 \text{ day} \quad k = 23, 24 \qquad \gamma^{-1}(\eta_k) = 6.0 \text{ day} \quad k = 25,$$
$$\gamma^{-1}(\eta_k) = 4.0 \text{ day} \quad k = 26$$

Again with the idea of testing the performance of our linear model, let us compare the

main results of this set of experiments with the ones presented in Navarra (1990). In figure (5.4b)-(5.4a), the zonal velocity response at 200 hPa for the two experiments is reported. The basic feature, seen in the Gill-like experiment, may be found also in this case: there is a westward (negative) anomaly at the west of the source, and a eastward (positive) anomaly at the east of the forcing region. The patterns we have obtained strongly resemble the ones presented in Navarra's discussion. For instance, one may clearly notice the different shape and intensity of the westerly anomalous wind, depending on the position of the forcing. Also the vertical structure of the response is consistent: as in the reference one, also in our case as the forcing is moved eastward, the inversion point tends to occur at a lower level (figure (5.4d)-(5.4c)). If we look at the vorticity at 300 hPa, some hints of large scale propagation of Rossby waves from the heating region may be found (figure (5.5)). While in Navarra (1990) an observed January climatology has been adopted, we have used a year mean statistics. This different choice of the basic state may be the cause of the lower amplitude of the large scale pattern we have obtained.

Chapter 6

Linear Signature of a Localized CO_2 Forcing

As presented in the previous chapter, the results of the tests performed with our new linear model show a very good agreement with similar experiments in the literature. For this reason we may feel confident in exploiting this numerical tool to investigate the dynamical linear response related with the persistent and spatially non-homogenous anomaly of carbon dioxide concentration already discussed in Chapter Four.

In the previous part of this work, we used a general circulation model in oder to detect and discuss the signal due to an idealized perturbation of the CO_2 content in the atmosphere. A stationary "spot" of doubling CO_2 concentration, localized over different regions of the globe, has been included in the model simulations, and a statistically significant pattern has been obtained for all the considered positions of the forcing. In every case the wave-like signal resembles the PNA pattern, and, like the actual PNA mode of variability, our signal is also correlated with an anomalous dipole convective pattern over the Indian Ocean and the Western Tropical Pacific.

In the Eulerian Dynamical Core, the heating from the physical parametrization suite (*i.e.* from the part of the model which accounts for all the processes not explicitly solved by the primitive equations) acts as an effective forcing for the full non-linear dynamics. We have forced the stationary linear model with the global steady state anomalous heating pattern from the full non-linear experiment, in order to study in a linear framework the fingerprint related to the localized CO_2 concentration. The fact that the linear model shares the same numerical scheme and resolution with the full version of CAM guarantees the consistency of the results.

The analysis of the linear signal forced in such a way does not represent an attempt to evaluate the linearity of the system. Our goal is to obtain an assessment of the direct dynamical signature due to a localized CO_2 source on the state of the atmosphere. To the extent that the anomalous heating fields from the full general circulation model sim-

ulations are representative of the original carbon dioxide forcings, the linear experiments presented in this chapter will allow to obtain a dynamical fingerprint without the need of any additional assumptions.

In the next section we will describe the linear experiments, while in sections (6.2)-(6.3) the main results will be presented and discussed.

6.1 Rationale of the experiment and experimental design

In the setup of CAM exploited in this research, the primitive equations solved by the dynamical core are constrained by the output of the physical parametrization suite: the sources and sinks of momentum and temperature enter as an effective forcing, driving the dynamical response. In order to further investigate the signal we have already discussed in Chapter Four, our idea is to detect the linear response of the atmosphere to the same forcing which originally was accounted for in the full non-linear dynamics. The linear model described in Chapter Five provides us with an efficient and consistent numerical tool to accomplish this task.

We want to use in our linear framework the same forcing which in the non-linear experiment (described in Chapter Four) enters in the non-linear dynamical core. Under the assumption that the sources and sinks for the momentum equations are taken into account and parametrized by the small scale diffusion terms included in the linearized equations, we focus our attention on the heating forcing. The stationary heating forcing is defined as the difference between the heating (from the physical parametrization suite) of the forced experiments and the heating of the control one. With "heating" we are indeed considering the sum of the contributions from the different sub-components which makes up the parametrization suite. More precisely, we take into account the radiative heating - both the shortwave and longwave components -, the heating from the convective parametrization, and the turbulent component:

$$Q_{tot} = Q_{rad} + Q_{conv} + Q_{turb}$$

Again our metrics for the steady state forced signal is the ten-year ensemble mean difference.

For the three case experiments we are discussing (Pacific, Far East Asia, and North America), the shape of the steady state heating forcing at 500 hPa is shown in figures (6.1). In all three cases, we may notice how the heating signal is spread over the whole global domain; nevertheless some preferred spots may be found. Generally, over the regions originally affected by the anomalous CO_2 concentration, some positive signals may be

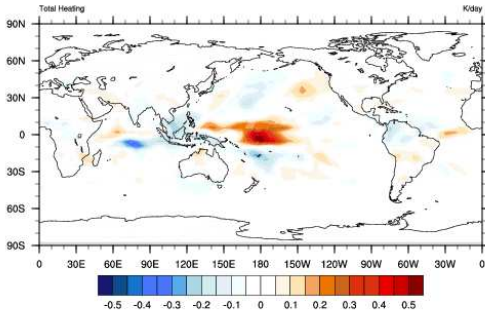

(a) 500 hPa *Stationary heating forcing* (Pacific Experiment)

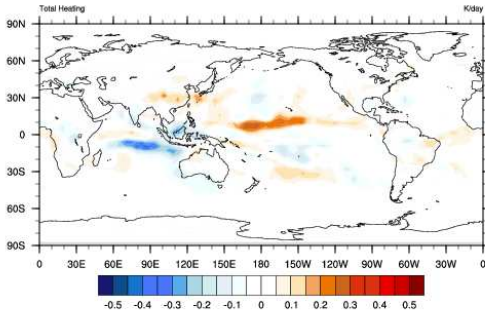

(b) 500 hPa *Stationary heating forcing* (Far East Asia Experiment)

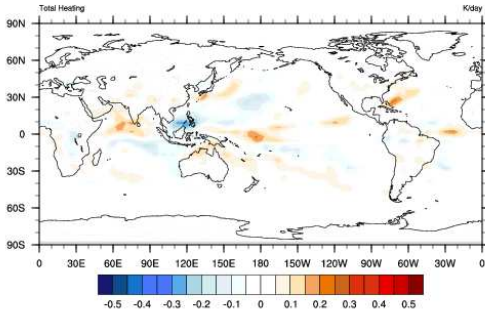

(c) 500 hPa *Stationary heating forcing* (North America Experiment)

Figure 6.1: *Forced minus control experiment - 10-year ensemble mean total heating at* 500 hPa: *convective + radiative + turbolent component.*
Values ranging from $-0.5\,\mathrm{Kday}^{-1}$ *to* $0.5\,\mathrm{Kday}^{-1}$

found. We may interpret this as related to the enhanced warming due to the local radiative effect of the carbon dioxide perturbation. A stronger anomaly is concentrated in the tropical region. If we recall the precipitation patterns in figures (4.6)-(4.9)-(4.12), we immediately recognise the convective contribution in this signal. Consistently with what observed in section (4.2), the Pacific and the Far East Asia experiments exhibit an enhanced convective activity over the tropical region, with a positive anomaly over the Western Pacific, and a negative anomaly over the Indian Ocean. We may find the same pattern in the heating signal, with a enhanced warming at the east and a cooling signal at the west of the Indonesian archipelago. As already noticed, the overall fingerprint in the North America experiment is less pronounced, and the same reverse pattern discussed for the precipitation field may be found also in the heating signal.

Once these forcings have been defined, they have been included in the linear computation, which has been performed following the same numerical procedure described in the previous chapter. The prognostic equations have been linearized against the present day mean state, which is the ten-year ensemble mean from the full non linear control simulation,

which in turn is the reference unforced state of the system for the full model experiments described in Chapter Four. Consistently, the model spatial resolution is not changed: also in this case we have a T31 horizontal spectral grid, and 26 vertical levels.

As already stressed when we have performed the sanity check experiments for our linear model, the choice of the model parameters, and in particular of the diffusivity coefficient, is a crucial element of the experimental design. In principle the shape of the response may be deeply affected by the the value of the diffusion term. For this reason, as more extensively discussed in the next sections, we have adopted different diffusion coefficients and tested the sensitivity of our results.

6.2 Linear experiment results

We have applied the new linear model to obtain the linear stationary response of the system to the three heating patterns described in the previous section. For each of them, we have performed a set of experiments in order to assess the sensitivity of the response to the choice of the diffusivity coefficients. Three different increasing values have been considered: $k_H = 2.338 \times 10^{17}\,\mathrm{m^4 s^{-1}}$, $k_H = 4.0 \times 10^{17}\,\mathrm{m^4 s^{-1}}$, and $k_H = 1.2 \times 10^{18}\,\mathrm{m^4 s^{-1}}$. The first one is the value adopted by Navarra (1990) in his linear experiment with an asymmetric basic state, the second one represents an intermediate choice, while the last one has been selected following Valdes and Hoskins (1989). In their analysis of the boreal winter stationary pattern, their linear model is discretized on the same horizontal resolution (T31) adopted in this framework. They apply a horizontal diffusivity constant corresponding to a 6 hour damping time on the smallest scale solved by the model, which, for a bi-harmonic operator, leads to the highest value among the three considered. Even if the amplitude of the response generally decreases as the diffusivity increases, nevertheless the overall patterns we have obtained turn out to be a robust feature of the system in all the three cases we have considered.

6.2.1 Pacific Experiment

Let us start form the Pacific experiment. The results from the three different diffusion coefficients are reported in figures (6.2), (6.3), and (6.4). If we look at the zonal winds at 200 hPa (figures (6.2a), (6.3a), (6.4a)), we may immediately notice a pattern which resembles the one observed for the test experiment in section (5.3.3). The pronounced heating around the Equator at about 180E yields the high level westerly wind over the Central and Eastern Equatorial Pacific, and the anomalous easterlies over the Western Equatorial Pacific. However, this is not the unique signal which may be detected. Each anomalous warming/cooling area acts as a potential source for wave propagation, depending on its

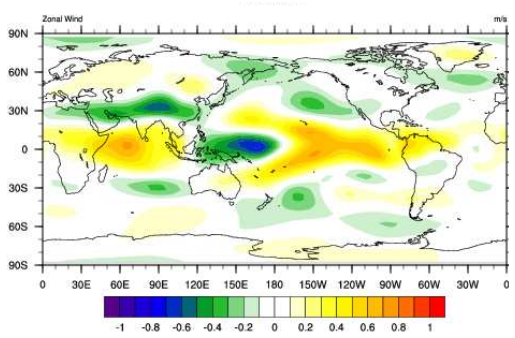

(a) 200 hPa *Zonal Wind*

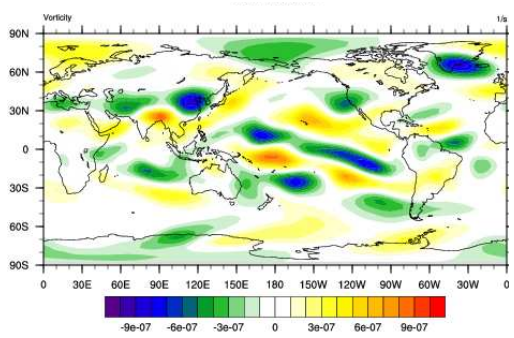

(b) 300 hPa *Vorticity*

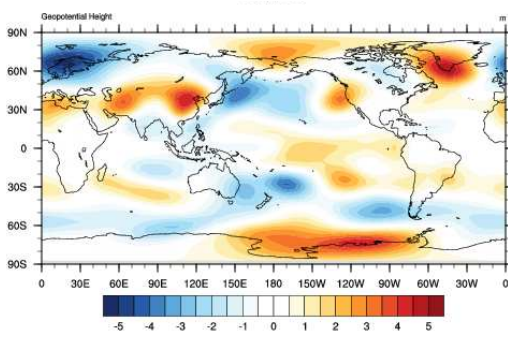

(c) 300 hPa *Geopotential Height*

Figure 6.2: *Stationary Linear Response for the Pacific Experiment (k_H =2.338 × 10^{17} m^4s^{-1}). In panel* (a) *the values range from* $-1\,ms^{-1}$ *to* $1\,ms^{-1}$, *in panel* (b) *the values range from* $-1 \times 10^{-6}\,s^{-1}$ *to* $1 \times 10^{-6}\,s^{-1}$, *and in panel* (c) *the values range from* $-5\,m$ *to* $5\,m$.

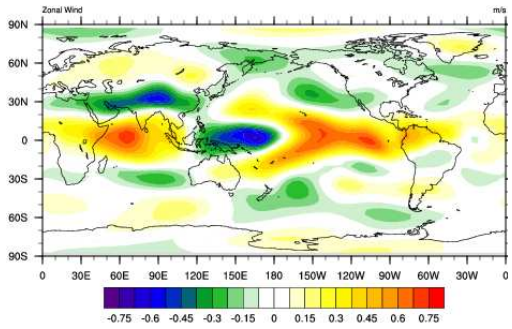

(a) 200 hPa *Zonal Wind*

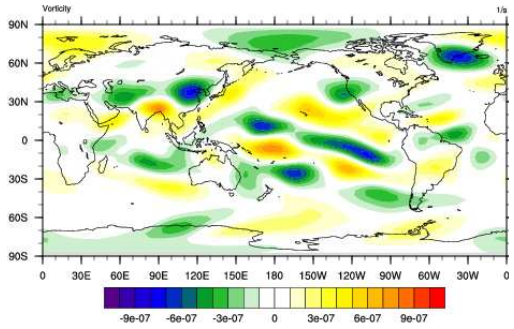

(b) 300 hPa *Vorticity*

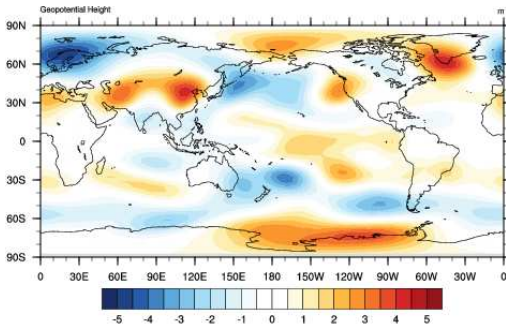

(c) 300 hPa *Geopotential Height*

Figure 6.3: *Stationary Linear Response for the Pacific Experiment* (k_H =$4.0 \times 10^{17}\,\mathrm{m^4 s^{-1}}$)*. In panel* (a) *the values range from* $-0.75\,\mathrm{ms^{-1}}$ *to* $0.75\,\mathrm{ms^{-1}}$*, in panel* (b) *the values range from* $-1 \times 10^{-6}\,\mathrm{s^{-1}}$ *to* $1 \times 10^{-6}\,\mathrm{s^{-1}}$*, and in panel* (c) *the values range from* $-5\,\mathrm{m}$ *to* $5\,\mathrm{m}$*.*

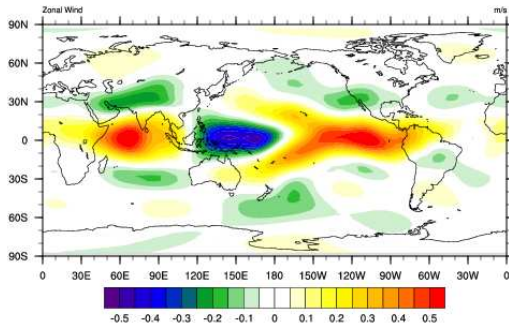

(a) 200 hPa *Zonal Wind*

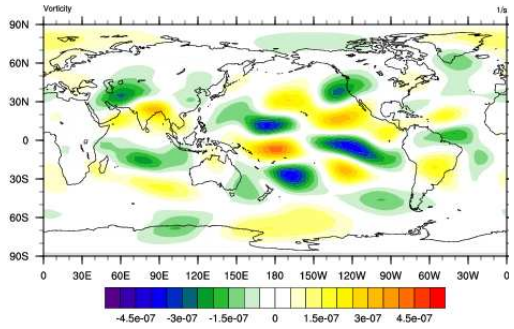

(b) 300 hPa *Vorticity*

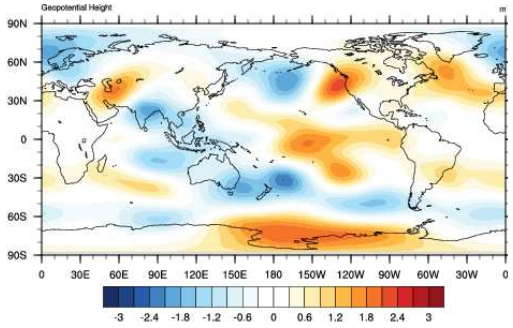

(c) 300 hPa *Geopotential Height*

Figure 6.4: *Stationary Linear Response for the Pacific Experiment* ($k_H = 1.2 \times 10^{18}\,\mathrm{m^4 s^{-1}}$). *In panel* (a) *the values range from* $-0.5\,\mathrm{ms}^{-1}$ *to* $0.5\,\mathrm{ms}^{-1}$, *in panel* (b) *the values range from* $-0.5 \times 10^{-6}\,\mathrm{s}^{-1}$ *to* $0.5 \times 10^{-6}\,\mathrm{s}^{-1}$, *and in panel* (c) *the values range from* $-3\,\mathrm{m}$ *to* $3\,\mathrm{m}$.

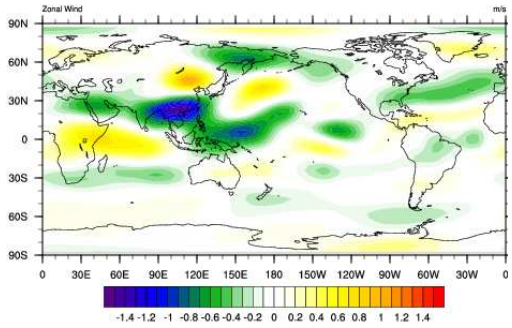

(a) 200 hPa *Zonal Wind*

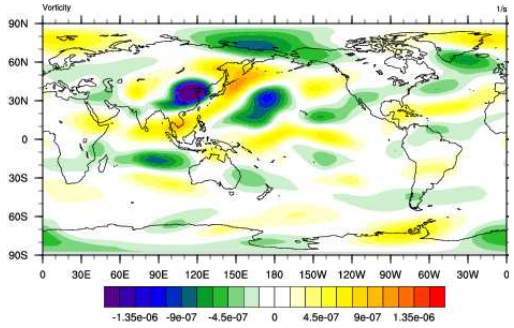

(b) 300 hPa *Vorticity*

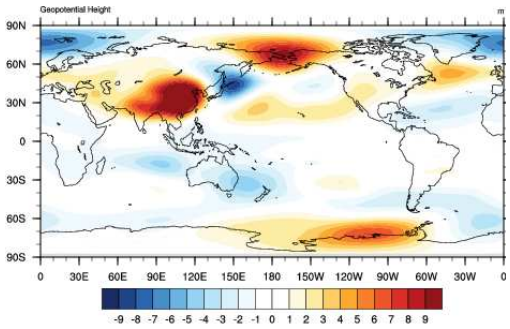

(c) 300 hPa *Geopotential Height*

Figure 6.5: *Stationary Linear Response for the Far East Asia Experiment* (k_H $=2.338 \times 10^{17}\,\mathrm{m^4 s^{-1}}$). *In panel* (a) *the values range from* $-1.5\,\mathrm{ms^{-1}}$ *to* $1.5\,\mathrm{ms^{-1}}$, *in panel* (b) *the values range from* $-1.5 \times 10^{-6}\,\mathrm{s^{-1}}$ *to* $1.5 \times 10^{-6}\,\mathrm{s^{-1}}$, *and in panel* (c) *the values range from* $-9\,\mathrm{m}$ *to* $9\,\mathrm{m}$.

amplitude and position. For example, the enhanced cooling in the Indian Ocean may be responsible for the positive (eastward) velocity anomaly over the Arabian Sea, even if the superposition of the different signals makes it difficult to recognise the expected negative (westward) anomalous wind at the east of the same negative source. If we look at the 300 hPa vorticity signal (figures (6.2b), (6.3b), (6.4b)), the wave train generated by the Tropical Pacific source and extended over Greenland may be clearly detected. Some hints may be found also of some wave propagation from the Indian Ocean regions along the Pacific coast of the Asian continent. The 300 hPa geopotential height pattern is totally consistent, showing the large scale features of the response (figures (6.2c), (6.3c), (6.4c)).

By comparing the patterns we have obtained for the experiments with different diffusivity, we notice that the main characteristics of the overall patterns are conserved, even if, as one may expect, the intensity of the maxima and the minima is generally damped as the diffusion in the model becomes stronger.

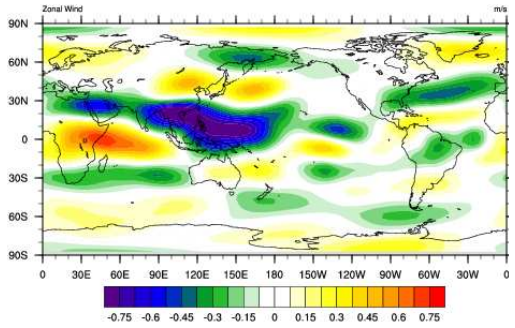

(a) 200 hPa *Zonal Wind*

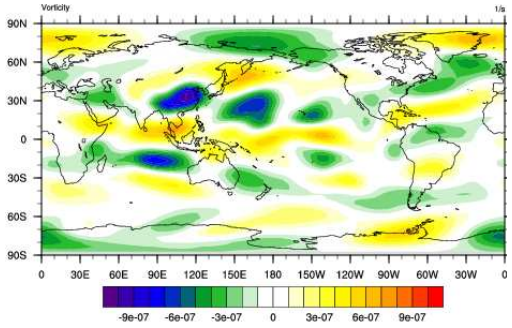

(b) 300 hPa *Vorticity*

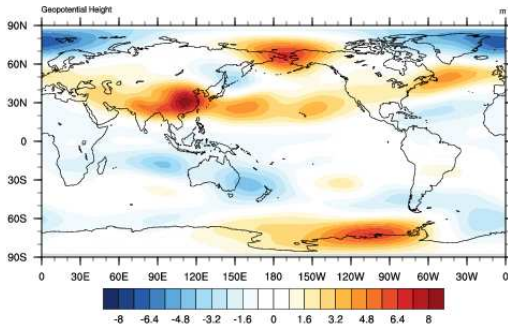

(c) 300 hPa *Geopotential Height*

Figure 6.6: *Stationary Linear Response for the Far East Asia Experiment* (k_H $=4.0 \times 10^{17}\,\mathrm{m^4 s^{-1}}$). *In panel* (a) *the values range from* $-0.75\,\mathrm{ms^{-1}}$ *to* $0.75\,\mathrm{ms^{-1}}$, *in panel* (b) *the values range from* $-1 \times 10^{-6}\,\mathrm{s^{-1}}$ *to* $1 \times 10^{-6}\,\mathrm{s^{-1}}$, *and in panel* (c) *the values range from* $-8\,\mathrm{m}$ *to* $8\,\mathrm{m}$.

6.2.2 Far East Asia Experiment

Also in this case we report the results from all the three sensitivity experiments (figures (6.5), (6.6), (6.7)). The heating pattern which forces this set of simulations (figure (6.1b)) shows three main structures, generally elongated in the zonal direction: the warming/cooling from the convective anomaly over the Central Pacific and the Indian Ocean, and the local radiative positive signal over continental South East Asia. The combination of the responses to these three sources yields a strong local effect, roughly over the region where the original CO_2 forcing was applied, together with a distinct hemispheric-wide signal.

If we look at the 200 hPa zonal wind signal (figures (6.5a), (6.6a), (6.7a)) a clear westward (negative) anomaly may be found over China up to the Western Equatorial Pacific, with a wave-like signal propagating northward and eastward from that region. The large scale signal emerges more distinctly by considering the 300 hPa vorticity pattern - shown in figures (6.5b), (6.6b), (6.7b) - and the 300 hPa geopotential height, reported in

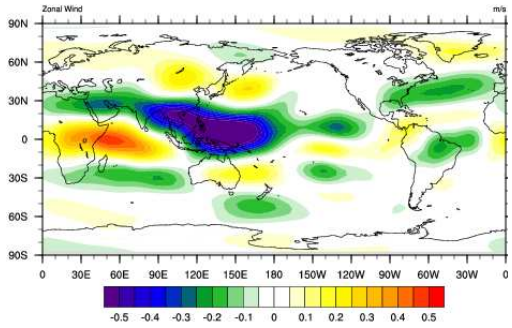

(a) 200 hPa *Zonal Wind*

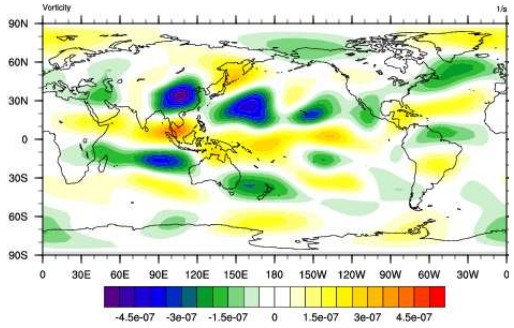

(b) 300 hPa *Vorticity*

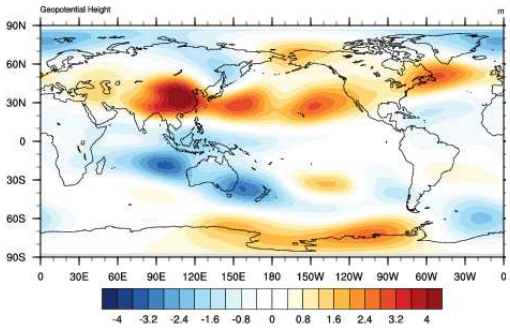

(c) 300 hPa *Geopotential Height*

Figure 6.7: *Stationary Linear Response for the Far East Asia Experiment* (k_H $=1.2 \times 10^{18}\,\mathrm{m^4 s^{-1}}$). *In panel* (a) *the values range from* $-0.5\,\mathrm{ms^{-1}}$ *to* $0.5\,\mathrm{ms^{-1}}$, *in panel* (b) *the values range from* $-0.5 \times 10^{-6}\,\mathrm{s^{-1}}$ *to* $0.5 \times 10^{-6}\,\mathrm{s^{-1}}$, *and in panel* (c) *the values range from* $-4\,\mathrm{m}$ *to* $4\,\mathrm{m}$.

figures (6.5c), (6.6c), and (6.7c). There is a clear waveguide pattern across the Pacific basin up to the eastern coast of the North America continent, and some hints of an analogous pattern may be found also in the Southern Hemisphere. Again the results have been shown not to be influenced in their general structure by the value of the diffusivity coefficients.

6.2.3 North America Experiment

As already noticed, the structures present in the forcing for the North America experiment are generally characterized by a much lower amplitude with respect to the other two cases we have considered. Nevertheless, some clear maxima and minima may be found, also in this case, across the Indo-Pacific region. Thus, one may expect to find a generally less intense response in this case with respect to the other ones we have analysed. Indeed, if we look at the results in figures (6.8)-(6.10), this *a priori* guess is confirmed. For instance, if we look at the 200 hPa zonal wind stationary anomalies (figures (6.8a), (6.9a), (6.10a)), in the Far East Asia experiment the magnitude of the signal is about twice as large as the

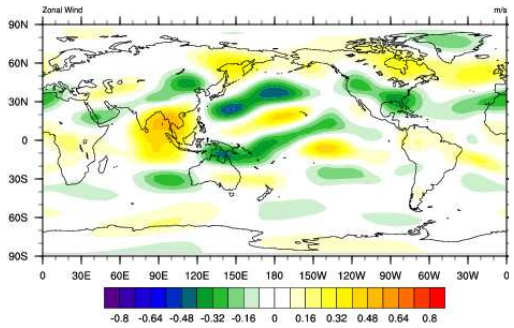

(a) 200 hPa *Zonal Wind*

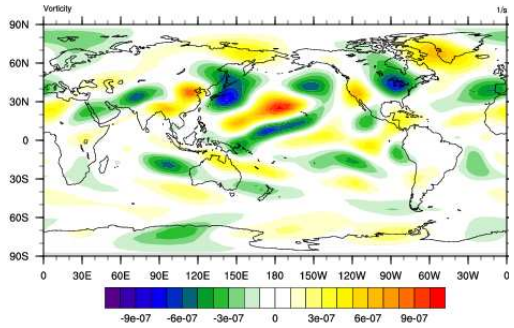

(b) 300 hPa *Vorticity*

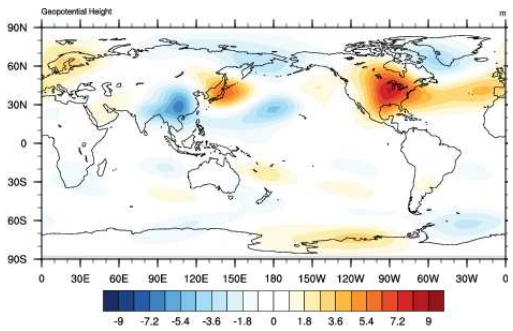

(c) 300 hPa *Geopotential Height*

Figure 6.8: *Stationary Linear Response for the North America Experiment* (k_H $=2.338 \times 10^{17}\,\mathrm{m^4 s^{-1}}$). *In panel* (a) *the values range from* $-0.8\,\mathrm{ms^{-1}}$ *to* $0.8\,\mathrm{ms^{-1}}$, *in panel* (b) *the values range from* $-1 \times 10^{-6}\,\mathrm{s^{-1}}$ *to* $1 \times 10^{-6}\,\mathrm{s^{-1}}$, *and in panel* (c) *the values range from* $-9\,\mathrm{m}$ *to* $9\,\mathrm{m}$.

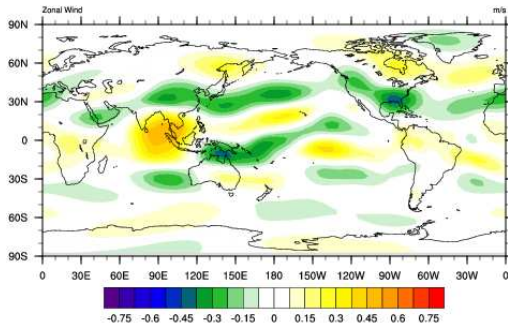

(a) 200 hPa *Zonal Wind*

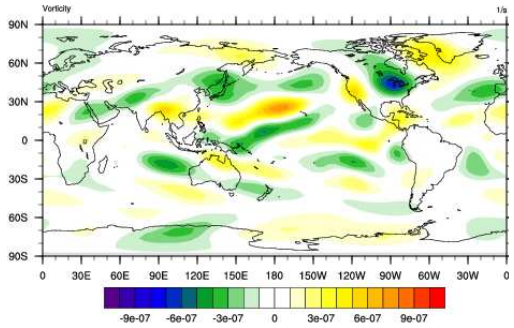

(b) 300 hPa *Vorticity*

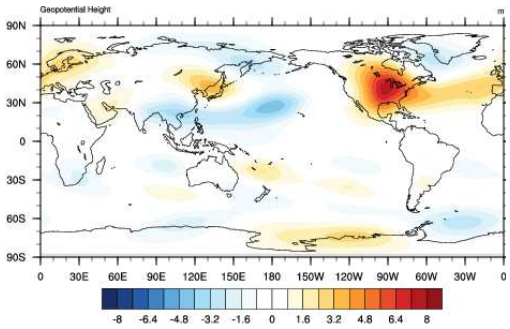

(c) 300 hPa *Geopotential Height*

Figure 6.9: *Stationary Linear Response for the North America Experiment* (k_H $=4.0 \times 10^{17}\,\mathrm{m^4 s^{-1}}$). *In panel* (a) *the values range from* $-0.75\,\mathrm{ms^{-1}}$ *to* $0.75\,\mathrm{ms^{-1}}$, *in panel* (b) *the values range from* $-1 \times 10^{-6}\,\mathrm{s^{-1}}$ *to* $1 \times 10^{-6}\,\mathrm{s^{-1}}$, *and in panel* (c) *the values range from* $-8\,\mathrm{m}$ *to* $8\,\mathrm{m}$.

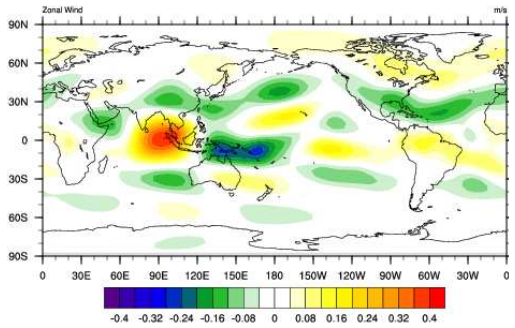

(a) 200 hPa *Zonal Wind*

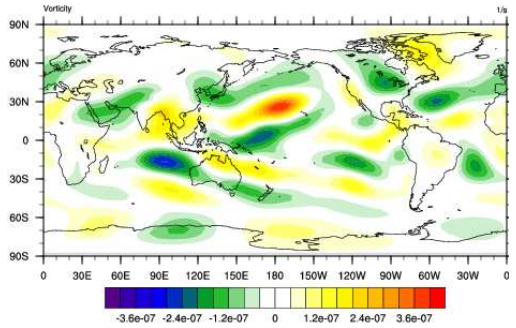

(b) 300 hPa *Vorticity*

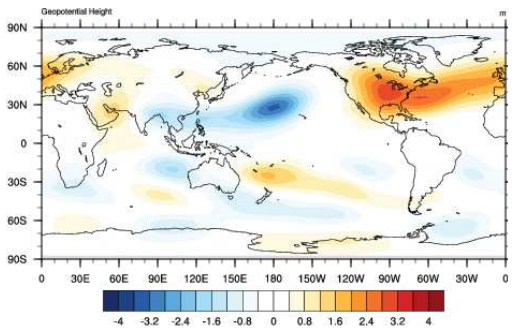

(c) 300 hPa *Geopotential Height*

Figure 6.10: *Stationary Linear Response for the North America Experiment* (k_H $=1.2 \times 10^{18}\,\mathrm{m^4 s^{-1}}$). *In panel* (a) *the values range from* $-0.4\,\mathrm{ms^{-1}}$ *to* $0.4\,\mathrm{ms^{-1}}$, *in panel* (b) *the values range from* $-0.4 \times 10^{-6}\,\mathrm{s^{-1}}$ *to* $0.4 \times 10^{-6}\,\mathrm{s^{-1}}$, *and in panel* (c) *the values range from* $-4\,\mathrm{m}$ *to* $4\,\mathrm{m}$.

amplitude of the North America experiment response, given the same value of the diffusion coefficient.

For this experiment, together with the enhanced circulation anomalies in the Indo-Pacific equatorial region, a localized effect over the North America continent may be found (figures (6.8b), (6.9b), (6.10b)). The sign of the Indo-Pacific signal is clearly affected by the sign of the convective dipole across the Indonesian Archipelago. If we look at the 300 hPa geopotential height, we may notice how the amplitude of the wave-like signal, which from South East Asia propagates along the Pacific coast of the Asian continent, is much less pronounced than in the previous case, while a relatively strong high pressure anomaly may be found over the Eastern North America continent, which is elongated over the Atlantic region.

As one may notice by comparing figures (6.8), (6.9), and (6.10) also in this case the results appear to be insensitive in the large scale pattern to the choice of the diffusivity coefficients.

6.3 Summary and discussion of the experimental results

In order to further assess the response of the atmosphere to a localized CO_2 forcing, we have performed a set of stationary linear experiments with a numerical linear model, designed to be totally consistent with the full version of CAM previously exploited. The three-dimensional stationary heating anomalies, related to the original carbon dioxide forcing, have been accounted for as forcings for the linear system. These steady state heating anomalies have been defined in terms of ten-year ensemble mean difference between the heating rates of the forced and of the control experiments, described in Chapter Four.

The results we have obtained are robust with respect to the choice of the diffusion coefficient. A good agreement is found across the different sensitivity tests we have performed, not just in the large scale pattern, but also in the position of the maxima and minima detected in the analysed fields. This makes us confident in interpreting the signal we have obtained and commented as the actual signature due to the applied forcing. Moreover, it should be mentioned that, when analysing the output from a linear experiment, the main focus is in the shape of the obtained patterns, and not in their amplitude. We have considered the amplitude just to have an idea of the relative magnitude of the responses in the different experiments and geographical location.

Also in this case, the so-called "Pacific" experiment acts as a reference exercise. Indeed, even if we have applied an empiric forcing, the main features of the response recalls the ones seen for the idealized experiment described in section (5.3.3). By contrast, the other

two experiments offer a much more unexpected picture.

The effective heating in the North America case is much less intense, locally and globally, than the Far East Asia case. Moreover, the relative position of the thermal sources and sinks are different in the two instances. The net result is that, while in the Far East Asia experiment the stationary wave trains generated from the main heating sources expand in all the domain, in the North America one they tend to be dissipated, affecting a much smaller portion of the global domain. The most prominent feature of the Far East Asia experiment response is the waveguide signal which extends across the Pacific, towards the North American continent and seems to be extended also over the Atlantic region. Remarkably, a similar pattern may be found also in the Southern Hemisphere region, as further proof of the actual large scale extension of this response.

These linear results show that, although the originally considered carbon dioxide anomaly is the same in both cases, the linear dynamical stationary responses are different, depending on the location of the forcing. Even if through the non-linear experiment we have detected a somehow similar PNA-like pattern in both cases, the linear exercise reveals that the stationary linear dynamical signal related to these two patterns is characterized by a different shape and, most of all, a different spatial extension, suggesting South East Asia as a particular sensitive forcing region in terms of both local and global response.

Summary and Conclusions

In this research different aspects of the atmospheric response to carbon dioxide forcing have been considered.

In the first part, the main focus has been on detecting the response function of the atmospheric system. This approach has been widely used in many fields of physics, and in climate change literature it provides a reduced-model to approximate, in multi-disciplinary assessment, the outcomes of full GCM simulations. We are interested in the response function as it represents, from a dynamical point of view, the elementary response of the system to a given forcing. Since it is impossible to define the deterministic relation which rules the interactions between climate variables - in our case the surface temperature - and carbon dioxide concentration, we exploit a GCM and introduce in our simulations an impulsive CO_2 forcing. While the response function, as usually defined in the literature, gives information just on the mean behaviour of the considered variable, in our case we have been able to obtained directly also the full spatial pattern related to the pulse response, without making any *a priori* assumption on the shape of this response.

We have obtained two main results. First of all, the response of a pulse can be detected as the first EOF mode of a simulation accounting for an impulsive forcing. The related spatial pattern shows a positive signal in all the domain, mainly concentrated in the tropical area. This feature is robust, as we have verified by imposing in our experimental setup different initial conditions, and both a continuous and a discrete pulse forcing. On the other hand, our approach has provided us with an estimate of the "fast" response of climate system to the CO_2 forcing. The time the model requires to recover from the effects of the impulsive forcing is about 15 years, and this estimate has been obtained independently of the choice made to approximate the shape of the pulse in the simulation. It is important to stress how these results represent the pure atmospheric-related signal, given the experimental setup we have adopted. Both the spatial shape and the temporal scale we have detected would have been deeply different, if the effects of the ocean had been taken into account.

In the second part of this research, we concentrate on the effects on the atmospheric state of a stationary and non-homogeneous spatial distribution of carbon dioxide concentration. The idea was to detect whether a localized CO_2 anomaly might be effective on

atmospheric variability, and in that case gather some insights on the possible shape of the response. We have performed a set of idealized experiments: a stationary doubling spot of carbon dioxide has been switched on over different regions of the global domain in order to investigate the sensitivity of the system to the position of the forcing. While the "Pacific" experiment may be considered as a benchmark test, the choice of including a forcing over South East Asia and North America has been made as the available data suggest that in this region there is indeed a persistent, even if small, positive anomaly in the actual carbon dioxide distribution in the atmosphere. By looking at the stationary response in terms of the difference between the ensemble and time mean of the forced and the unforced simulations, a statistically significant pattern has been detected in all the three cases. This wave-like signal at the mid-to-high latitudes of the Northern Hemisphere, resembles the PNA pattern, and, like the PNA observed in natural variability, it is related to an anomaly in the convective structure over the Indo-Pacific area.

In oder to further investigate the effects of a localized CO_2 forcing, we have decided to define the stationary dynamical linear response of the system. A new linear model has been implemented. It is the first attempt to linearize the actual Eulerian Dynamical Core of CAM. The introduction of the hybrid coordinates in the vertical dimension radically changes the shape of the equations, making our model totally independent of the previous linearized CAM which may be found in the literature (Branstator, 1990). The linear model shares the same numerical scheme and resolution of the full-version of CAM used in the previous simulations of this research, and it solves the stationary problem by inverting the characteristic matrix of the system. It is important to notice how the introduction of this new numerical tool represents an important result independently of the focus of this research, as it is an efficient tool to assess the dynamical response of the atmosphere to steady state forcings.

By introducing in this linearized framework the stationary heating signal which, in the full CAM experiments, originally forces the non-linear dynamical model, we obtained some interesting results. In both the Far East Asia and in the North America experiment some signal may be found in all the global domain, but in the first case, a pattern with a stronger amplitude and a more pronounced spatial extension seems to be enhanced.

From this set of idealized experiments there are two main lessons which may be drawn. First of all, a stationary localized anomalous concentration of carbon dioxide may be effective on atmospheric variability. The signals we have detected arise in a totally idealized framework, where, nevertheless, the key aspect has been the persistency of the forcing. An analogous persistency is observed in the actual carbon dioxide distribution, with some preferred accumulation areas. Moreover, looking at the linearized response has allowed to achieve a much more direct assessment on the shape of the response. Our second noteworthy point is that some regions seem to be more effective than others in terms of

both spatial extent and amplitude of the response. In particular, for the cases we have considered, South East Asia may be proposed as a particular sensitive forcing area.

Starting from the results we have obtained, a number of possible future extensions of this research may be envisaged. First of all, a natural complement to our analysis may be an application of the same methodology to other possible regions (*e.g.* Europe), in order to have a more complete picture of the sensitivity of the system to the position of the forcing. Secondly, our results have obviously been derived under a set of idealized conditions, hence a better insights might be gathered by working with a more realistic framework. Finally, the overall perspective suggested in this research, that the persistent localized carbon dioxide forcing may have an effect on the global scale whose magnitude depends on the particular localization, might point to significant policy implications, which should call for specific inquiries.

Bibliography

Bitz, C., and Coauthors, 2012: Climate Sensitivity of the Community Climate System Model, Version 4. *Journal of Climate*, **25 (9)**, 3053–3070.

Blackford, L., and Coauthors, 1997: *ScaLAPACK Users' Guide*, Vol. 4. Society for Industrial and Applied Mathematics.

Boville, A., and C. Bretherton, 2003: Heating and Kinetic Energy Dissipation in the NCAR Community Atmosphere Model. *Journal of Climate*, **16 (23)**, 3877–3887.

Branstator, G., 1985: Analysis of General Circulation Model Sea-Surface Temperature Anomaly Simulations Using a Linear Model. Part I: Forced Solutions. *Journal of the Atmospheric Sciences*, **42 (21)**, 2225–2241.

Branstator, G., 1990: Low-Frequency Patterns Induced by Stationary Waves. *Journal of the Atmospheric Sciences*, **47 (5)**, 629–649.

Branstator, G., 2014: Long-Lived Response of the Midlatitude Circulation and Storm Tracks to Pulses of Tropical Heating. *Journal of Climate*, **27 (23)**, 8809–8826.

Chahine, M., and Coauthors, 2008: Satellite remote sounding of mid-tropospheric CO_2. *Geophysical Research Letters*, **35 (17)**.

Craig, A., M. Vertenstein, and R. Jacob, 2011: A new flexible coupler for Earth system modeling developed for CCSM4 and CESM1. *International Journal of High Performance Computing Applications*.

Danabasoglu, G., and P. Gent, 2009: Equilibrium Climate Sensitivity: Is It Accurate to Use a Slab Ocean Model? *Journal of Climate*, **22 (9)**, 2494–2499.

Denning, A., Y. Fung, and D. Randall, 1995: Latitudinal gradient of atmospheric CO_2 due to seasonal exchange with land biota. *Nature*, **376 (6537)**, 240–243.

Edwards, P., 2011: History of climate modeling. *WIREs Climate Change*, **2 (1)**, 128–139.

Franzke, C., S. Feldstein, and S. Lee, 2011: Synoptic analysis of the Pacific-North American teleconnection pattern. *Quart. J. Roy. Meteor. Soc.*, **137 (655)**, 329–346.

Fung, I., and Coauthors, 1983: Three-Dimensional Tracer Model Study of Atmospheric CO_2: Response to Seasonal Exchanges With the Terrestrial Biosphere. *Journal of Geophysical Research*, **88 (C2)**, 1281–1294.

Gill, A., 1980: Some simple solutions for heat-induced tropical circulation. *Quart. J. Roy. Meteor. Soc.*, **106 (449)**, 447–462.

Gurney, K., and Coauthors, 2002: Towards robust regional estimates of CO_2 source and sinks using atmospheric transport models. *Nature*, **415 (6872)**, 626–630.

Hannachi, A., I. Jolliffe, and D. Stephenson, 2007: Empirical orthogonal functions and related techniques in atmospheric sciences: A review. *International Journal of Climatology*, **27 (9)**, 1119–1152.

Hasselmann, K., and Coauthors, 1997: Sensitivity Study of Optimal CO_2 Emission Paths Using a Simplifed Structural Integrated Assessment Model (SIAM). *Climatic Change*, **37 (2)**, 345–386.

Hasselmann, K., R. Sausen, E. Maier-Reimer, and R. Voss, 1993: On the cold start problem in transient simulations with coupled atmosphere-ocean models. *Climate Dynamics*, **9 (2)**, 53–61.

Hegerl, G., and F. Zwiers, 2011: Use of models in detection and attribution of climate change. *WIREs Climate Change*, **2 (4)**, 570–591.

Held, I., R. Panetta, and R. Pierrehumbert, 1985: Stationary External Rossby Waves in Vertical Shear. *Journal of the Atmospheric Sciences*, **42 (9)**, 865–883.

Held, I., and Coauthors, 2010: Probing the Fast and Slow Components of Global Warming by Returning Abruptly to Preindustrial Forcing. *Journal of Climate*, **23 (9)**, 2418–2427.

Hooss, G., and Coauthors, 2001: A nonlinear impulse response model of the coupled carbon cycle-climate system (NICCS). *Climate Dynamics*, **18 (3-4)**, 189–202.

Hoskins, B., and T. Ambrizzi, 1993: Rossby Wave Propagation on a Realistic Longitudinally Varying Flow. *Journal of the Atmospheric Sciences*, **50 (12)**, 1661–1671.

Hoskins, B., and D. Karoly, 1981: The Steady Linear Response of a Spherical Atmosphere to Thermal and Orographic Forcing. *Journal of the Atmospheric Sciences*, **38 (6)**, 1179–1196.

Hunke, E., and W. Lipscom, 2010: CICE: the Los Alamos Sea Ice Model Documentation and Software User's Manual - Version 4.1. Technical Report LA-CC-06-012, Los Alamos National Laboratory.

Hurrell, J., and Coauthors, 2013: The Community Earth System Model - A Framework for Collaborative Research. *Bulletin of the American Meteorological Society*, **94 (9)**, 1339–1360.

Jiang, X., and Coauthors, 2010: Interannual variability of mid-tropospheric CO_2 from atmospheric infrared sounder. *Geophysical Research Letters*, **37 (13)**.

Johnson, N., and S. Feldstein, 2010: The Continuum of North Pacific Sea Level Pressure Patterns: Interseasonal, Interannual, and Interdecadal Variability. *Journal of Climate*, **23 (4)**, 851–867.

Linter, B., 2002: Characterizing global CO_2 interannual variability with empirical orthogonal function/principal component (EOF/PC) analysis. *Geophysical Research Letters*, **29 (19)**.

Liu, M., Z. Alexander, 2007: Atmospheric Bridge, Oceanic Tunnel, and Global Climatic Teleconnections. *Reviews of Geophysics*, **45 (2)**.

Machenhauer, B., 1979: The spectral methods. *Numerical Methods Used in Atmospheric Models*, World Meteorological Organization, Geneva, Switzerland.

Manabe, S., R. Stouffer, M. Spelman, and K. Bryan, 1991: Transient Responses of a Coupled Ocean-Atmosphere Model to Gradual Changes of Atmospheric CO_2. Part I: Annual Mean Response. *Journal of Climate*, **4 (8)**, 785–818.

Manabe, S., and R. Wetherald, 1967: Thermal Equilibrium of the Atmosphere with a Given Distribution of Relative Humidity. *Journal of the Atmospheric Sciences*, **4 (3)**, 241–259.

Manabe, S., and R. Wetherald, 1975: The Effects of Doubling the CO_2 Concentration on the Climate of a General Circulation Model. *Journal of the Atmospheric Sciences*, **32 (1)**, 3–15.

Navarra, A., 1990: Steady Linear Response to Thermal Forcing of an Anomaly Model with an Asymmetric Climatology. *Journal of the Atmospheric Sciences*, **47 (2)**, 148–169.

Navarra, A., and V. Simoncini, 2010: *A Guide to Empirical Orthogonal Functions for Climate Data Analysis*. Springer Science & Business Media.

Neale, R., and Coauthors, 2010: Description of the NCAR Community Atmosphere Model (CAM 4.0). Tech.Note TN-485+STR, NCAR.

Nevison, C., and Coauthors, 2008: Contribution of ocean, fossil fuel, land biosphere, and biomass burning carbon fluxes to seasonal and interannual variability in atmospheric CO_2. *Journal of Geophysical Research*, **113 (G1)**.

Nigam, S., I. Held, and S. Lyons, 1986: Linear Simulation of the Stationary Eddies in a General Circulation Model. Part I: The No-Mountain Model. *Journal of the Atmospheric Sciences*, **43 (23)**, 2944–2961.

Oleson, K., and Coauthors, 2010: Technical Description of version 4.0 of the Community Land Model (CLM). Tech. Note TN-478, NCAR.

Olivié, D., and G. Peters, 2013: Variation in emission metrics due to variation in CO_2 and temperature impulse response functions. *Earth System Dynamics*, **4 (2)**, 267–286.

Olivié, D., G. Peters, and D. Saint-Martin, 2012: Atmosphere Response Time Scales Estimated from AOGCM Experiments. *Journal of Climate*, **25 (22)**, 7956–7972.

Pearman, G., P. Hyson, and P. Fraser, 1983: The Global Distribution of Atmospheric Carbon Dioxide: 1. Aspect of Observations and Modeling. *Journal of Geophysical Research*, **88 (C6)**, 3581–3590.

Ruzmaikin, A., H. Aumann, and T. Pagano, 2012: Patterns of CO_2 Variability from Global Satellite Data. *Journal of Climate*, **25 (18)**, 6383–6393.

Shine, K., S. Fuglestvedt, K. Hailemariam, and N. Stuber, 2005: Alternatives to the global warming potential for comparing climate impacts of emission of greenhouse gases. *Climatic Change*, **68 (3)**, 281–302.

Simmonds, I., 1985: Analysis of the "Spinup" of a General Ciruclation Model. *Journal of Geophysical Research*, **90 (D3)**, 5637–5660.

Simmons, A., and R. Strüfing, 1983: Numerical forecast of stratospheric warming events using a model with hybrid vertical coordinate. *Quart. J. Roy. Meteor. Soc.*, **109 (459)**, 81–111.

Simmons, A., J. Wallace, and G. Branstator, 1983: Barotropic Wave Propagation and Instability, and Atmospheric Teleconnection Patterns. *Journal of the Atmospheric Sciences*, **40 (6)**, 1363–1392.

Smith, J., and T. Wigley, 2000a: Global Waming Potentials: 1. Climatic implications of emission reductions. *Climatic Change*, **44 (4)**, 445–457.

Smith, J., and T. Wigley, 2000b: Global Warming Potentials: 2. Accuracy. *Climatic Change*, **44 (4)**, 459–469.

Stouffer, R., 2004: Time Scale of Climate Response. *Journal of Climate*, **17 (1)**, 209–217.

Stouffer, R., and S. Manabe, 1999: Response of a Coupled Ocean-Atmosphere Model to Increasing Atmospheric Carbon Dioxide: Sensitivity to the Rate of Increase. *Journal of Climate*, **12 (8)**, 2224–2237.

Tans, P., I. Fung, and T. Takahashi, 1990: Observational Constraints on the Global Atmospheric CO_2 Budget. *Science*, **247**, 1431–1438.

Ting, M., 1996: Steady Linear Response to Tropical Heating in Barotropic and Baroclinic Models. *Journal of the Atmospheric Sciences*, **53 (12)**, 1698–1709.

Ting, M., and P. Sardeshmukh, 1993: Factors Determining the Extratropical Response to Equatorial Diabatic Heating Anomalies. *Journal of the Atmospheric Sciences*, **50 (6)**, 907–918.

Ting, M., and L. Yu, 1998: Steady Response to Tropical Heating in Wavy Linear and Nonlinear Baroclinic Model. *Journal of the Atmospheric Sciences*, **55 (24)**, 3565–3582.

Trenberth, K., and Coauthors, 1998: Progress during TOGA in understanding and modeling global teleconnections associated with tropical sea surface temperatures. *Journal of Geophysical Research*, **103 (C7)**, 14 291–14 324.

Valdes, P., and B. Hoskins, 1989: Linear Stationary Wave Simulations of the Time-Mean Climatological Flow. *Journal of the Atmospheric Sciences*, **46 (16)**, 2509–2527.

Voss, R., and U. Mikolajewicz, 2001: Long-term climate changes due to increase CO_2 concentration in the coupled atmosphere-ocean general circulation model ECHAM3/LSG. *Climate Dynamics*, **17 (1)**, 45–60.

Wallace, J., and D. Gutzler, 1981: Teleconnections in the Geopotential Height Field during the Northern Hemisphere Winter. *Monthly Weather Review*, **109 (4)**, 784–812.

Washington, W., and C. Parkinson, 2005: *An Introduction to Three-Dimensional Climate Modeling*. 2nd ed., University Science Books.

Williamson, D., 1983: Description of the NCAR Community Climate Model (CCM0B). Tech.Note TN-210+STR, NCAR.

Williamson, D., 2002: Time-Split versus Process-Split Coupling of Parametrizations and Dynamical Core. *Monthly Weather Review*, **103 (8)**, 2024–2041.

Williamson, D., and G. Olson, 1994: Climate Simulations with a Semi-Lagrangian Version of the NCAR Community Climate Model. *Monthly Weather Review*, **122 (7)**, 1594–1610.